LOCKHEED MARTIN ENERGY RESEARCH LIBRARIES

3 4456 0441315 0

ORNL/TM-13256

ornl

OAK RIDGE NATIONAL LABORATORY

LOCKHEED MARTIN

Effect of Stress Rate on Helium Bubble Kinetics During Welding of Helium Containing Materials

C. A. Wang

OAK RIDGE NATIONAL LABORATORY
CENTRAL RESEARCH LIBRARY
CIRCULATION SECTION
4500N ROOM 175
LIBRARY LOAN COPY
DO NOT TRANSFER TO ANOTHER PERSON
If you wish someone else to see this report, send in name with report and the library will arrange a loan.
ornl-1813 (8-77)

MANAGED AND OPERATED BY
LOCKHEED MARTIN ENERGY RESEARCH CORPORATION
FOR THE UNITED STATES
DEPARTMENT OF ENERGY

ORNL-27 (3-96)

This report has been reproduced directly from the best available copy.

Available to DOE and DOE contractors from the Office of Scientific and Technical Information, P. O. Box 62, Oak Ridge, TN 37831; prices available from (423) 576-8401, FTS 626-8401.

Available to the public from the National Technical Information Service, U.S. Department of Commerce, 5285 Port Royal Road, Springfield, VA 22161.

This report was prepared as an account of work sponsored by an agency of the United States Government. Neither the United States Government nor any agency thereof, nor any of their employees, makes any warranty, express or implied, or assumes any legal liability or responsibility for the accuracy, completeness, or usefulness of any information, apparatus, product, or process disclosed, or represents that its use would not infringe privately owned rights. Reference herein to any specific commercial product, process, or service by trade name, trademark, manufacturer, or otherwise, does not necessarily constitute or imply its endorsement, recommendation, or favoring by the United States Government or any agency thereof. The views and opinions of authors expressed herein do not necessarily state or reflect those of the United States Government of any agency thereof.

ORNL/TM-13256

Metals and Ceramics Division

EFFECT OF STRESS STATE ON HELIUM BUBBLE KINETICS DURING WELDING OF HELIUM CONTAINING MATERIALS

C. A. Wang

Date Published: July 1996

Prepared by the
OAK RIDGE NATIONAL LABORATORY
Oak Ridge, Tennessee 37831
managed by
LOCKHEED MARTIN ENERGY RESEARCH CORPORATION
for the
U.S. DEPARTMENT OF ENERGY
under contract DE-AC05-96OR22464

LOCKHEED MARTIN ENERGY RESEARCH LIBRARIES

3 4456 0441315 0

ACKNOWLEDGEMENTS

The author would like to express his sincere thanks and appreciation to Prof. Bryan Chin for his constant support, guidance and perseverance throughout the duration of this study. The author would also like to thank Dr. Martin Grossbeck for his help, guidance and encouragement. The author would like to thank Dr. Tomo Sawai and Mr. Alex Fischer for help with TEM operations. Thanks are due Dr. Janet Pawel, Mr. Charlie DeVore and Mr. Pat Howard for testings of irradiated materials. Thanks are also due Dr. Jim Bentley, Dr. Steve Zinkle and Dr. H. T. Lin for helpful discussions. The author would also like to thanks Mr. L. T. Gibson, Mr. Scott Eatherly and Mr. Wade Jones with various aspects of experimental operations. Special thanks to Dr. Joe Wermer for preparation of tritiated specimens. The author would like to express the deepest gratitude to his family, especially his mother Ms. Chun-Li Chiang without whose love, support and understanding this work could not have been accomplished. This research was sponsored by the Office of Fusion Energy, U. S. Department of Energy, under contact DE-AC05-96OR22464 and grant DE-FG05-91ER54134 with the Lockheed Martin Energy Research Corp. and Auburn University.

ABSTRACT

EFFECT OF STRESS STATE ON HELIUM BUBBLE KINETICS DURING WELDING OF HELIUM-CONTAINING MATERIALS

Chin-An Wang

Catastrophic centerline interdendritic fractures in the fusion zone and intergranular cracking in the heat-affected zone have been observed in helium-bearing materials using the conventional gas tungsten arc welding process. Helium, generated from (n-α) reactions in a nuclear reactor, nucleates and grows to form bubbles which subsequently grow and coalesce rapidly along grain boundaries subjected to a tensile stress at elevated temperatures. This study investigated the threshold helium concentrations required to cause weld cracking and developed techniques to eliminate helium-induced weld cracking in irradiated materials.

Severe heat-affected zone cracking occurred in type 316 stainless steel containing 1.5, 5.2 and 9.7 appm He, introduced by tritium charging and decay. Macrocracks, visible to the naked eye, were found to occur in up to 72% of the total weld length. Fusion zone cracking was also observed in steels with He concentrations as low as 2.5 appm. No cracking was found in either the fusion zone or

heat-affected zone in the welds with 0.7 appm helium. The threshold He concentrations required to cause welding cracking in type 316 stainless steel was predicted at 0.9 appm. Fusion zone cracking was also found in PCA alloy with 11.4 appm He concentrations. No cracking was observed in HT-9 steel with up to 2.5 appm He concentrations. Severe fusion zone cracking was also observed in type 316 stainless steel, 6.9 appm He, and PCA alloy, 6.3 appm He, irradiated at 200°C in Oak Ridge Research Reactor.

A stress-modified gas tungsten arc welding technique was developed which minimizes the effects of helium-induced weld cracking. The application of a compressive stress, about 25% of the yield stress, during welding was found to effectively suppress the weld cracking observed in conventional welding process. Cracking was eliminated with a compressive stress about 75% of the yield stress. Electron microscopy showed that grain boundary helium bubble growth was retarded by the applied compressive stresses and the bubbles may not reach the critical size leading to catastrophic cracking. The results indicate that the stress-modified welding technique may be used to suppress and control helium-induced cracking during repair welding of irradiated materials.

TABLE OF CONTENTS

LIST OF TABLES ix

LIST OF FIGURES xi

I. INTRODUCTION 1

II. LITERATURE REVIEW 5

Effect of Neutron Irradiation on Materials 5
Formation of Helium Bubbles 7
Migration Mechanisms of Helium in Stainless Steel 8
Growth of Helium Bubbles 9
Stresses which Occur during Welding 15
Influence of Helium on Material Properties 18
Weldability of He-Containing Materials 27
Reduction of Weld Cracking 40

III. EXPERIMENTAL PROCEDURES 52

Materials 52
Helium-Doping Process 56
Gas Tungsten Arc Welding Process 61
Temperature Measurement during Welding 63
Mechanical Properties Characterization 66
Tensile Tests 66
Microhardness Tests 68
Microscopy 68
Optical Microscopy 68
Scanning Electron Microscopy (SEM) 69
Transmission Electron Microscopy (TEM) 69
TEM Foil Thickness Measurement 70
Quantitative Bubble Analysis 71

IV. EXPERIMENTAL RESULTS 73

Temperature Profile during Welding 73
Helium-Charging 75
Optical Microscopy 77
Weld Integrity 83
Stress Effects 86
Microhardness Tests 95

Tensile Tests 99
Scanning Electron Microscopy 104
Transmission Electron Microscopy 117
Welding of Neutron Irradiated Materials 138

V. THEORETICAL INTERPRETATION 147

VI. DISCUSSIONS 171

Theoretical Interpretation 171
Release of Helium during Welding 174
Stress And Weld Cracking 176
Stress Direction and Bubble Growth 177
Welding of Neutron Irradiated Materials 181
Welding Techniques 183

VII. CONCLUSIONS 187

REFERENCES 189

APPENDIXES 202

LIST OF TABLES

1. Tensile test data of unwelded type 316 stainless steel [19] 23

2. Tensile test data of welded type 316 stainless steel [19] 25

3. Tensile test data of HT-9 steel [19] 26

4. Helium bubble density and size after one hour aging at high temperature for type 316 stainless steel containing 256 appm He [19] 38

5. Results of tensile test of overlay weld for type 304 stainless steel [15] 44

6. Comparison of helium-induced weld cracking tendency among various alloys [19] 50

7. Chemical compositions of type 316 stainless steel (Reference Heat 8092297), HT9 (Heat 9607-R2) and PCA steels. 54

8. Heat treatment processes 55

9. Helium-doping conditions 60

10. Welding power supply settings 64

11. Gas tungsten arc welding parameters 65

12. Helium concentration in tritium-charged steel samples 76

13. Susceptibility to weld cracking of type 316 stainless steel, standard GTA welding process 87

14. Susceptibility to weld cracking of PCA Alloy, standard GTA welding process 89

15. Weld cracking in type 316 stainless steel 93

16. Weld cracking in PCA-B3 alloy 94

17. Room temperature tensile properties of stress modified welds and unwelded base material of type 316 stainless steel containing 0.7 and 1.5 appm helium 102

18. Room temperature tensile properties of stress modified welds and unwelded base material of type 316 stainless steel containing 5.2 and 9.7 appm helium 103

19. Room temperature tensile properties of stress modified welds and unwelded base material of PCA-B3 alloy 105

20. Room temperature tensile properties of stress modified welds and unwelded base material of HT-9 steel 106

21. Parameters used for the welding neutron irradiated materials 141

22. Test matrix of crack growth specimens from ORR-MFE-6J capsule 142

23. Parameters used in Regime II calculation 153

24. Temperature dependent Young's modulus and the thermal expansion coefficient of type 316 stainless steel [124] 165

25. Surface free energy of type 304 stainless steel [125] 166

LIST OF FIGURES

1. The interaction of high energy particles with the nuclei of a solid lattice can lead to (a) displaced lattice atoms (interstitials) and vacancies and to (b) transmutation products (e.g. He-nuclei created by (n,α) reactions) [24] 6

2. Three possible mechanisms of helium atom diffusion through the lattice by (a) interstitial migration, (b) vacancy mechanism, and (c) impeded interstitial migration [26] 10

3. Illustration of (a) unconstrained cavity growth, and (b) constrained cavity growth [19] 12

4. Schematic representation of changes in grain boundary cavity growth mechanisms during welding [16] 13

5. Schematic representation of changes in temperature and stress during welding [54] 16

6. TEM micrographs of helium bubbles associated with dislocations and grain boundaries [19] 19

7. Effects of He-implantation and testing temperature on the fatigue properties of type 316 stainless steel [58] 20

8. Helium-induced fracture toughness reduction in various alloys [93] 28

9. Cracking of as-welded type 316 stainless steel with 2.5 appm helium [19] 32

10. Structure of as-welded type 316 stainless steel with 105 appm helium. (a) Brittle fracture in fusion and heat-affected zones, (b) HAZ intergranular fracture, (c) Dimple structure on the HAZ fracture surfaces, (d) Fusion zone interdendritic fracture surfaces [19] 33

11. Microstructure of as-welded helium-doped V-15Cr-5Ti alloy. (a) Welding cracking in fusion and heat-affected zones, (b) SEM micrograph of HAZ intergranular fracture, (c) Dimple structure on the HAZ fracture surfaces [96] 35

12. Structure of as-welded HT-9 with 1 appm He. (a) Intergranular fracture along prior-austenite grain boundaries, (b) Grain boundary facets decorated with uniformly distributed dimples [19] 36

13. Results of room temperature tensile tests of type 316 stainless steel containing 256 appm helium after aging [19] 39

14. Percentage of reduction of area as a function of peak annealing temperature in helium charged type 304L stainless steel [97] 41

15. Schematic representation of weld overlay process [98] 42

16. Effect of doped-helium on the tensile test reduction of area in type 304 stainless steel [15] 45

17. Underbead cracking in the overlay welding process. (a) Intergranular HAZ cracking, (b) Intergranular facets reveal dimple structure at higher magnification [98] 47

18. Total weld cracking is effectively reduced in overlay welding process compared to conventional stringer bead welding process [98] 48

19. Comparison of weld cracking tendency of austenitic stainless steels containing 2 appm helium. (a) Solution annealed type 316 stainless steel, (b) 20% cold-worked type 316 stainless steel (c) Solution annealed prime candidate alloy [19] 51

20. Schematic representation of the helium doping process 58

21. Hydraulic weld plate fixture system 62

22. Schematic representation of an SS-3 tensile specimen 67

23. Temperature time history of heat-affected zone during GTA welding of type 316 stainless steel. (a) full process (b) cooling curve 74

24. Microstructure of type 316 stainless steel after gas tungsten arc welding. (a) fusion zone (b) HAZ (c) base metal 78

25. Type 316 stainless steel has stringers dispersed in the matrix. They were identified as MnS_2 by x-ray microprobe analysis 80

26. Microstructure of PCA-B3 alloy after gas tungsten arc welding. (a) fusion zone (b) HAZ (c) base metal 81

27. Microstructure of HT-9 steel after gas tungsten arc welding. (a) fusion zone (b) HAZ (c) base metal 82

28. Weld cracking of type 316 stainless steel containing 5.2 appm helium using standard GTA welding process 84

29. Microcracks in the heat-affected zone of type 316 stainless steel, 9.7 appm He. Cracking occurs perpendicular to stresses developed during cooling 85

30. Weld cracking increases as the He concentration increases 88

31. Hydraulic jack pressure calibration 91

32. Results of the hydraulic jack pressure calibration 92

33. Microhardness across welds of type 316 stainless 96

34. Microhardness across welds of PCA-B3 alloy 97

35. Microhardness across welds of HT-9 steel 98

36. Results of room temperature tensile tests of type 316 stainless steel in as-charged condition 100

37. Tensile properties of He-doped type 316 stainless steel following welding 101

structure in type 316 stainless steel containing 9.7 appm He in a standard GTA weld. Welding direction (wd) is indicated by an arrow 122

49. Extensive dislocation network was observed in the matrix of standard weld HAZ and helium bubbles were found to be concentrated at grain boundaries, 9.7 appm He concentration 123

50. Very few or no helium bubbles were observed in some areas of the standard weld HAZ, 9.7 appm He concentration. One of the bubbles is indicated by the arrowhead 124

51. TEM micrograph of base metal of a standard GTA weld of type 316 stainless steel containing 9.7 appm He. No helium bubbles were observed. Welding direction (wd) is indicated by an arrow 125

52. TEM micrograph of helium bubbles as large as 1 μm at the fusion zone of a standard weld, 9.7 appm He concentration 126

53. Effect of applied compressive stress during welding on the growth of helium bubbles of a type 316 stainless steel weld containing 9.7 appm He 128

54. Effect of applied compressive stress during welding on the helium bubble density of type 316 stainless steel weld containing 9.7 appm He 130

55. TEM micrograph of a grain boundary triple junction at the HAZ of type 316 stainless steel, 9.7 appm He, with 55 MPa applied compressive stress during welding. Welding direction (wd) is indicated by an arrow 131

56. No bubbles were observed in grain boundaries of a junction at the HAZ of type 316 stainless steel, 9.7 appm He, with 110 MPa applied compressive stress during welding 132

57. HAZ subgrain structure with extensive bubble nucleation and growth in type 316 stainless steel, 9.7 appm He, with 55 MPa applied compressive stress during welding 133

38. Heat-affected zone cracking of type 316 stainless steel containing 1.5 appm helium 107

39. Cavity size distribution and cavity volume average diameter ($VAD=(\Sigma N_i D_i^3/\Sigma N_i)^{1/3}$) of HAZ fracture surfaces in type 316 stainless steel 109

40. Comparison of heat-affected zone in standard and stress-modified weld of type 316 stainless steel containing 5.2 appm helium: (a,b) continuous through thickness fusion zone and heat-affected zone cracking in a standard weld; (c,d) no visible cracking in stress-modified weld 110

41. Interdendritic fusion zone cracking was observed in type 316 stainless steel containing as low as 5.2 appm He, b, c and d show increasing magnification of the fusion zone cracking 111

42. Intergranular HAZ cracking was fully decorated with cavities caused by grain boundary helium bubble growth in type 316 stainless steel containing 5.2 appm He; b, c and d show increasing magnification of the HAZ fracture surfaces 112

43. HAZ fracture surface cavity size distribution for type 316 stainless steel containing 5.2 and 9.7 appm He 114

44. SEM photographs of jet-polished TEM discs from (a) standard GTA weld; (b) stress-modified GTA weld. Arrows indicate the welding direction (wd). (C) and (d) are magnified features of circle in (a) and (b) respectively 115

45. Heat-affected zone cracking was found around the weld pool of a steady state weld of type 316 stainless steel containing 1.5 appm He 116

46. Fusion porosity morphology in type 316 stainless steel containing 9.7 appm He after GTA welding 118

47. Results of TEM calibrations: (a) magnification and (b) image rotation 119

48. TEM micrograph of the HAZ helium bubble

58. Weld cracking in terms of crack length per length of a weld as a function of applied stress. Weld cracking is effectively suppressed as applied compressive stress increases during welding 134

59. Relationship between grain boundary bubble density and grain boundary direction with respect to the weld in the modified compressive welds 136

60. Relationship between adjacent grain boundary resolved stress and grain boundary helium bubble number 137

61. Crack growth specimen 140

62. Photographs of welds of irradiated type 316 stainless steel using (a) standard welding process - fusion zone cracking indicated by an arrow (b) stress-modified welding process, 55 MPa - no cracking 144

63. Photographs of welds of irradiated PCA alloy (a) standard welding process - fusion zone cracking indicated by an arrow (b) stress-modified welding process, 165 MPa - no cracking 145

64. Photographs of welds of irradiated HT-9 steel using (a) standard welding process (b) stress-modified welding process, 165 MPa. No cracking was observed 146

65. Vacancy diffusion into a bubble along a grain boundary is everywhere radial 149

66. Predicted grain boundary helium bubble growth in Regime II during welding 154

67. Predicted results of bubble coalescence after GTA welding of helium containing type 316 stainless steel 157

68. Surface and grain boundary diffusivities of type 316 stainless steel as a function of temperature 160

69. Surface free energy as a function of temperature 167

70. Predicted grain boundary bubble growth in final stage, Regime III, during welding 168

71. Comparison of grain boundary bubble growth in Regime III 170

72. Bubble diameter as a function of peak temperature for three typical values of vacancy formation energy 172

73. Relationship between results of aging experiment [19] and theoretical model of grain boundary bubble growth 173

74. Predicted results of grain boundary bubble growth at different peak temperatures during welding 175

75. Threshold helium concentration required to cause severe cracking in type 316 stainless steel using a conventional GTA welding process was predicted to be 0.9 appm by the experimental data 178

76. Distribution of bubble size in the matrix (a) and at grain boundaries (b) as determined by transmission electron microscopy 180

77. Relationship between the resolved stress ratio and actual bubble number ratio on the adjacent grain boundaries. Shaded area indicates preferred grain boundary bubble growth 182

I. INTRODUCTION

The exposure of metallic materials, such as structural components of the first wall and blanket of a fusion reactor, to neutron irradiation will induce changes in both the material composition and microstructure. Along with these changes can come a corresponding deterioration in mechanical properties resulting in premature failure. It is, therefore, essential to expect that the repair and replacement of the degraded components will be necessary. Such repairs may require the joining of irradiated materials through the use of fusion welding processes.

The present ITER (International Thermonuclear Experimental Reactor) conceptual design is anticipated to have about 5 km of longitudinal welds and ten thousand pipe butt welds in the blanket structure. A recent study by Buende et al. [1] predict that a failure is most likely to occur in a weld. Although they do not state this as a conclusion because of uncertainties in the input data and in the analysis, their study indicates that the ITER will have a 97% down-time. The study is based on data from other large structures, particularly nuclear reactors. The data used also appear to be consistent with the operating

experience of the Fast Flux Test Facility (FFTF). This reactor has a fuel pin area comparable with the area of the ITER first wall and has experienced one unanticipated fuel pin failure after two years of operation. A fusion reactor has many more welds and critical blanket structures of far higher complexity than found in fission reactors.

The study from Buende et al. indicates the necessity for an effort to design a more reliable structure. The authors recommend three approaches: improvement of manufacturing quality of the welds, load reduction and separation by removing welds from areas with multiple loads, and reduction of the number of critical welds. The above recommendations are important to building a reliable fusion device. However, another essential improvement that follows from such studies is that there must be removable blanket modules, spare modules, and most important, a method of repair for the inevitable failures. It is the latter issue that is addressed in the present study.

The repair of irradiated structures using fusion welding will be difficult due to the entrapped helium. Helium is primarily generated by the reactions of thermal neutrons and alloying constituents in the metal, principally with nickel and boron:

$$^{58}Ni + n \longrightarrow {}^{59}Ni + \gamma \qquad (1)$$

$$^{59}Ni + n \longrightarrow {}^{56}Fe + {}^{4}He \qquad (2)$$

$$^{10}B + n \longrightarrow {}^{7}Li + {}^{4}He \qquad (3)$$

Due to its extremely low solubility in metals, helium will diffuse and agglomerate to form helium bubbles after being trapped at point defects, dislocations and grain boundaries. It has been known for several decades that the degradation of irradiated materials at elevated temperature is partially exacerbated by the presence of helium. At high temperature, helium bubbles have been shown to grow rapidly along grain boundaries under the influence of both temperature and stress [2-5]. This situation is found typically in autogenous welding upon cooling. Internal tensile stresses are generated due to the volume contraction upon solidification and subsequent thermal contraction in the solid state.

Welding of neutron-irradiated type 304 stainless steels has been reported with varying degree of heat-affected zone (HAZ) cracking [6-15]. Catastrophic heat-affected zone intergranular cracking following gas tungsten arc (GTA) welding was also observed by Lin et al. in type 316 stainless steel with doped helium levels greater than 2.5 appm [16-20]. Centerline interdendritic fractures in the fusion zone have also been observed in GTA welds of alloys containing greater than 100 appm helium. The HAZ fracture surfaces were fully decorated by cavities about 1 μm in diameter. These severe failures are attributed to the growth of helium bubbles at the HAZ grain boundaries and weld dendrite interface.

The objectives of this study were to determine the threshold helium concentrations required to cause HAZ cracking and to investigate techniques that might be used to eliminate the heat-affected zone cracking in welding of helium-containing materials. The welding techniques need to be identified to enable repair and maintenance of the first wall of a fusion reactor through GTA welding. This work studied the effects of the stress field modification during cooling by the application of a controlled compressive stress perpendicular to the weld direction prior to welding. The applied stresses readily change the stress state of grain boundaries and alter the growth kinetics of grain boundary helium bubbles. This study primarily focused on materials of type 316 stainless steel doped with helium by tritium charging and decay. Some work was also included for tritiated Sandvik HT-9 steel and prime candidate alloy (PCA) and neutron irradiated steels.

II. LITERATURE REVIEW

Effect of Neutron Irradiation on Materials

It is known that high energy neutrons impinging on materials can degrade structural components. The deterioration of materials is a consequence of the interactions between the fast neutron and the lattice atoms as shown in Figure 1 [24]. The threshold energy for atomic displacement of atoms in metals is generally between 10 and 30 eV [25]. When the high energy neutrons, 14 MeV, bombard the metal, they transfer the energy into lattice atoms causing atomic displacements and formation of vacancies. The process continues until the recoil energy is less than the threshold energy for atomic displacement. Another significant effect, resulting from the neutron irradiation, is the production of transmuted atoms, such as helium, in the metal. These foreign atoms modify the microstructure and therefore change the mechanical properties. Another source of helium production in fusion facilities is by tritium decay. Due to the inert nature, helium atoms can agglomerate, nucleate and grow into bubbles within metals and lead to premature failure.

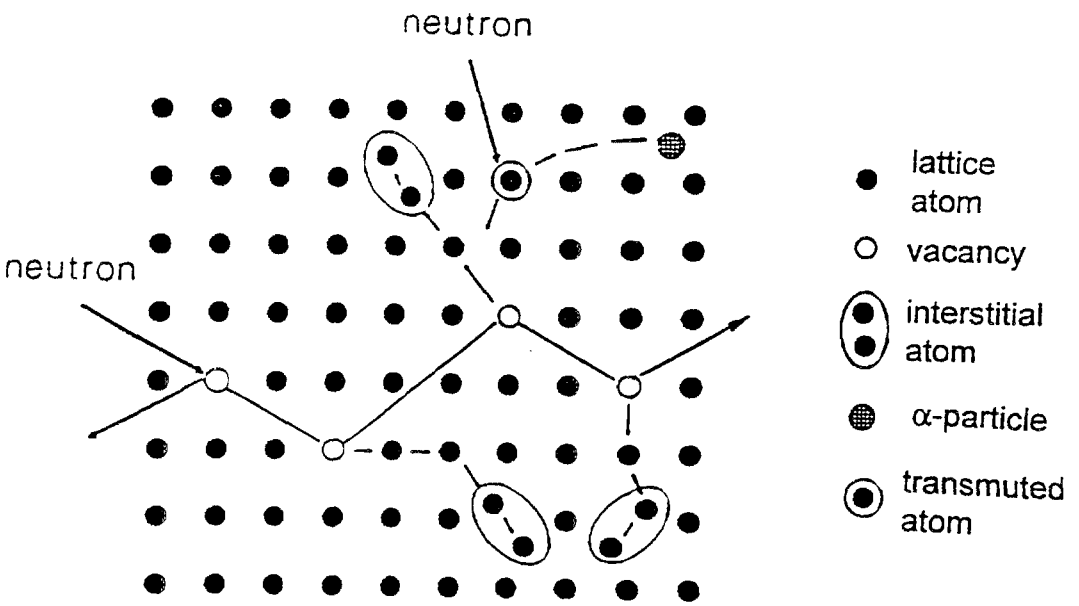

Figure 1. The interaction of high energy particles with the nuclei of a solid lattice can lead to (a) displaced lattice atoms (interstitials) and vacancies and to (b) transmutation products (e.g. He-nuclei created by (n,α) reactions) [24].

Formation of Helium Bubbles

The formation energy for helium interstitial solution in metals is found to be much higher than the corresponding energy for vacancy substitutional solution [24,26]. However, even for the more energetically favorable substitutional solution, the equilibrium concentration is found to be extremely small [26,27]. This low solubility promotes the precipitation of He atoms into clusters or bubbles which deteriorates the mechanical properties of the material.

Investigations have shown that the formation of helium bubbles in metals occurs primarily by three mechanisms: self-interstitial emission [28-31], loop punching [32,33] and thermal vacancy absorption [24]. In the self-interstitial emission mechanism, studies show that the interstitial helium atom clusters produce considerable elastic strain and are capable of ejecting lattice atoms [28-31]. Helium bubbles can nucleate simply by the repetitive emission of self-interstitial atoms even without the thermal or radiation induced vacancies. Deep sinks such as impurities and dislocations have been shown to effectively enhance the nucleation of helium bubbles in metals [34,35].

In the loop-punching mechanism, when the pressure of a helium bubble exceeds a threshold value, vacancies can be created by punching out a platelet of lattice atoms along a

glide plane. This mechanism is called loop punching proposed by Greenwood et al. [32]. In this process, the over-pressurized bubbles can produce their own vacancies and interstitial dislocation loops by pressure relaxation. The threshold pressure required for loop punching is given by

$$p > 2\gamma_s/r + \mu b \log(r/b)/2\pi r \qquad (4)$$

where p is the helium bubble pressure, r is the bubble radius, γ_s is the surface energy of bubble, μ is the shear modulus of the solid and b is the length of the Burger's vector of the resulting dislocation loop. Both self-interstitial emission and loop punching are favored at lower temperature.

At elevated temperature, bubble formation by vacancy absorption becomes significant due to high equilibrium vacancy concentrations. Because of the high binding energy with vacancies, helium atoms tend to agglomerate at vacancy sites. Helium bubble nucleation is enhanced and preferentially located at the grain boundaries, dislocations and precipitate interfaces [24].

Migration Mechanisms of Helium in Stainless Steel

Results from experiments and computer simulations [26] suggest three migration mechanisms for the diffusion of helium in metals:

(1) The migration of helium atoms via jumps between interstitial positions as shown in Figure 2a. However, Ullmaier [24] pointed out that free interstitial migration will only be observed in lattices that are free of vacancies and other traps for helium. Since extensive vacancies and dislocations are formed during neutron irradiation, only the following two mechanisms are assumed to be relevant for materials in a fusion environment.

(2) Helium atoms can migrate by the vacancy mechanism which occurs in most substitutional alloys as shown in Figure 2b. For $T < 0.6\ T_m$, it is found that the stationary concentration of irradiation-induced vacancies in a fusion environment is higher than the thermal vacancy concentration. This will enhance the migration by the vacancy mechanism and make the diffusion coefficient less temperature-dependent than in the purely thermal case.

(3) If the He-vacancy binding is not strong and the vacancy formation energy is high, the substitutional He atoms are able to dissociate from vacancies and then migrate interstitially until they are trapped again as shown in Figure 2c. This process is referred to as impeded interstitial migration.

Growth of Helium Bubbles

After the nucleation, helium bubbles can grow by migration and coalescence [36-41] and Ostwald ripening

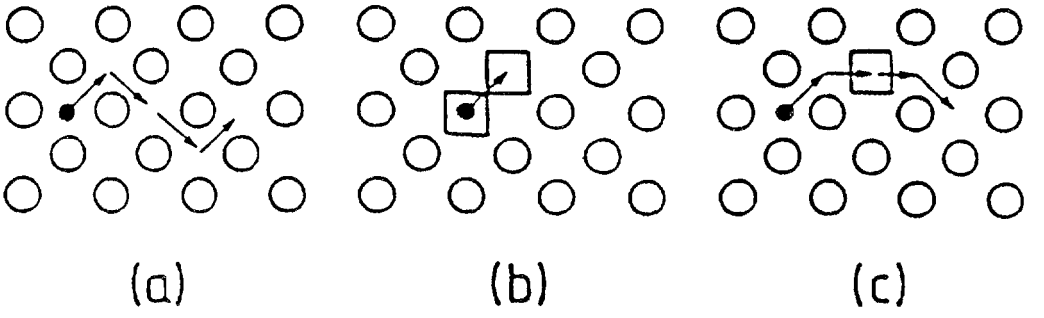

Figure 2. Three possible mechanisms of helium atom diffusion through the lattice by (a) interstitial migration, (b) vacancy mechanism, and (c) impeded interstitial migration [26].

[42-44]. The coalescence can occur by random migration of the helium bubbles or by biased migration, such as in the presence of a thermal or stress [45-53] gradient. Ostwald ripening occurs when a system reduces overall surface free energy and by the growth of larger bubbles at the expense of smaller ones.

Basically, the cavity (helium bubble) growth on grain boundaries can be divided into two types: unconstrained and constrained [19]. In the case of unconstrained growth, cavities are present on all the grain boundaries and are free to grow as shown in Figure 3a. In the constrained growth case, cavities are present preferentially on grain boundaries normal to the applied constraints as shown in Figure 3b.

During the welding process, the kinetics of grain boundary helium bubble growth in the HAZ can be divided into three regimes as shown in Figure 4 [16,19]. Regime I is the heatup period before the temperature reaches the melting point. During this regime, compressive stress is produced due to the thermal expansion of the plate. Regime II represents the period of peak temperature when the molten pool is present. This regime is stress-free. Regime III begins when the weld solidification takes place and tensile stresses are generated due to solidification shrinkage.

During the first regime, grain boundary helium bubbles can grow by the absorption of thermal vacancies. However,

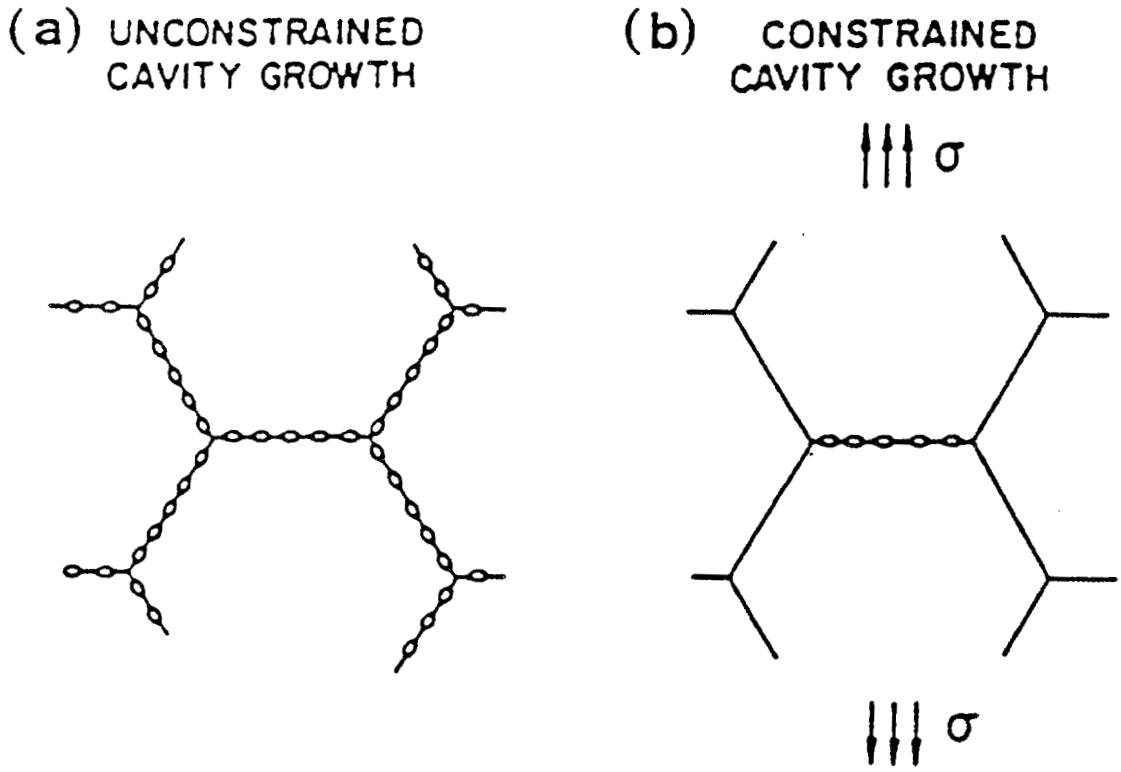

Figure 3. Illustration of (a) unconstrained cavity growth, and (b) constrained cavity growth [19].

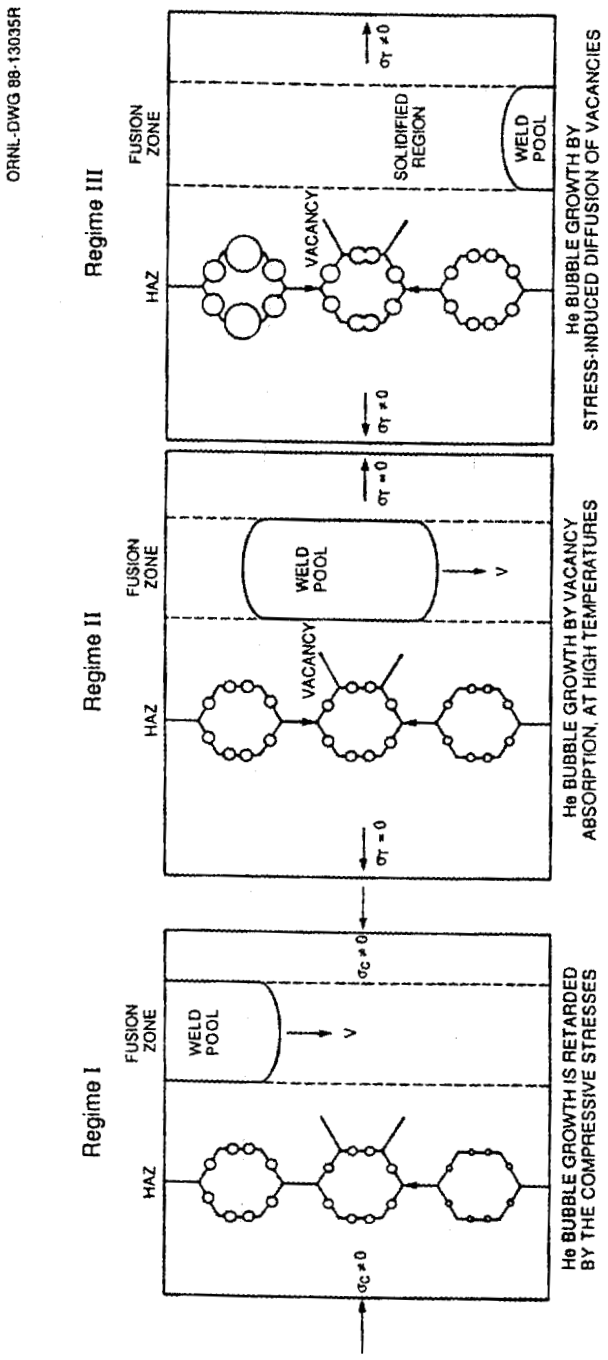

Figure 4. Schematic representation of changes in grain boundary cavity growth mechanisms during welding [16].

compressive stresses generated in this regime will tend to retard the helium bubble growth at grain boundaries normal to the compressive stresses. Therefore, the growth of grain boundary helium bubbles during welding occurs primarily in the regimes II and III.

During regime II, grain boundary bubbles grow by the mechanism of thermal vacancy absorption. As stated previously, this process is favored at temperatures close to the melting point where the equilibrium vacancy concentration is high. Helium bubble growth in regime II predicted by Lin et al. [16,19] is given by

$$R_{ii}^3 - R_i^3 = 3\delta_{gb}\Omega D_{gb}C_v\Delta t/2 \qquad (5)$$

where R_{ii} is the bubble radius after regime II, R_i is the bubble radius at the end of regime I, δ_{gb} is the grain boundary thickness, Ω is the atomic volume, D_{gb} is the grain boundary vacancy diffusivity, C_v is the equilibrium vacancy concentration, and Δt is the elapse time in regime II.

In regime III, the stress generated during welding changes to tensile due to the molten metal shrinkage during solidification and thermal contraction during cooling. The magnitude of internal tensile stresses will be enhanced if lateral external constraint is applied during welding. In this stage, the helium bubbles grow primarily by stress enhanced cavity growth. Atoms are transported from the

cavity surface to the adjoining grain boundary. Stress-assisted grain boundary cavity growth can be described by the following equation [46] based on Hull-Rimmer's model:

$$dR/dt = 2\pi\delta_{gb}D_{gb}\Omega\sigma_t/akTR \qquad (6)$$

where κ is Boltzmann's constant, a is the average bubble spacing, R is the bubble radius, T is the temperature, Ω is the atomic volume, δ_{gb} is the grain boundary thickness, σ_t is the thermal stress, and D_{gb} is the grain boundary vacancy diffusivity.

Stresses which Occur during Welding

In fusion welding, material is locally heated by the heat source to above its melting temperature, then solidifies and cools down. When the welding process is completed, residual strains resulting from the process remain in regions near the weld and therefore generate residual stresses. Dimensional changes associated with solidification of the weld metal, thermal contraction during cooling, metallurgical transformations and plastic deformation all contribute to the generation of residual stresses and distortion of a weld.

Figure 5 is a schematic which describes the changes of temperature and typical resulting stresses that occur during welding [50]. The area, cross-hatched region M-M' in Figure

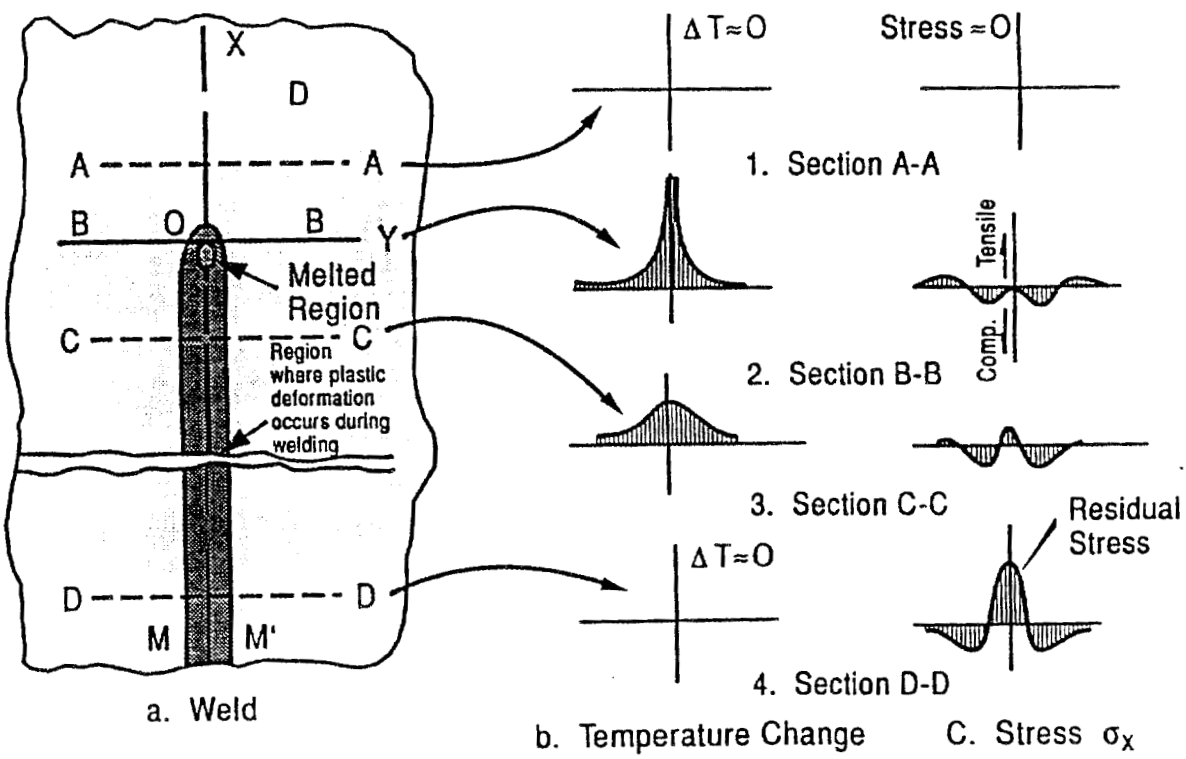

Figure 5. Schematic representation of changes in temperature and stress during welding [54].

5a, near the heat source is subjected to high temperature and undergoes plastic deformation during fusion welding. Beyond this plastic deformation area, the material remains elastic during the entire process. The heat source moving along the x-axis is indicated by the origin O as shown in Figure 5a. Temperature changes at cross section A-A, far ahead of the heat source, are relatively small and therefore introduce little or no thermal stress.

Along section B-B, which crosses the molten pool, the material is locally heated above the melting temperature and experiences a rapid change in the temperature distribution across the weld as shown in Figure 5b-2. Since the molten metal does not bear any stress, and the nearby metal expansion is restricted by the cooler metal away from the weld pool, the thermal stress changes from zero stress at the weld pool to a compressive state at the high temperature area and to a tensile state at metal away from the pool as shown in Figure 5c-2.

In the section C-C, as the heat source passes through, the molten metal solidifies and cools down subsequently. Weld metal contraction generates tensile stresses in the nearby regions as shown in Figure 5b-3. The thermal stresses now go from tensile at regions close to the weld to compressive and then diminishing tensile at regions far from the weld centerline (Figure 5c-3). At the D-D section, far behind the heat source, the metal cools down and temperature

changes again near zero. However, the stresses due to the thermal cycle are high in tension around the weld and compressive away from the weld as shown in Figure 5c-4. This is a typical stress distribution across the weld after fusion welding.

Influence of Helium on Material Properties

It has been known that mechanical properties, such as tensile, fatigue and creep, will be adversely affected by the presence of helium especially at elevated temperature [55-78]. The degradation of material properties may cause premature failure during service. The failure is normally intergranular and exhibits dimple structure on the fracture surfaces as a result of helium bubble growth at grain boundaries. TEM observations have shown that precipitate interfaces, dislocations and grain boundaries are favorable sites for the formation of large He bubbles. Figure 6 shows TEM micrographs of HAZ helium bubbles associated with dislocations and grain boundaries in type 316 stainless steel containing 256 appm He.

Fatigue properties of solution annealed type 316 stainless steel were only slightly degraded at temperatures below 500°C after He-implantation up to about 1000 appm. However, reductions in fatigue life were observed with He-implantation at higher temperature [24,57,58]. Figure 7 shows the effects of He-implantation and testing temperature

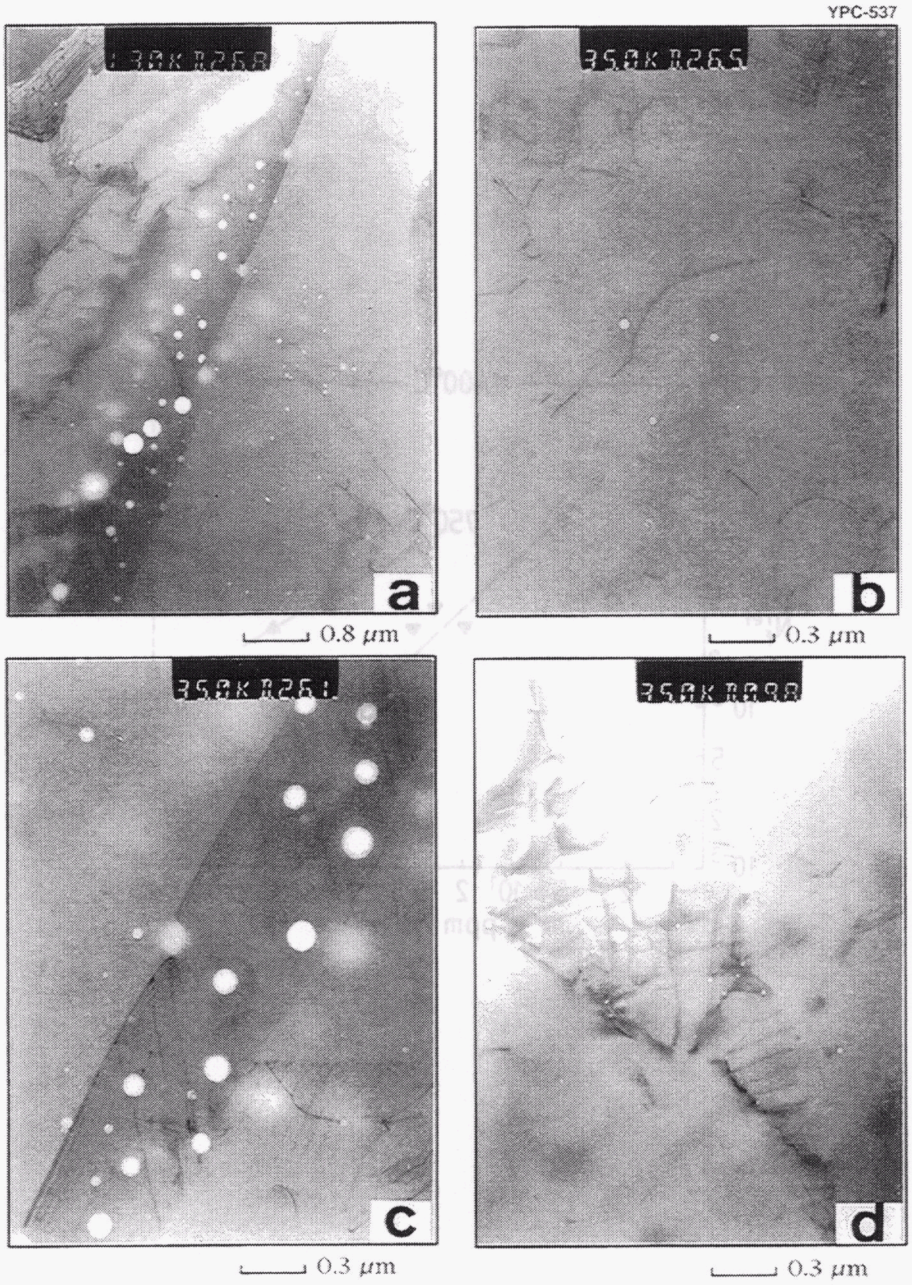

Figure 6. TEM micrographs of helium bubbles associated with dislocations and grain boundaries [19].

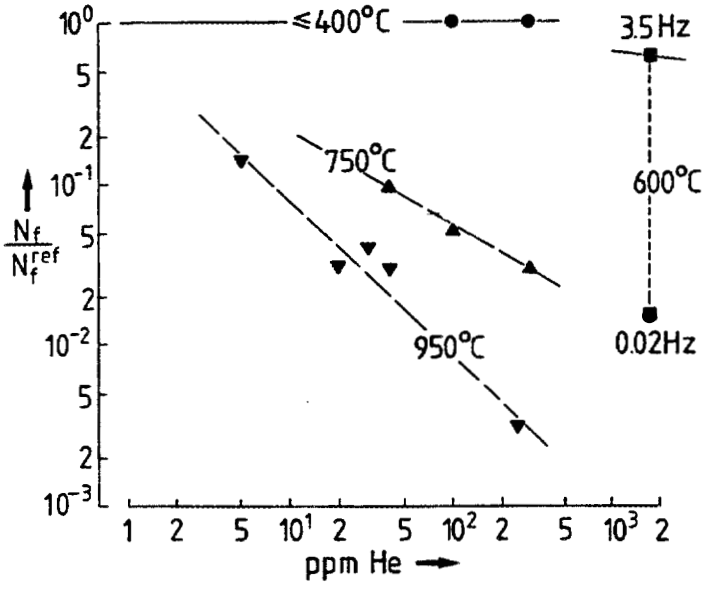

Figure 7. Effects of He-implantation and testing temperature on the fatigue properties of type 316 stainless steel [58].

on the fatigue properties of type 316 stainless steel. SEM observations showed grain boundaries were heavily perforated by helium bubbles after fatigue tests. Helium bubbles accompanied with radiation-induced voids can also cause materials to expand and distort due to swelling. The dimensional change due to the formation and growth of voids and helium bubbles has became a critical issue for materials to be used in irradiation environments [66,69,71,72].

Among the various effects of helium-induced degradation on the material properties, embrittlement is considered to be most critical [74-79]. For most materials, He-embrittlement begins at temperatures about 45% of the absolute melting temperature and intensifies with increasing temperature. In neutron irradiated austenitic stainless steels, helium embrittlement starts at around 500°C and is fully present at 550°C [79]. Kramer el al. [74] observed a loss in tensile ductility at temperatures above 540 and 650°C respectively for materials subjected to a precipitation heat treatment from the solution annealed and cold-rolled type 316 stainless steels containing 40 appm helium concentration. Significant loss of high-temperature ductility of type 304 stainless steel was also observed even at helium concentrations as low as 0.1 appm [75].

Helium embrittlement in alloys is mostly due to the nucleation and growth of helium bubbles at grain boundaries. Failure is normally characterized by an intergranular

fracture mode. Tensile test results of the neutron irradiated type 316 stainless steels showed a significant decrease in total elongation with increasing He content [59,63,80]. The embrittlement resistance can be improved by the introduction of fine stable carbide precipitates in the matrix or at the grain boundaries [80-92]. Titanium-modified type 316 stainless steel showed much less sensitivity to helium embrittlement than the unmodified materials by trapping helium bubbles on the fine precipitates. Ductile fracture occurred in titanium-modified type 316 stainless steel at temperatures below 450°C, while intergranular failure was observed above 575°C due to excessive bubble growth at grain boundaries. Embrittlement resistance can also be improved through the introduction of dislocation network by cold-work [80,87,91,92]. Precipitates and dislocations effectively trap helium bubbles and thus suppress the helium-induced embrittlement as well as swelling.

Degradation of mechanical properties was also observed in steels into which helium was introduced by tritium charging and decay [8,11,19]. Results of tensile tests of as-doped and welded type 316 stainless steels, containing from 0.18 to 256 appm He concentration, are shown in Table 1 and 2. Type 316 stainless steel did not show any sign of helium-induced strengthening with up to 256 appm He in the as-doped condition. A significant increase in the 0.2%

Table 1

Tensile test data of unwelded type 316 stainless steel [19]

Helium (appm)	Temperature (°C)	UTS (MPa)	0.2% YS (MPa)	Elongation (%)
Control	20	584.5	231.5	44.1
	20	580.1	223.5	45.2
	500	466.4	123.2	26.0
	500	487.5	124.8	25.2
	600	458.3	103.7	26.8
	600	447.0	104.6	27.2
	700	357.0	98.5	23.7
	700	340.3	99.1	21.0
0.18	20	588.2	231.4	41.9
	500	480.9	127.6	29.0
	600	454.1	111.1	27.9
	700	322.1	96.4	17.6
2.5	20	595.0	232.3	41.8
	500	480.0	121.1	27.2
	600	450.3	140.7	25.7
	700	335.1	103.5	16.9
27	20	549.7	190.1	37.8
	500	481.2	141.0	25.0
	600	458.3	117.4	25.1
	700	372.7	123.0	15.9
105	20	583.0	244.5	39.8
	500	494.0	149.0	27.1
	600	456.1	121.0	26.1
	700	328.4	126.4	11.3
256	20	601.2	250.4	44.1
	500	476.0	155.0	27.6
	600	462.9	144.7	25.6
	700	340.2	144.1	10.1

offset yield strength (YS) was found in steels with up to 105 appm helium after welding compared to the as-doped materials. However, the welds with 256 appm He showed the lowest yield strength as shown in Table 2. The ultimate tensile strength (UTS) was found insensitive to the presence of helium up to 256 appm at room temperature in the as-doped condition. Nevertheless, the UTS decreased after gas tungsten arc welding which Lin attributed to grain boundary helium bubble growth. Both yield strength and ultimate tensile strength decreased with increasing temperature in both as-doped and welded conditions. The total elongation decreased to less than 2% for type 316 stainless steel with greater than 2.5 appm doped helium after welding as shown in Table 2.

Similar deteriorations in material properties were also observed in ferritic steels [19]. Tensile test results of HT-9 ferritic steel doped with 0.3 and 1 appm helium are shown in Table 3. All the specimens failed in the base metal region. Yield strength and ultimate tensile strength of the as-doped and welded materials were insensitive to the presence of helium at these levels. Both strengths decreased with increasing temperature in all conditions. Total elongation was also found insensitive to helium up to 1 appm concentration. Contrary to that in type 316 stainless steel, the total elongation in HT-9 steel increased with increasing temperature. However, the welded

Table 2

Tensile test data of welded type 316 stainless steel [19]

Helium (appm)	Temperature (°C)	UTS (MPa)	0.2% YS (MPa)	Elongation (%)
Control[a]	20	560.2	351.2	17.8
	20	569.1	347.8	18.5
	500	387.5	244.2	7.2
	500	408.9	232.5	10.3
	600	369.7	222.3	6.0
	600	357.3	211.0	8.1
	700	325.0	197.5	7.7
	700	291.0	175.0	9.1
0.18[a]	20	518.5	358.1	10.4
	500	370.1	241.8	8.1
	600	361.0	224.0	8.6
	700	262.0	198.0	3.2
2.5[b]	20	428.3	356.9	2.9
27[b]	20	386.0	386.0	0.2
	500	296.4	266.8	0.6
	600	262.8	227.6	1.2
	700	200.0	191.0	0.3
105[b]	20[a]	404.0	373.0	1.5
	500	261.9	253.9	1.4
	600	253.1	244.1	0.6
	700	199.6	191.5	1.2
256[b]	20	247.6	247.6	1.1
	500	153.8	153.8	0.7
	600[a]	186.5	186.5	1.7
	700[a]	137.9	137.9	1.5

[a]Specimens failed in the fusion zone.
[b]Specimens failed in the fusion boundary.

Table 3

Tensile test data of HT-9 steel [19]

Helium (appm)	Temperature (°C)	UTS (MPa)	0.2% YS (MPa)	Elongation (%)
		Unwelded		
Control	20	1001.2	835.0	4.7
	20	1013.8	866.9	5.4
	500	869.5	777.0	3.0
	500	845.3	760.8	3.2
	600	654.0	616.0	7.4
	600	670.3	622.4	7.0
	700	425.5	414.2	10.5
	700	447.8	422.8	12.2
0.3	20	1034.5	903.3	6.1
	500	760.8	695.1	4.5
	600	653.4	604.0	5.5
	700	409.0	399.7	9.1
1.0	20	1038.0	893.8	5.1
	500	855.6	744.1	5.0
	600	702.4	681.3	6.6
	700	426.2	416.7	10.6
		Welded		
Control[a]	20	983.0	895.4	5.5
	20[b]	965.3	890.1	0.7
	500	815.6	765.8	4.2
	500	739.4	708.6	1.8
	600	756.4	701.6	3.4
	600	713.0	676.0	3.8
	700	418.2	408.2	7.2
	700	475.7	464.5	6.2
0.3[a]	20[b]	961.0	827.0	0.3
	500	795.7	736.4	1.6
	600	688.6	633.4	3.9
	700	372.6	356.8	8.7
1.0[a]	20	992.6	882.3	3.1
	500	812.1	764.4	2.6
	600	696.2	675.2	5.3
	700	410.4	400.8	8.0

[a]Specimens failed in the base metal.
[b]Speceimns failed in the HAZ.

specimens exhibited lower total elongation than as-doped materials due to limited base metal available for the plastic deformation at the gage section.

Fracture resistance is also affected by helium in alloys. Results of room temperature J-integral tests from Caskey's study on several high-energy-rate-forged (HERF) alloys are shown in Figure 8 [93]. Helium was introduced into these alloys by tritium charging and decay. Fracture toughness decreased rapidly with increasing helium content and reached a lower bound at 300-400 appm helium concentration. Among all the tested alloys, HERF type 316 stainless steel showed the best resistance to the helium-induced degradation. Caskey also showed that the presence of tritium in alloys could further degrade the mechanical properties due to complex interaction between tritium and helium atoms.

Weldability of He-Containing Materials

Investigations on the welding of irradiated materials have been reported at several occasions [6-15,94,95]. Hall et al. [7] welded thin wall type 304 stainless steel tubing which was irradiated in Experimental Breeder Reactor-II (EBR-II) at temperatures between 454°C and 487°C to fast fluences ranging from 1.38×10^{26} to 7.51×10^{26} n/m^2 (E > 0.1 MeV). The welds were made using only a small constraint to hold the parts together while welding in the hot cell.

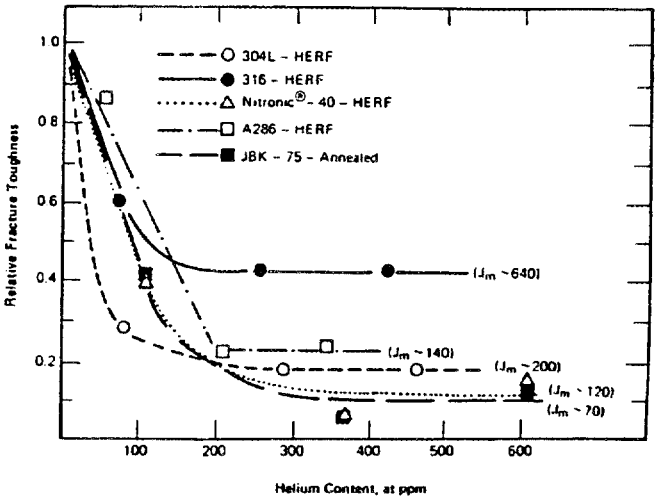

Figure 8. Helium-induced fracture toughness reduction in various alloys [93].

Intergranular cracking was observed in the HAZs of a small fraction of these specimens. The He concentration of these materials was not measured but was estimated to be between 3 to 15 appm.

Atkin [74] performed gas tungsten arc welding of 20% cold-worked type 316 stainless steel that had been irradiated in EBR-II at 400°C to a peak fluence of 1.26 x 10^{27} n/m^2 (E > 0.1 MeV). The welds were made on materials taken from reactor coolant ducts and were welded in an unconstrained condition. Based upon known irradiation conditions and measurements on materials seeing similar irradiation conditions, the helium content of the material was estimated to be between 4 to 25 appm. After welding the specimens were bend tested. Visual examination indicated the welds were sound and free from cracks. However no detailed examination or further analyses were conducted.

Hamada et al. [95] have also reported welding of 10% cold-worked type 316 stainless steel that was taken from wrapper tubes irradiated in JOYO at 395-410°C to a maximum helium content of 9 appm. GTA welds with filler metal additions were made on strips similar in configuration to the specimens prepared by Atkin [74]. The section which was being welded was allowed to float freely during welding. Welded specimens appeared to be sound. Tensile specimens taken from the weld region failed in the heat affected zone and showed a loss in ductility. Intergranular cracking was

observed in the heat-affected zone, which was attributed to the helium bubble growth during welding.

Recently efforts were initiated to repair stress-corrosion cracks in a neutron irradiated type 304 stainless steel reactor vessel at the Savannah River Site [8-15]. Patches were gas tungsten arc welded over the stress-corrosion cracks in a vessel which was measured to contain 3 appm of helium. Previous repairs of a similar vessel earlier in life had been successfully performed [6], the major difference being the increase in helium content due to further irradiation exposure. Examinations after welding revealed extensive cracking in the HAZ of the patch welds. Analyses indicated that the cracking was associated with helium bubble growth at the grain boundaries in the heat affected zone. Similar results were observed by Kanne et al. in welds of a sample from the R-reactor tank wall [12]. Helium level in this material is 30 appm following 12 years of reactor operation. Heat-affected zone cracking was intergranular and had a tendency to run perpendicular to the wall surfaces [11,12].

In order to avoid the difficulties associated with hot cell operation and reduce radiological hazards, welding was carried out on helium-doped materials by Lin et al. [16-20]. In the experiment, materials were charged with tritium at elevated temperatures and high pressures. The tritium was then allowed to decay to helium and then the excess tritium

was pumped off. In their study, type 316 stainless steel and HT-9 ferritic steel with various helium concentrations were produced and tested using the gas tungsten arc welding process. Both steels are being considered as candidate materials for near term fusion reactor structural applications. Results from their study showed that catastrophic intergranular heat-affected zone cracking occurred in type 316 stainless steel with as low as 2.5 appm He concentration. Video-taping revealed that cracking occurred at 1 to 2.2 seconds after passage of heat source during welding. Figure 9 shows the HAZ cracking on type 316 stainless steel with 2.5 appm doped helium. The HAZ fracture surfaces are fully decorated with uniformly distributed cavities about 1 μm in diameter. This cracking is attributed to the growth of helium bubbles at grain boundaries. As the helium concentration exceeded 105 appm, brittle fusion zone interdendritic cracking was also observed due to helium bubble precipitation at the dendrite interfaces as shown in Figure 10.

Severe fusion and heated-affected zone cracking were also reported by Lin and Braski in the vanadium alloy, V-15Cr-5Ti, with 25.6 appm He introduced by tritium charging and decay [96]. SEM observation revealed that large pores decorated the fusion zone fracture surfaces indicating helium bubble coalescence and growth during welding. The fracture of the vanadium alloy indicates that it is more

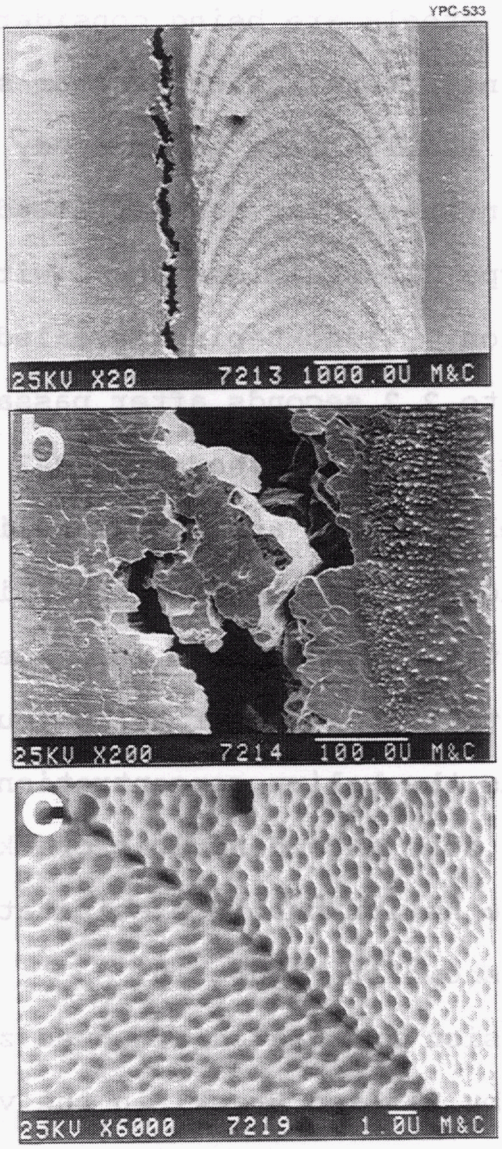

Figure 9. Cracking of as-welded type 316 stainless steel with 2.5 appm helium [19].

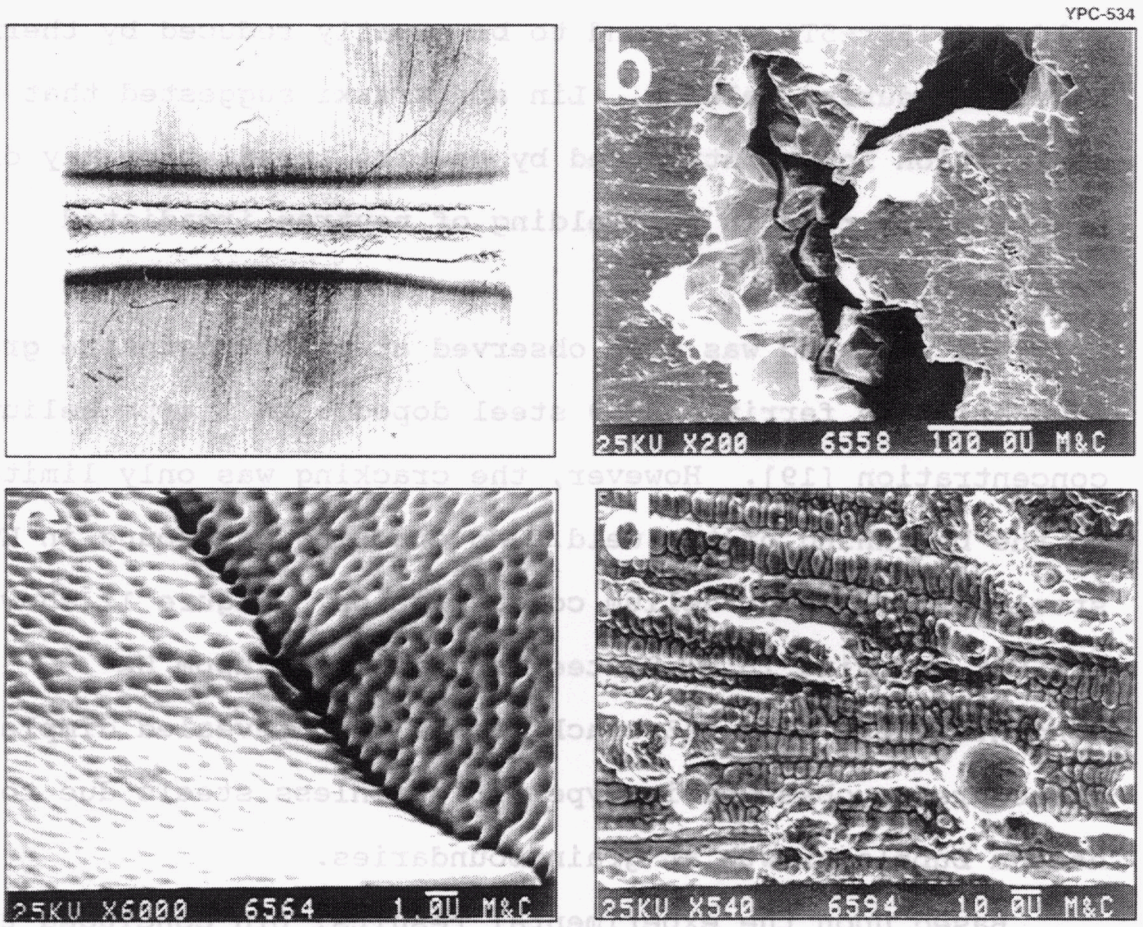

Figure 10. Structure of as-welded type 316 stainless steel with 105 appm helium. (a) Brittle fracture in fusion and heat-affected zones, (b) HAZ intergranular fracture, (c) Dimple structure on the HAZ fracture surfaces, (d) Fusion zone interdendritic fracture surfaces [19].

susceptible to fusion zone cracking than helium-doped type 316 stainless steel, which did not crack in fusion zone with 27 appm He concentration. Weld cracking observed in helium-doped V-15Cr-5Ti is shown in Figure 11. Compared to the as-doped alloy, the dislocation loop density in the matrix of welded V-15Cr-5Ti was found to be greatly reduced by thermal annealing during welding. Lin and Braski suggested that the dislocation loops introduced by neutron irradiation may only play a minor role in the welding of neutron irradiated materials.

HAZ cracking was also observed at prior-austenite grain boundaries in ferritic HT-9 steel doped with 1 appm helium concentration [19]. However, the cracking was only limited to the beginning of the weld. No cracking was found in HT-9 steel with 0.3 appm helium concentration. Figure 12 shows the HAZ cracking in HT-9 steel containing 1 appm He concentration. The HAZ crack facets also revealed dimple structure as observed in type 316 stainless steels due to helium bubble growth at grain boundaries.

Based upon the experimental results, Lin concluded that a critical combination of high temperature and stress is the key factor in controlling the severe cracking during welding. The grain boundary helium bubbles, which nucleated and formed during the charging period, grow rapidly during welding until the reduced contact areas of the grain

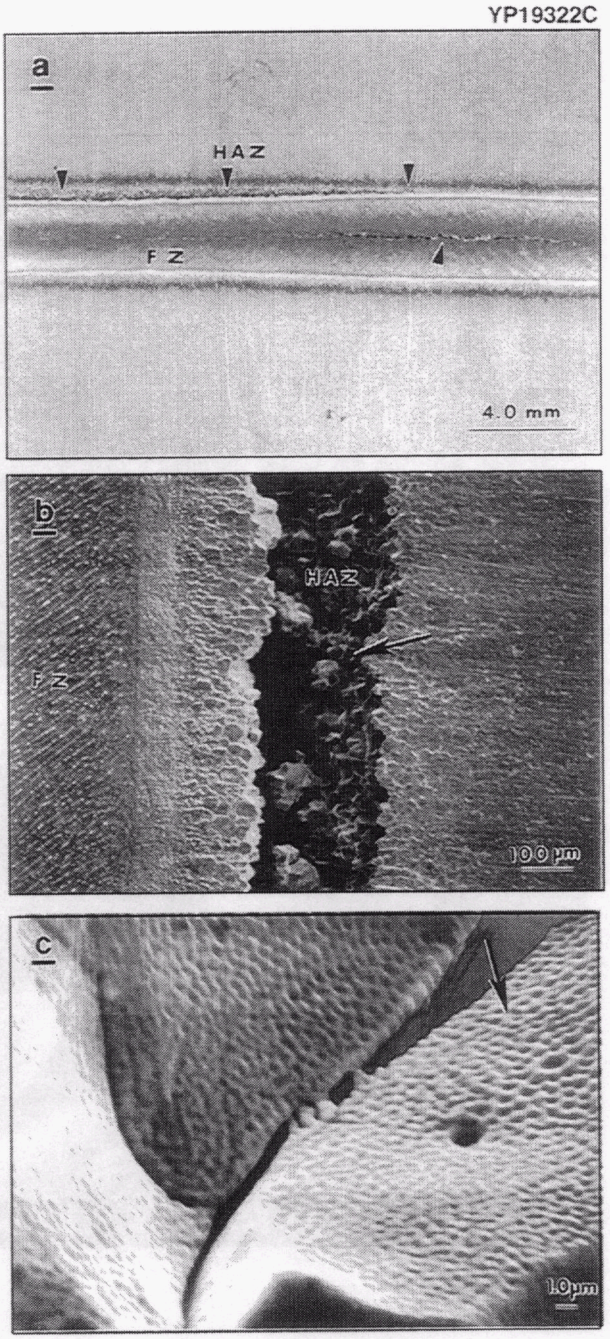

Figure 11. Microstructure of as-welded helium-doped V-15Cr-5Ti alloy. (a) Welding cracking in fusion and heat-affected zones, (b) SEM micrograph of HAZ intergranular fracture, (c) Dimple structure on the HAZ fracture surfaces [96].

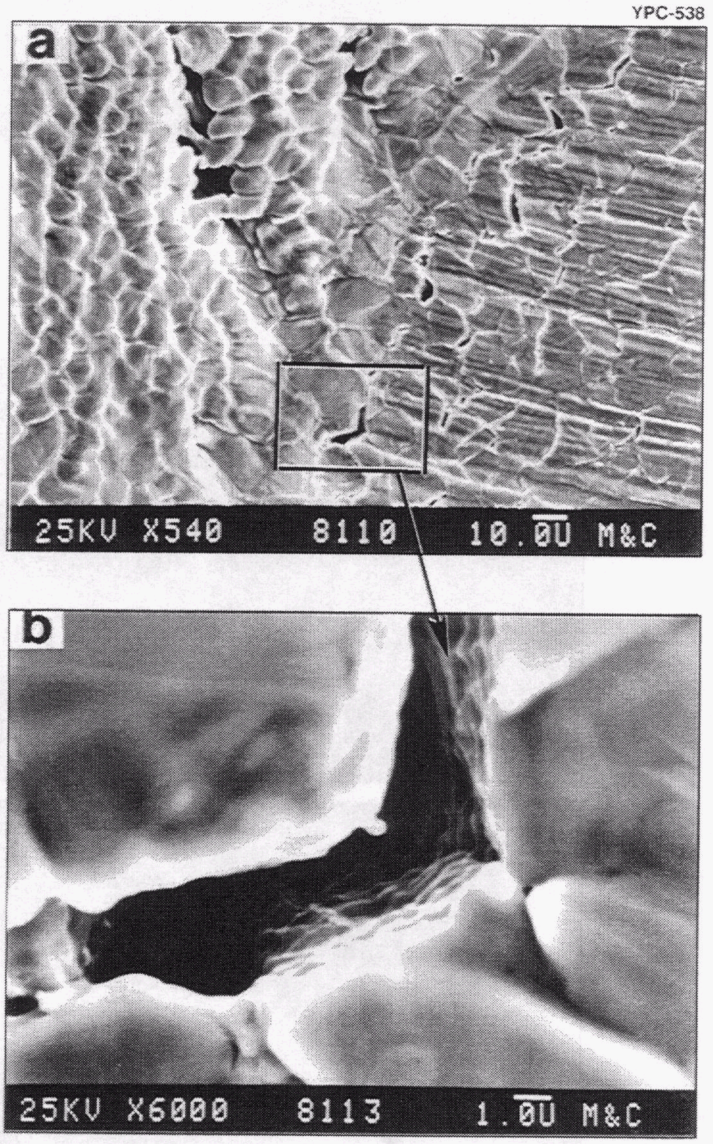

Figure 12. Structure of as-welded HT-9 with 1 appm He. (a) Intergranular fracture along prior-austenite grain boundaries, (b) Grain boundary facets decorated with uniformly distributed dimples [19].

boundaries can no longer bear the shrinkage-induced tensile stress and lead to the final brittle rupture.

Evidence has been shown in a high temperature aging experiment to support the finding of the effect of stress on weld cracking [19]. TEM disks and tensile test specimens of type 316 stainless steel containing 256 appm helium were heat treated at 800, 900, 1050 and 1300°C for one hour. Results of the TEM observation on these aged materials are shown in Table 4. In general, helium bubbles decreased in density and increased in size with increasing aging temperature. At higher temperature, thermal vacancy concentration and diffusivity are both increased and enhance the bubble coalescence and growth. No cracking was observed in all the aged materials. This was consistent with the hypothesis that the high temperature alone is not sufficient to cause the cracking during welding. Results of tensile tests revealed ductile transgranular fracture for the materials aged below 1300°C. Contrarily, it was predominantly intergranular fracture for specimens aged at 1300°C, and the fracture surfaces were decorated with dimples due to helium bubble growth at grain boundaries. All specimens maintained relatively high total elongation, greater than 35%, while the welded specimens generally failed with less than 2% elongation as shown in Table 2. Figure 13 shows the tensile properties of type 316 stainless steel containing 256 appm He after one hour aging.

Table 4

Helium bubble density and size after one hour aging at high temperature for type 316 stainless steel containing 256 appm He [19]

Temperature (°C)	σ_m ($10^{20}/m^3$)	D_m (nm)	σ_{gb} ($10^{14}/m^3$)	D_{gb} (nm)
1300	0.11	86.5	0.31	124.9
1050	2.01	39.5	0.56	39.0
900	2.30	13.0	0.57	18.3
800	4.20	7.8	4.10	5.3

σ_m = density of matrix helium bubble
D_m = diameter of matrix helium bubble
σ_{gb} = density of grain boundary helium bubble
D_{gb} = diameter of grain boundary helium bubble

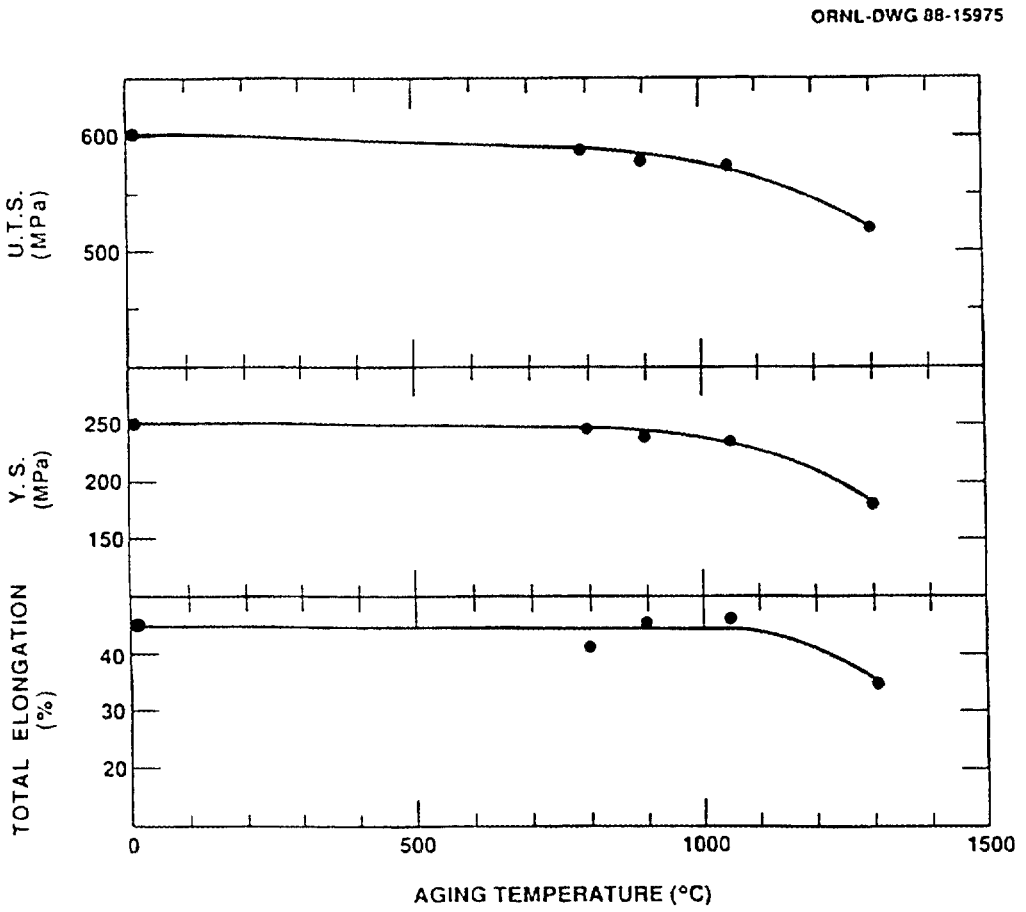

Figure 13. Results of room temperature tensile tests of type 316 stainless steel containing 256 appm helium after aging [19].

Results from a welding simulation reported by Robinson [97] provided further evidence of the combined effects of high temperature and stress on weld cracking. Type 304L stainless steel containing 256 appm He, by tritium charging and decay, was subjected to transient thermal cycles similar to that which occurred in the HAZ of a GTA welding process. The experiment was carried out using a Gleeble 1500 testing machine with various peak temperatures. Room temperature tensile tests on the simulated HAZ structure showed no sign of deterioration in properties for steel subjected to 1073K peak temperature thermal cycles. The fracture surfaces exhibited 100% ductile mode with fine uniform dimples on large shear lips. However, severe property degradation was observed when peak temperature was increased to 1473K and the fracture mode became 90% intergranular with little reduction in area as shown in Figure 14. The fracture facets were decorated with dimples due to grain boundary helium bubble growth. Higher peak temperature not only increased thermal vacancies, it also increased thermal stress and enhanced the bubble growth rate.

Reduction of Weld Cracking

Cracking susceptibility of helium-charged type 304 stainless steel is reduced by using a low heat gas metal arc (GMA) weld overlay technique [12-15,98]. Figure 15 shows a schematic representation of the weld overlay process. Welds

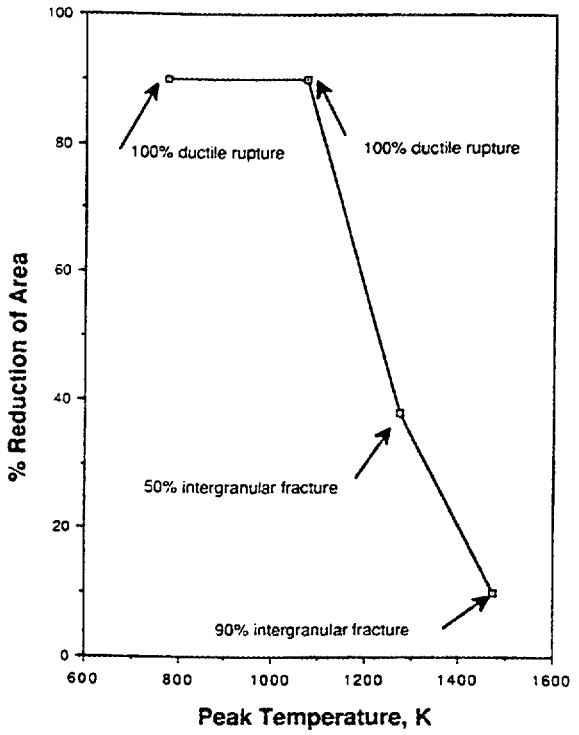

Figure 14. Percentage of reduction of area as a function of peak annealing temperature in helium charged type 304L stainless steel [97].

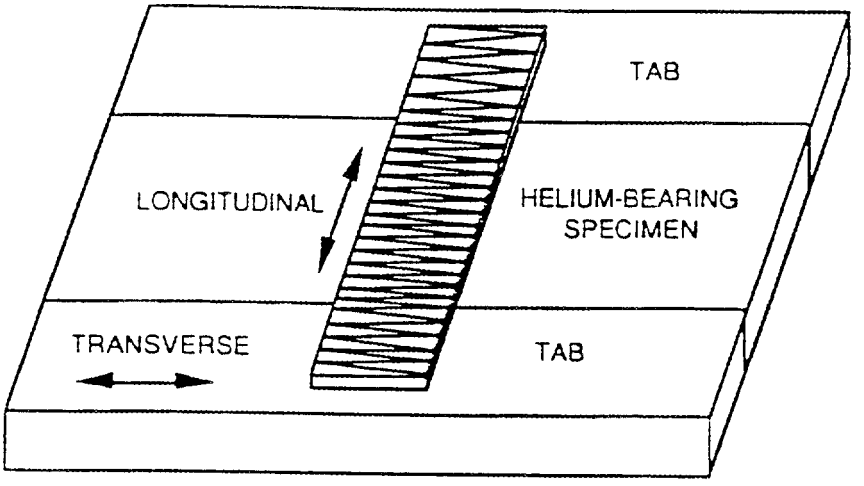

Figure 15. Schematic representation of weld overlay process [98].

were produced using 38 to 64 J/mm^2 heat inputs on steel charged with He ranging from 2.7 to 221.1 appm. The weld penetration into the underlying base metal produced by this process was only about 0.076 mm. This low penetration weld was intended to minimize the volume of material beneath the weld that was heated to high temperature. The shrinkage stresses generated by the overlay weld were considerably different from those established by the conventional welding processes. Metallography results showed that toe-cracking experienced in the conventional stringer welds was eliminated by the overlay technique. In spite of no toe-cracking, underbead intergranular cracking was observed and became significant with higher helium concentrations.

Room temperature tensile tests of the overlay welds were also reported by Kanne et al. [15] The axis of tensile specimens, 3.175 mm in diameter by 12.7 mm long gage section, was perpendicular to the weld overlay surface. Studs were resistance welded onto the overlay surface before specimens were machined. The yield strength changed slightly with increasing He concentration while the ultimate tensile strength decreased slowly to about half of the initial value as shown in Table 5. A sharp drop in reduction of area was observed for type 304 stainless steel with about 35 appm helium concentration. Specimens failed in a completely brittle fracture mode when the helium concentration increased to 221.1 appm as shown in Figure 16.

Table 5

Results of tensile test of overlay weld for type 304 stainless steel [15]

Helium Content (appm)	Samples Averaged (No.)	Yield Strength (Ksi)	Ultimate Strength (Ksi)	Elong.@ Max. Load (%)	Elong.@ Max. Load (%)	Reduction of Area (%)
0	1	52.9	90.0	27.7	42.1	81.6
3	3	54.2	84.2	16.8	36.6	78.8
9	2	56.4	88.2	16.9	30.9	68.8
17	3	53.2	86.3	19.3	36.6	76.6
22	2	58.3	87.8	18.7	33.2	65.5
49	4	58.4	84.4	10.8	11.4	27.2
85	2	58.0	70.5	4.1	4.1	7.1
147	3	49.0	54.4	1.6	1.6	7.8
220	1	43.3	44.1	0.5	0.5	0.0

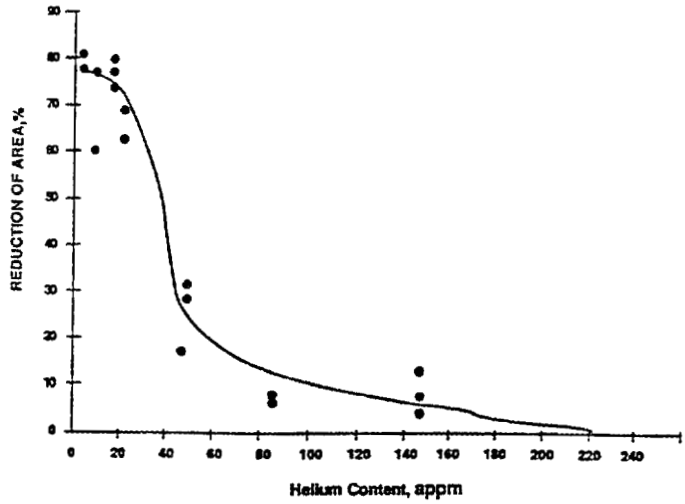

Figure 16. Effect of doped-helium on the tensile test reduction of area in type 304 stainless steel [15].

The pronounced drop in reduction of area was attributed to the change in failure location from base metal to heat-affected zone, where excessive bubble growth occurred.

Similar results were also observed by Goods and Karfs [98] using the same shallow penetration overlay process on type 304 stainless steel charged with helium ranging from 2.7 to 85 appm. In their process, a 0.6 to 1.5 mm thick GMA "pad" of filler metal, type 308L stainless steel welding wire, was welded onto the helium-bearing material. Low heat inputs, 54.4 and 60.5 J/mm^2, were used in the welding process. The resulting fusion boundary penetrated only 0.1 to 0.2 mm into the underlying metal. Extensive heat-affected zone cracking was observed in all the welds. Cracks were intergranular and preferentially oriented normal to the overlay fusion boundary. Detailed SEM examinations revealed dimple structure on the HAZ crack facets, a characteristic of high temperature helium-induced weld cracking. Figure 17 shows the transverse section of HAZ cracking below the weld overlay in type 304 stainless steel with 85 appm He concentration. Cracking was also found to extend into the weld overlay itself. Fusion zone cracking also exhibited dimple structure. However, the extent of weld cracking was significantly reduced compared to that of the conventional stringer bead welds as shown in Figure 18. No toe cracking in overlay welds was observed as in the other studies using the same technique [12-15]. Goods

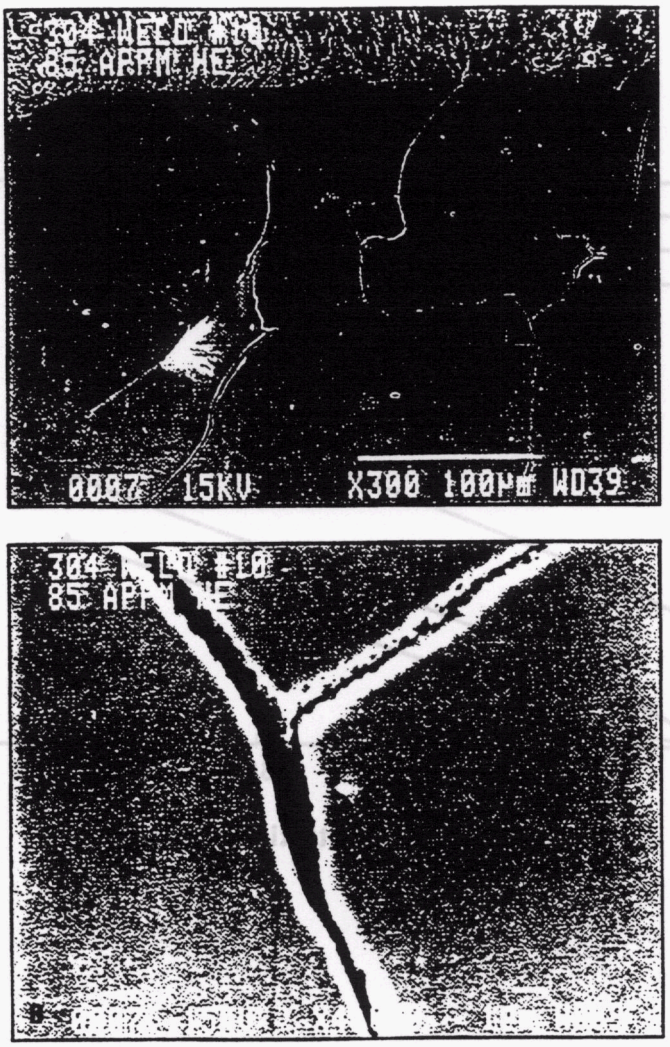

Figure 17. Underbead cracking in the overlay welding process. (a) Intergranular HAZ cracking, (b) Intergranular facets reveal dimple structure at higher magnification [98].

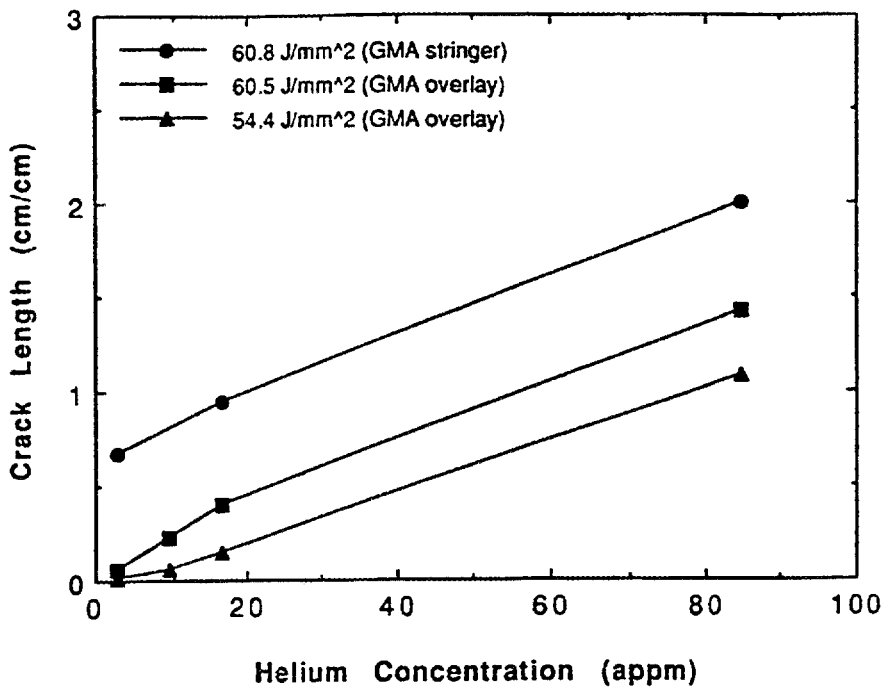

Figure 18. Total weld cracking is effectively reduced in overlay welding process compared to conventional stringer bead welding process [98].

and Karfs also demonstrated that the extent of weld cracking depended upon the heat input: the higher heat input during welding the more severe weld cracking. Conventional stringer bead welding results in deeper penetration and higher shrinkage stresses and therefore is more susceptible to weld cracking.

The cracking tendency during welding of helium-bearing materials varies from alloy to alloy. Microstructure, chemical composition and fabrication processes all contribute to the susceptibility of weld cracking [19]. Table 6 gives a comparison for various alloys on the GTA weld cracking tendency. Among which type 304 stainless steel produced using rapidly-solidified-processing (RSP) shows best resistance to the helium-induced weld cracking, while solution annealed type 316 stainless steel the worst. The comparison of HAZ cracking among different alloys is shown in Figure 19.

Table 6

Comparison of helium-induced weld cracking tendency among various alloys [19]

Alloy	He (appm)	Crack Length (mm/mm)	Tendency
SA 316 SS	2.5	0.79	High
20%CW 316 SS	2.0	0.06	Low
SA PCA	2.0	0.0017	Very Low
RSP 304 SS	7.0	0.0	None
HT-9	1.0	0.009	Very Low

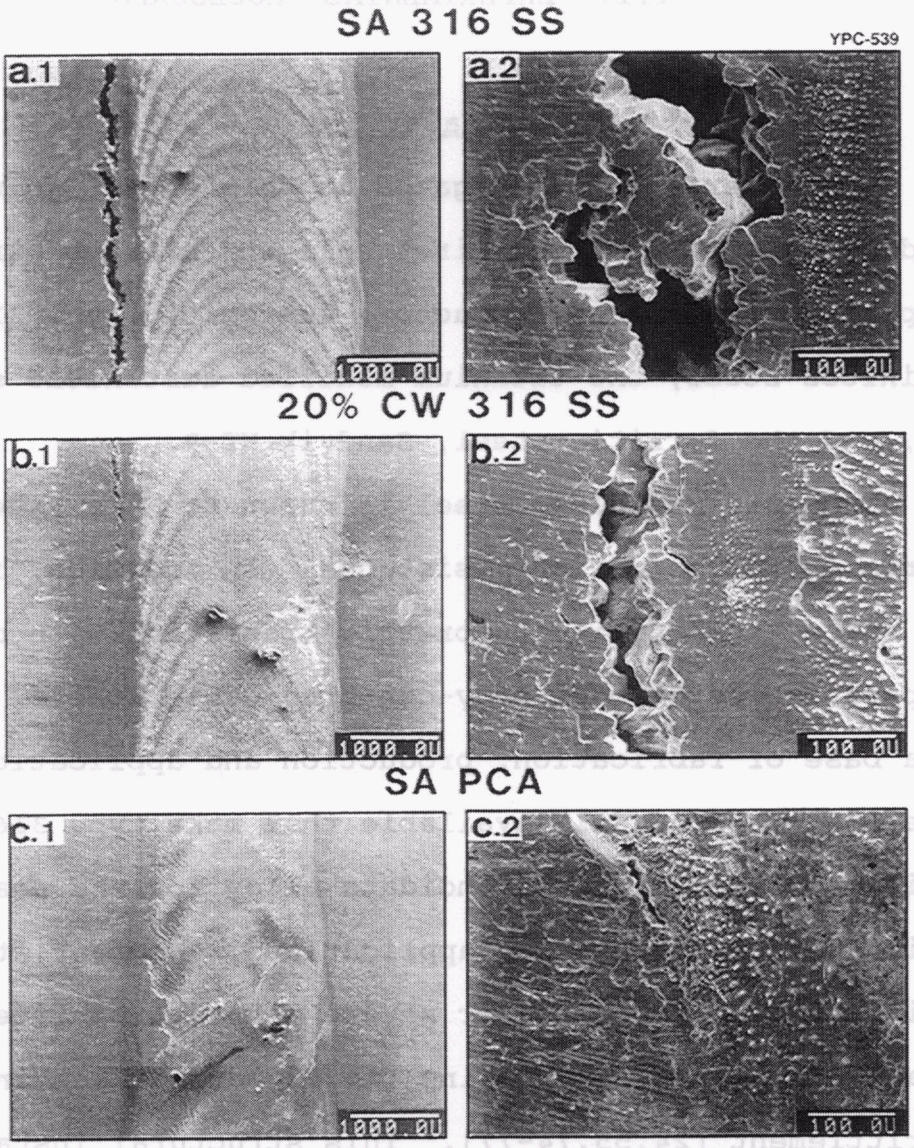

Figure 19. Comparison of weld cracking tendency of austenitic stainless steels containing 2 appm helium. (a) Solution annealed type 316 stainless steel, (b) 20% cold-worked type 316 stainless steel (c) Solution annealed prime candidate alloy [19].

III. EXPERIMENTAL PROCEDURES

Materials

The materials investigated in this study include three candidate alloys for the first wall and blanket structural components for a fusion reactor: austenitic type 316 stainless steel, the titanium modified austenitic steel, PCA, and the ferritic steel, Sandvik HT-9.

Type 316 stainless steel is known to have excellent corrosion and oxidation resistance. In addition, it does not suffer the ductile-to-brittle transition with decreasing temperature as do most body-centered-cubic steels. A large data base of fabrication, production and application experience are readily available that make type 316 stainless steel a major candidate alloy for the near-term fusion reactor structural applications. However, type 316 stainless steel does suffer severe degradation after neutron irradiation, such as swelling [24,72] and helium-induced embrittlement [24,55,74-77]. This structural instability has lead to the development of the titanium modified austenitic steel, PCA. The finely dispersed precipitates, titanium carbides, within PCA trap helium bubbles and reduce the bubble growth rate and stabilize the structure. Similar

radiation resistance is found in ferritic steel, HT-9. Voids and helium bubbles are trapped by the subgrain lath structure, dislocations, and carbide precipitates. Furthermore, HT-9 steel also shows higher thermal conductivity and lower thermal expansion than austenitic stainless steel, which are favored in a fusion environment. The chemical compositions of the three alloys are shown in Table 7.

All materials investigated in this study were 0.76 mm thick sheet metals. Type 316 stainless steel from the Liquid Metal Fast Breeder Reactor (LMFBR) program, heat 8092297, was used in this experiment. The steel was solution annealed at 1050°C for one hour in an inert atmosphere. PCA was solution annealed for one half hour at 1100°C, aged eight hours at 800°C, and then received a 25% cold roll into the final 0.76 mm thickness. HT-9 steel, Combustion Engineering Co. heat 9607-R2, was solution annealed at 1050°C for one half hour in an inert atmosphere and then air cooled. The steel was then tempered at 700°C for one hour in an inert atmosphere followed by air cooling. Tempered martensite was obtained for HT-9 steel after these treatments. Table 8 shows the processes of heat treatment received by materials investigated in this study.

Table 7

Chemical compositions of type 316 stainless steel (Reference Heat 8092297), HT9 (Heat 9607-R2) and PCA steels

Element(wt%)	316 SS	PCA	HT9
C	0.057	0.05	0.2
Mn	1.86	1.7	0.57
Si	0.58	0.4	0.17
Ni	13.48	16.2	0.51
Cr	17.25	14.0	12.10
Mo	2.34	2.4	1.04
V	--	--	0.28
P	0.024	0.01	0.016
S	0.019	--	0.003
Ti	0.02	0.24	0.001
N	0.03	--	0.027
W	--	--	0.45
Al	--	--	0.006
Co	0.02	--	--
Cu	0.10	--	--
Pb	0.003	--	--
Sn	0.004	--	--
B	0.0005	--	--
Fe	Balance	Balance	Balance

Table 8

Heat treatment processes

Steel	Heat Treatment
316 SS	solution annealed 1 h at 1050°C
PCA	solution annealed 0.5 h at 1100°C + aged 8 h at 800°C + cold worked 25%
HT-9	solution annealed 1 h at 1050 °C + tempered 1 h at 700°C

Helium-Doping Process

In order to reduce the radiological hazard and difficulty of hot cell operations, the tritium trick technique [99-102] was used to introduce helium into alloys to study the effects of helium on irradiated materials. In this technique, tritium was first charged into specimens at elevated temperature in a pressurized vessel and then allowed to decay into helium. Tritium is chemically identical to hydrogen and has a high diffusivity in metals. Therefore, it is relatively easy to diffuse tritium into alloys at elevated temperature and under pressurized conditions. Although radiation damage in neutron irradiated materials is far more complicated than in the tritium charged alloys, it is considered an advantage to isolate the helium effects from the others such as the displacement damage.

Helium is generated by tritium decay according to the following reaction:

$$^{3}H \rightarrow {}^{3}He + \beta^{-} \qquad (7)$$

The radioactive half life of tritium is 12.34 years. The beta particles from the above reaction have an average energy of 5.6 keV and a maximum energy of 18.6 keV. The recoil energy, about 14 eV, associated with the beta decay from tritium is negligible. This energy is well below the

threshold energy required to cause atomic displacement in most metals. Figure 20 shows a schematic representation of the helium doping process.

The following radioactive decay equation is used to calculate the helium concentration of a tritium charged specimen:

$$-(dN/dt) = \lambda N \tag{8}$$

where

N = total number of tritium atoms,

t = decay time,

λ = decay constant, $0.693/t_{\frac{1}{2}}$,

$t_{\frac{1}{2}}$ = tritium half life, 12.34 years.

Therefore, the helium concentration resulting from tritium decay can be expressed as,

$$[He]_t=[T]_i\{1-\exp(-\lambda t)\} \tag{9}$$

where:

$[He]_t$ = He concentration after time t, appm,

$[T]_i$ = initial tritium concentration, appm.

In this study the tritium was introduced into alloys at 371°C and 0.8 MPa pressure. Tritium concentration will

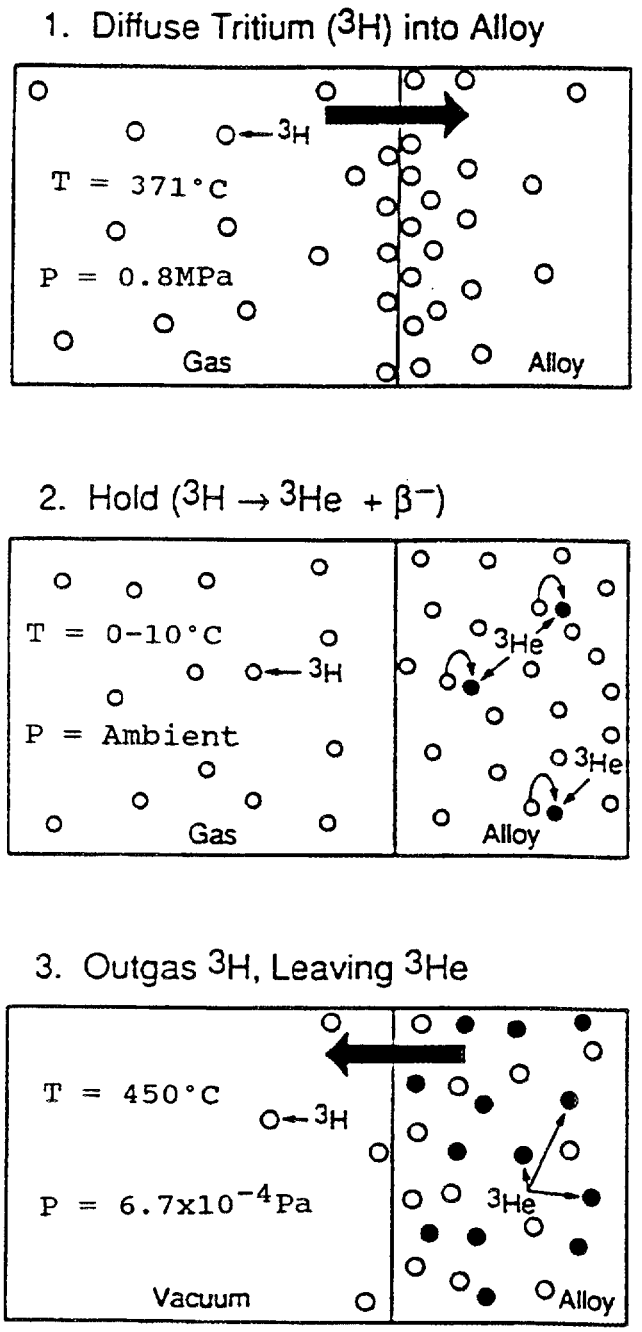

Figure 20. Schematic representation of the helium doping process.

reach saturation in the alloys within a few hours under these conditions. After tritium charging, the alloys were kept at low temperature, about 0°C, until the desired helium concentrations were obtained and then the excessive tritium was removed by placing the specimens in a vacuum vessel at 450°C and 6.7×10^{-4} Pa pressure. Helium-doping conditions is listed in Table 9.

It is necessary to mention that after the completion of the helium-doping process, severe tritium contamination was found on the material surfaces. This is attributed to tritium being entrapped in the oxide layers on the material's surface. The surface contamination was found to be very resistant to removal. The author found that the most effective way to reduce the surface contamination was to physically remove the surface oxide layers by grinding with SiC paper.

The concentration of helium, ^3He, generated by tritium decay was determined by gas mass spectrometry [103-105]. All the helium analyses in this study were performed by Rockwell International, Canoga Park, CA. At least two duplicate specimens were examined for each specimen to investigate the analysis reproducibility and helium homogeneity. Helium, ^3He, was extracted by fusing the helium-containing alloys in the mass spectrometer system's high-temperature vacuum furnace. By adding a known quantity of ^4He as a spike and measuring the ratio between ^3He and

Table 9

Helium doping conditions

Batch No.	Predicted He in 316 SS (appm)	Charging Pres. (MPa)	Charging Temp. (°C)	Decay Time (day)
1	0.7	0.8	371	30
2	1.4	0.8	371	60
3	4.2	0.8	371	180
4	8.4	0.8	371	360

a. Excessive tritium were removed at 450°C and 6.7×10^{-4} Pa.

^4He, the helium content generated from tritium decay can be obtained along with the known specimen weight. The mass spectrometer was calibrated for mass sensitivity during each series of runs by analyzing known mixtures of ^3He and ^4He.

Gas Tungsten Arc Welding Process

According to the model proposed by Lin et al. [16,19], the growth of grain boundary helium bubbles should be significantly reduced by a change in the stress state during cooling of a weld. To investigate this hypothesis, a hydraulic weld plate fixture system, as shown in Figure 21, was constructed to enable applying a controlled compressive stress perpendicular to the weld during welding.

Single pass gas tungsten arc (GTA) welding was conducted under constrained conditions to simulate the structural restraint encountered in practical repair and maintenance. Welding was performed at 10 V-DC and 24 A for type 316 stainless steel and PCA, while the welding current was increased to 28 A for HT-9 steel. The torch travel speed was 3.2 mm/s. Welding was performed under a protective argon atmosphere with a gas flow of 1.57×10^{-4} m^3/sec from the torch and 7.87×10^{-5} m^3/sec from the back of the weld plates. Full penetration welds were made using 2% thoriated tungsten electrodes 1.6 mm in diameter. Specimen surfaces were cleaned with acetone before welding to prevent contamination. Two plates, start and runoff plates, of

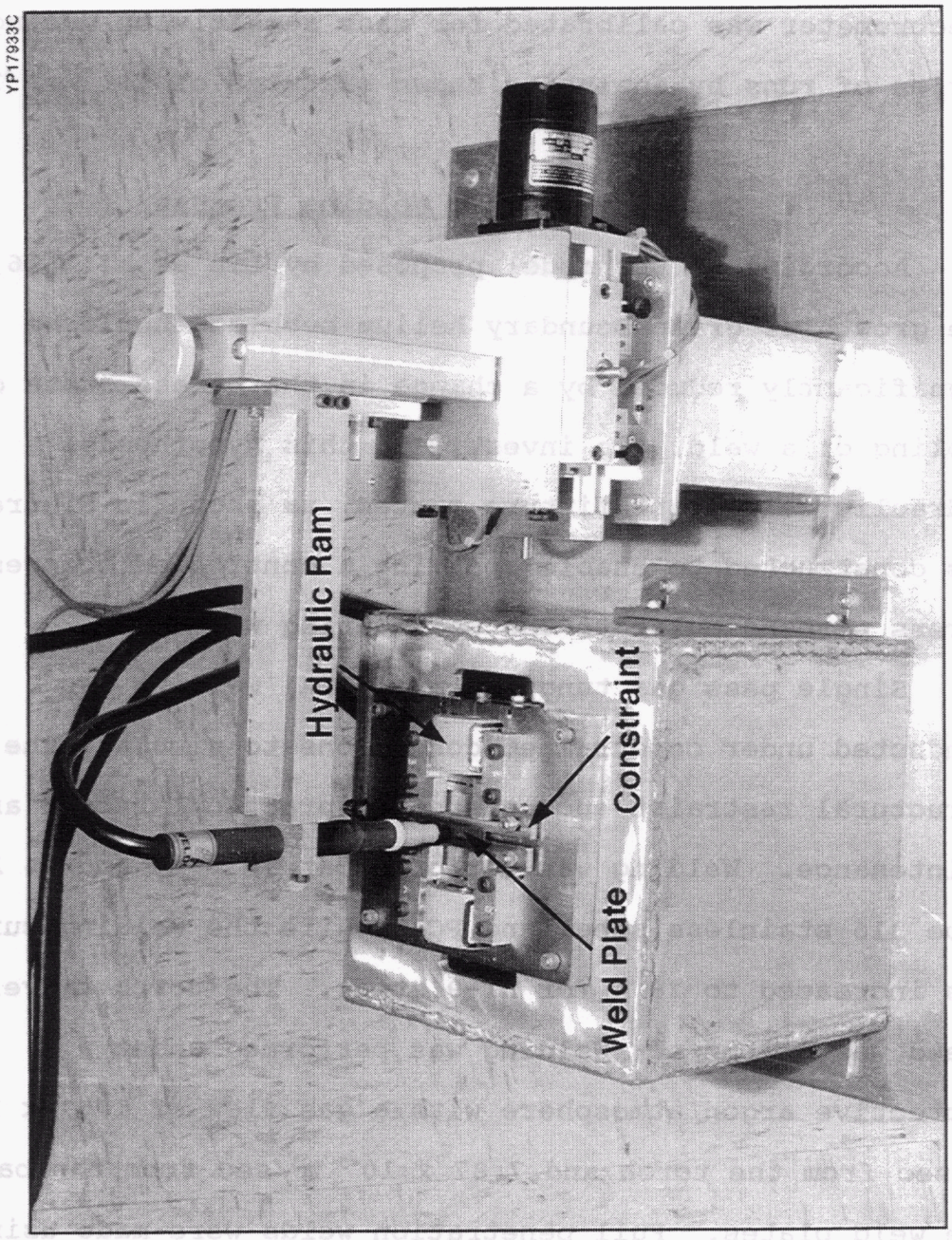

Figure 21. Hydraulic weld plate fixture system.

similar material were placed in front and back of the weld plates so a uniform weld could be obtained for the entire length of helium-containing plates. The resulting heat input was 75.6 J/mm for type 316 stainless steel and PCA whereas it was 88.2 J/mm for HT-9 steel. The heat input produced a full penetration weld approximately 3 mm wide. Table 10 shows the machine settings used for this study on the Miller 300P welding power supply (by Miller Electric MFG. Co., Appleton, WI). The gas tungsten arc welding parameters used to produce full penetration welds for various steels are shown in Table 11.

Temperature Measurement during Welding

As described in the previous section, the combined action of high temperature and thermal stress causes severe weld cracking during welding of helium-containing materials. Welding inevitably introduces thermal stresses due to the expansion and contraction of the weld plate as temperature changes throughout the process. It is, therefore, necessary to analyze the dynamic changes of temperature during welding to enable the calculation of thermal stress and hence the grain boundary bubble growth.

K-type thermocouples, Chromel and Alumel, were used to measure the temperature profile at the heat-affected zone during welding. Thermocouple junctions were spot welded onto the type 316 stainless steel before welding. The

Table 10

Welding power supply settings

AC/DC Polarity	DCEN
Voltage Range	5-50
Start Adjustment	2
High Frequency	Start
Overload Control	On
Remote Amperage Control	Remote
Contactor Control	Remote

Table 11

Gas tungsten arc welding parameters

Voltage	10 V-DC
Current	
Type 316SS, PCA	24 A
HT9	28 A
Torch Speed	3.2 mm/s
Gas Flow	
Top	1.57×10^{-4} m^3/s
Bottom	7.87×10^{-5} m^3/s
Tungsten Electrode	1.6 mm dia.
	2% thoriated

junction was carefully positioned such that it was very close to the fusion boundary but did not break off of the plate during welding. Voltage readings from the thermocouple were acquired and stored dynamically in the memory of a Nicolet 3091 digital ocilliscope (by Nicolet Instrument Corp., Madison, WI.) during welding. The data were later retrieved from the ocilliscope memory using a personal computer for temperature conversion via an RS-232 serial connection as described in appendix A.

Mechanical Properties Characterization

Tensile Tests

Sheet tensile tests were conducted to investigate the mechanical properties of the welds. Sheet tensile specimens across the weld were produced using a punch and die. The tensile axis was perpendicular to the welding direction. The weld was in the center of the gauge section, 7.62 mm long by 1.52 mm wide by 0.76 mm thick. Figure 22 shows the schematic for the sheet tensile specimen, fusion program type SS-3.

Tensile properties are known to be sensitive to the strain rate, defined as the ratio of crosshead speed divided by the gage length, during tensile tests. Materials subjected to a higher strain rate tend to have higher yield strength and ultimate tensile strength. Ductility, on the other hand, typically decreases as strain rate increases,

ORNL-DWG 84-14010R

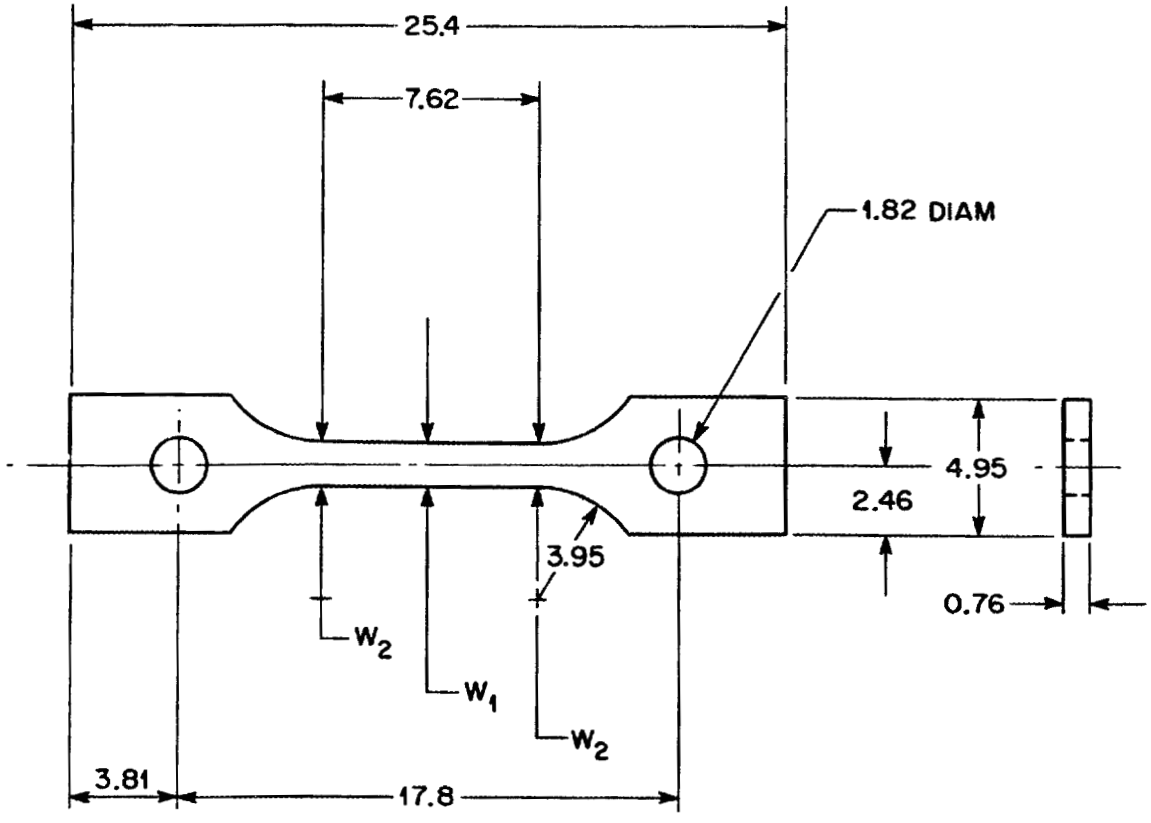

W_1 = 1.52 mm
W_2 = 0.025 TO 0.038 mm
GREATER THAN W_1

DIMENSIONS IN MILLIMETERS

Figure 22. Schematic representation of an SS-3 tensile specimen.

and materials are prone to fail by brittle fracture. In this study, tensile tests were performed with a strain rate of 5×10^{-4} s^{-1}. All tests were conducted at room temperature.

Microhardness Tests

Diamond pyramid microhardness (DPH) was measured across the weld to evaluate the microstructure-property relationship. The measurement of microhardness also gives an indication of the effect of helium on the strengthening of materials. A Micromet 3 microhardness tester (by Buehler Ltd., Lake Bluff, IL) was used with 500 grams load and 15 seconds dwell time. The spacing between each measurement was 0.203 mm, and measurements were not made closer than 0.203 mm from the specimen edges.

Microscopy

Optical Microscopy

Optical microscopy was used to examine the microstructure of the steels across the weld. Samples were cut across the weld using an Isomet diamond low speed saw (by Buehler Ltd.). Specimens were then mounted in epoxy resin and hand ground and polished before chemical etching. The etching solution for the type 316 stainless steel was a mixture of hydrochloric acid and nitric acid in a five to one ratio. PCA was electrolytically etched using a 10%

aqueous oxalic acid solution. For HT-9 steel, the etching solution was a mixture of 9% nitric acid, 1% hydrofluoric acid and 90% water by volume.

Scanning Electron Microscopy (SEM)

A scanning electron microscope, JEOL JSM-35CF (by JEOL Ltd., Tokyo, Japan), was used to examine weld integrity and fracture mechanisms. Disk specimens prepared for TEM observation were also examined using SEM to investigate the preferred orientations of grain boundary bubble growth. Cracking susceptibility of steels was evaluated based on the total crack length observed on the SEM photographs. Cavity size on the fracture surfaces was calculated from the SEM photographs to evaluate the grain boundary helium bubble growth during welding. All specimens were cleaned using methanol and acetone before examination.

Transmission Electron Microscopy (TEM)

Transmission electron microscopy was used as the primary tool for the helium bubble observation. TEM foils were prepared from the 3 mm diameter disks punched out from the heat-affected zone. The disks were carefully positioned such that the final thinned hole position would be located about 200 μm away from the fusion boundary, where the HAZ cracking was most likely to occur. The punched disks were hand ground to about 0.125 mm thick using up to 600 grit SiC

papers and then electrolytically thinned using a Tenupol 3 thinning machine (by Struers A/S, Copenhagen, Denmark). The electrolytic thinning solution was a mixture of sulfuric acid and methanol in a one to seven ratio. All thinning processes were conducted at 20 V, 120 mA and 0°C. The JEM 2000FX transmission electron microscope (by JEOL Ltd.), capable of up to 200 kV accelerating voltage, was used in this study for all the TEM examinations. Magnifications of the microscope were calibrated using a standard 60021 replica grid (2160 lines/mm).

TEM Foil Thickness Measurement

The quantitative analysis of helium bubbles requires an accurate knowledge of the TEM foil thickness. The stereo-pair technique [106-108] was used in this study for the TEM foil thickness measurement. Grain boundaries, twin boundaries and other planar defects extending through the TEM foil and showing sharp contrast were used for the foil thickness measurement.

In the stereo-pair thickness measurement technique, the incident electron beam was assumed to be parallel and therefore result in parallel projections of the object. A tilt angle of 10 degrees between micrographs was used in this study. By carefully aligning the electron beam, it was possible to have an accuracy within 5% for the foil

thickness measurement [107,108]. The TEM foil thickness, t, was calculated with the following equation:

$$t = p/(2M*\sin(\Theta/2)) \tag{10}$$

where

p = parallax of micrographs,

M = magnification of the micrographs,

Θ = the total tilt angle of the stereo pair.

The parallax, p, is an average of three measurements for each stereo pair. All the stereo-pair photographs were taken under identical diffraction conditions.

Quantitative Bubble Analysis

Helium bubbles are known to nucleate and grow preferentially at the high energy sites, e.g., stacking faults, dislocations and grain boundaries. Examinations of helium bubbles were usually conducted on TEM micrographs with under-focused images. With this focusing condition, a bubble appears as a white dot surrounded by a dark Fresnel-like ring. The bubble diameter was then measured across only the white portion of the image. The volume-average bubble diameter, VAD, was calculated according to the following equation [105]:

$$VAD = (\Sigma N_i D_i^3 / \Sigma N_i)^{1/3} \tag{11}$$

where

N_i = total number of bubbles in size class i,

D_i = mean bubble diameter of size class i.

The density of helium bubbles, ρ_b, was calculated from the following equation:

$$\rho_b = N_b / tA \tag{12}$$

where

N_b = total number of helium bubbles,

t = foil thickness,

A = area of the TEM micrograph.

IV. EXPERIMENTAL RESULTS

Temperature Profile during Welding

It is known that the welding process produces steep thermal gradients and leads to non-uniform thermal expansion. Thermal stresses, which result from the dimensional changes, cause voids/cavities at grain boundaries to grow and leads to premature failure. It is necessary to know the temperature as a function of time during welding to calculate the thermal stress, diffusivity and hence grain boundary bubble growth. The dynamic change in temperature at the heat-affected zone, T(t), adjacent to the fusion boundary, was measured using K-type thermocouples during gas tungsten arc welding.

Figure 23 shows the temperature history of a region in the heat-affected zone during GTA welding of type 316 stainless steel. Temperature was measured in the heat-affected zone at a distance of 0.25 mm from the fusion boundary. This corresponds to the region where final failure occurs in the helium containing specimens, a distance of approximately three grain diameters from the fusion boundary. The temperature data measured during welding was then curve fitted (using the Table Curve program

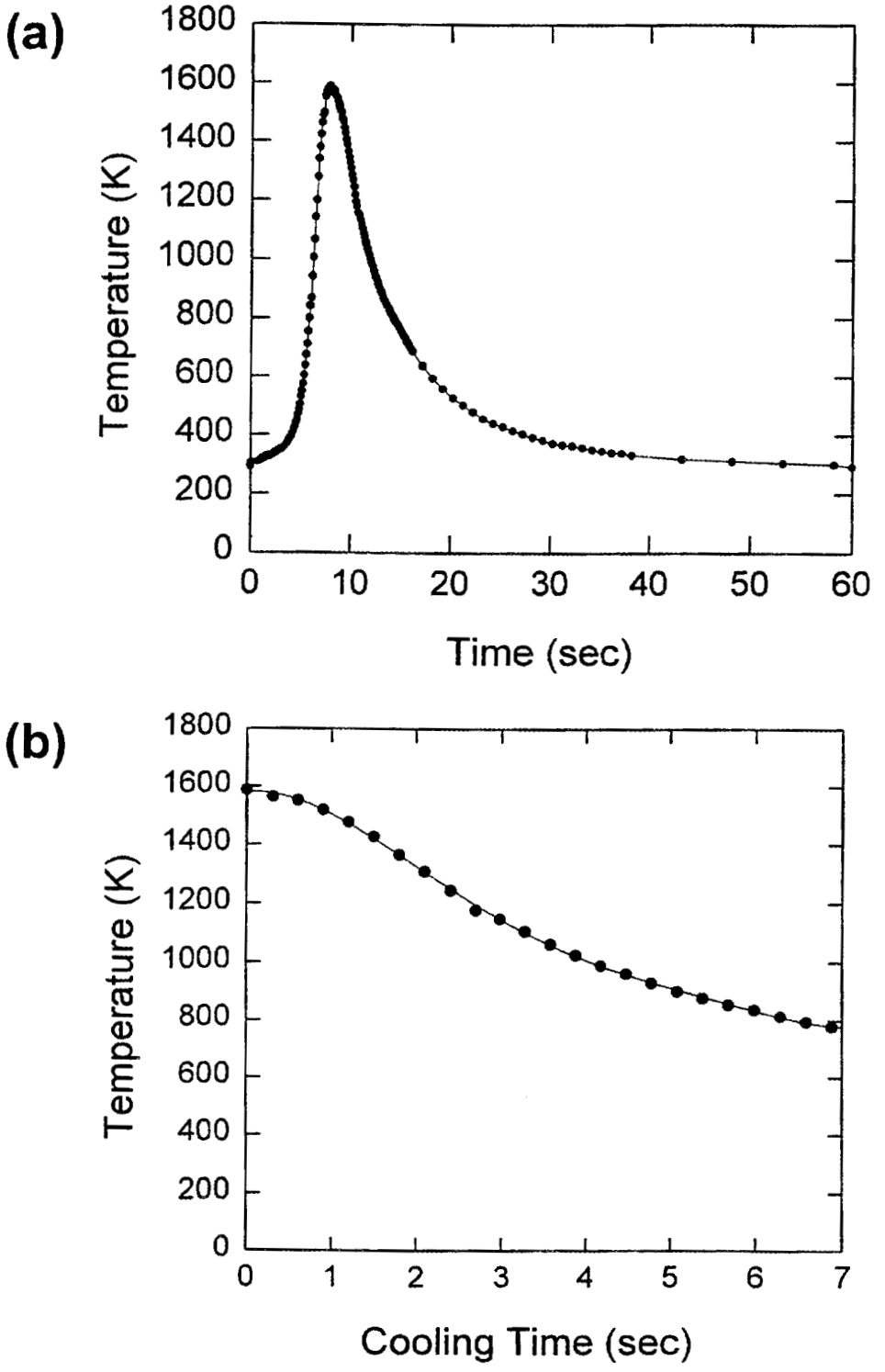

Figure 23. Temperature time history of heat-affected zone during GTA welding of type 316 stainless steel. (a) full process (b) cooling curve.

from Jandel Scientific) to obtain an equation which could then be used in the subsequent helium bubble growth analysis. The dynamic temperature history of the specified region of the heat-affected zone can be described as:

$$T(t) = \exp[(a+ct+et^2)/(1+bt+dt^2+ft^3)] \qquad (13)$$

where $T(t)$ = temperature at time t, K,

t = instantaneous time during welding, sec,

$a = 5.774993$,

$b = -0.25759204$,

$c = -1.5058468$,

$d = 0.020198644$,

$e = 0.12530994$,

$f = 9.2443251 \times 10^{-6}$.

Helium-Charging

Helium content of the tritium-tricked materials was determined by isotope-dilution gas mass spectrometry, performed by Rockwell International, Canoga Park, CA. The results of the helium measurements are given in Table 12. Helium concentrations are listed in atomic parts per million (10^{-6} atom fraction) with respect to the total number of atoms in each material. Although some significant variations were observed, the results of helium concentration measurements were in general agreement with

Table 12

Helium concentration in tritium-charged steel samples

Batch No.	Helium Concentration (appm)		
	316 SS	PCA-B3	HT-9
1	0.7	--	--
2	1.5	3.9	0.5
3	5.2	6.0	1.4
4	9.7	11.4	2.5

the preliminary estimated values based upon charging conditions. The alloy PCA-B3 had the highest helium concentration under the same doping conditions and showed the best helium homogeneity. The ferritic alloy HT-9 had the lowest helium concentration and showed some heterogeneity within individual specimens. Type 316 stainless steel showed the highest levels of heterogeneity in helium concentration within each specimen. Localized impurities which trap helium may be the cause of heterogeneity observed in helium concentrations.

Helium concentrations were also measured after welding. Specimens of welded type 316 stainless steel, containing 5.2 appm He, showed no change in helium concentration in both the heat-affected zone and base metal. However, helium concentrations decreased 21% to 4.2 appm, in the fusion zone.

Optical Microscopy

Type 316 stainless steel, heat 8092297 from the Liquid Metal Fast Breeder Reactor (LMFBR) program, was annealed at 1050 °C for one hour in an inert atmosphere. A mixture of hydrochloric acid and nitric acid in a five to one ratio was used to etch the samples for optical microstructure examinations. Figure 24 shows the as-welded austenitic structure of type 316 stainless steel after GTA welding. This particular heat of steel was found to have stringers

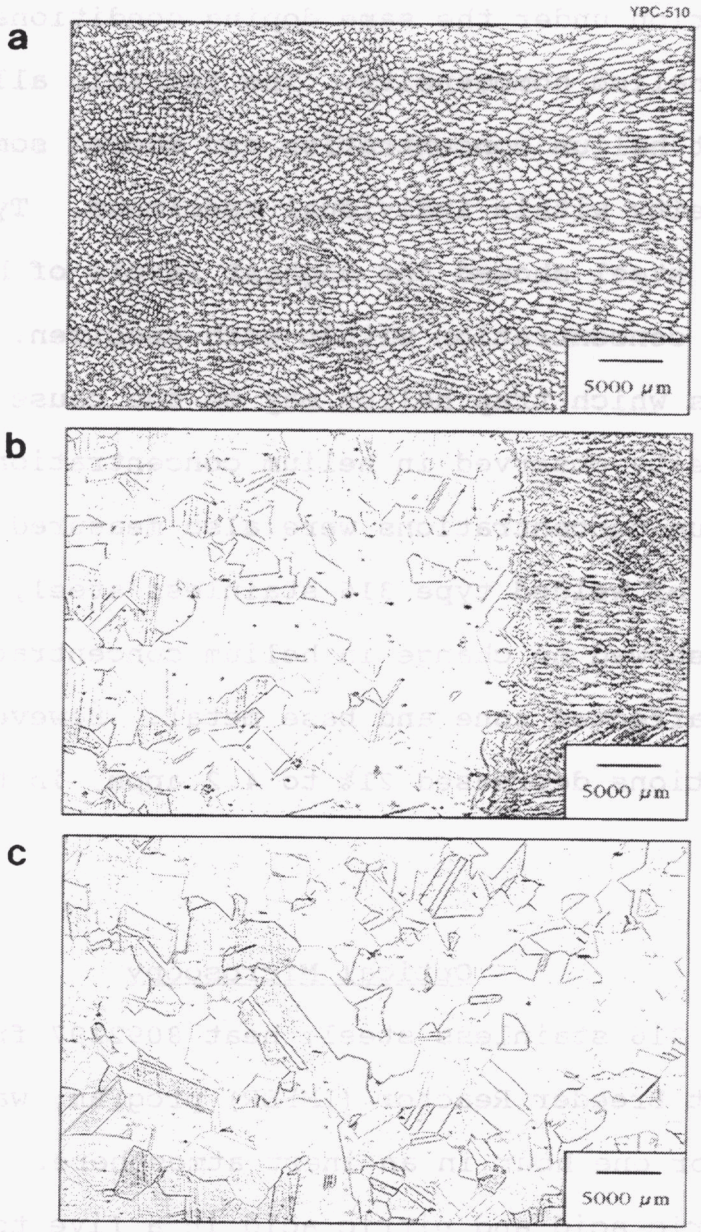

Figure 24. Microstructure of type 316 stainless steel after gas tungsten arc welding. (a) fusion zone (b) HAZ (c) base metal.

dispersed in the matrix as shown in Figure 25. They were identified as MnS_2 by x-ray microprobe analysis. The extent of this impurity varied significantly from specimen to specimen. These impurities act as nucleation sites for helium bubbles and as helium traps and are probably responsible for the heterogeneity found in helium concentration measurements.

PCA is a 14Cr-16Ni-2.5Mo-0.25Ti-0.4Si-0.55C, in weight percent, austenitic stainless steel whose composition was developed for void swelling resistance in a neutron irradiation environments [109]. The specimen group B3, composed of PCA alloy, was solution annealed for one half hour at 1100°C, aged at 800°C for eight hours, and then cold-worked 25 percent. The aging process produced dispersed fine MC precipitates which was patterned to reduce void swelling. Figure 26 shows the as-welded microstructure of PCA-B3. The solution used for etching was a mixture of hydrochloric acid and nitric acid in a five to one ratio.

HT-9 steel, heat 9607-R2, was first solution annealed at 1050°C for one half hour in an inert atmosphere then air cooled. The steel was then tempered for one hour at 700°C in an inert atmosphere and then air cooled. The resulting microstructure was tempered martensite structure as shown in Figure 27. The HT-9 was etched using a mixture of 9% nitric acid, 1% hydrofluoric acid and 90% water by volume.

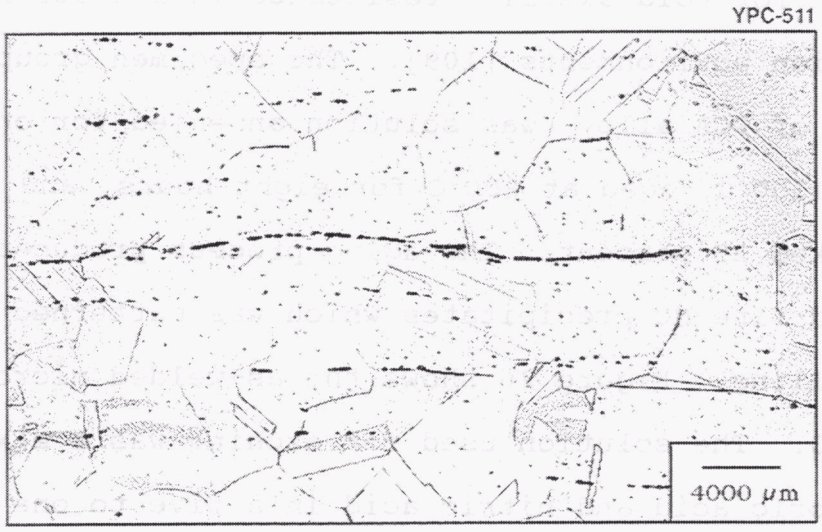

Figure 25. Type 316 stainless steel has stringers dispersed in the matrix. They were identified as MnS_2 by x-ray microprobe analysis.

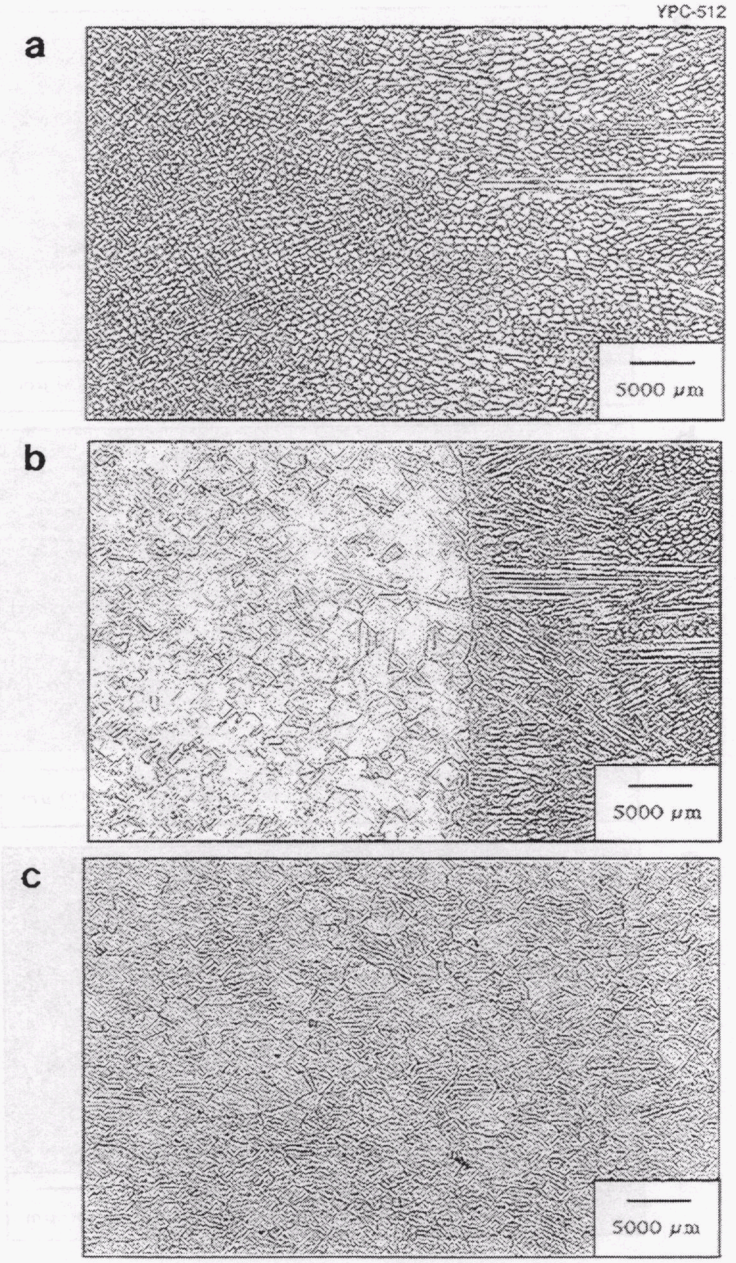

Figure 26. Microstructure of PCA-B3 alloy after gas tungsten arc welding. (a) fusion zone (b) HAZ (c) base metal.

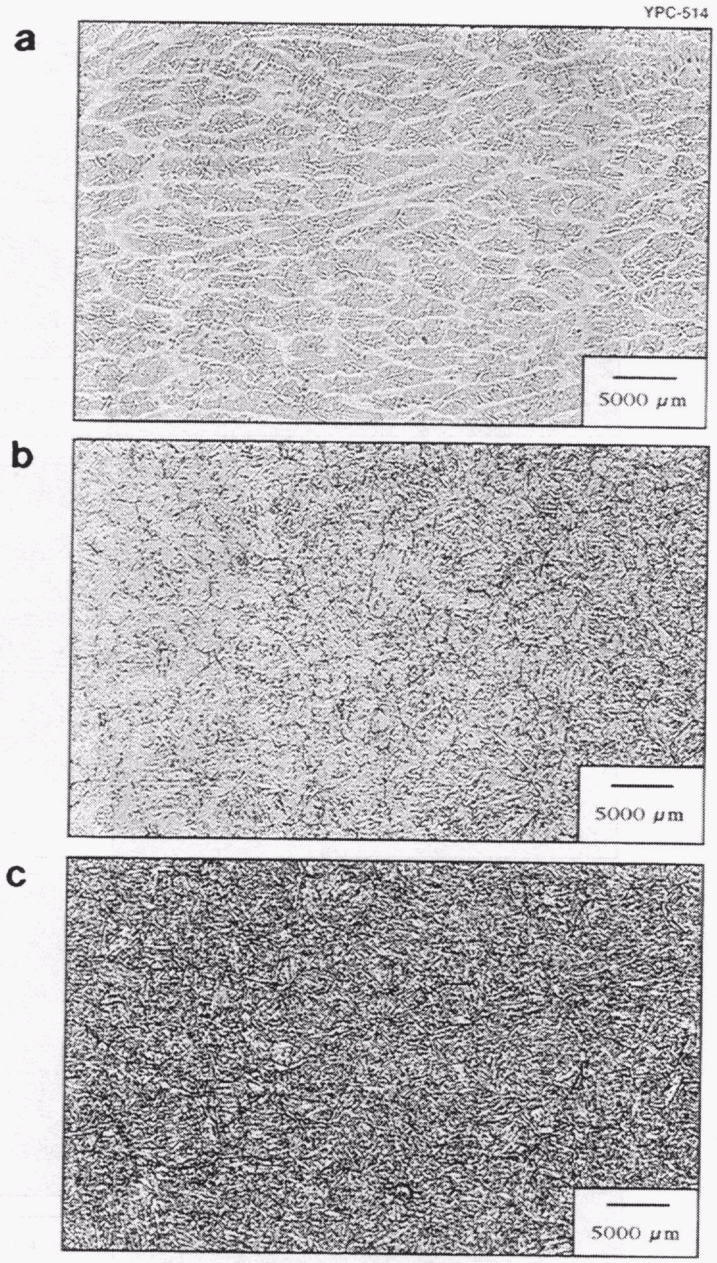

Figure 27. Microstructure of HT-9 steel after gas tungsten arc welding. (a) fusion zone (b) HAZ (c) base metal.

Weld Integrity

Autogenous bead-on-plate full penetration welds were made on all the materials using the conventional gas tungsten arc welding process in an argon atmosphere. The welding direction is normal to the material's rolling direction. An optical microscope was used initially to investigate the general integrity of a weld. Detailed analyses were later performed using scanning electron microscopy.

No cracks were found in type 316 stainless steel with 0.7 appm He following the standard GTA welding process, while severe heat-affected zone cracking, visible to the naked eye, occurred in steels with helium concentrations of 1.5 appm. Catastrophic fusion zone cracking was found in steels containing 5.2 and 9.7 appm helium. Figure 28 shows the weld cracking of type 316 stainless steel containing 5.2 appm helium using the standard GTA welding process.

The extent of cracking varied from weld to weld. Fusion zone macrocracks, visible to the naked eye, varied from 0 to 72% of the total weld length, while heat-affected zone macrocracks varied from 0 to 84% of the total weld length as helium concentrations increased from 0.7 to 9.7 appm. Microcracks, as shown in Figure 29, were always distributed in the heat-affected zone parallel to the welding direction about 200 μm from the fusion boundary in standard welds of type 316 stainless steel. The overall

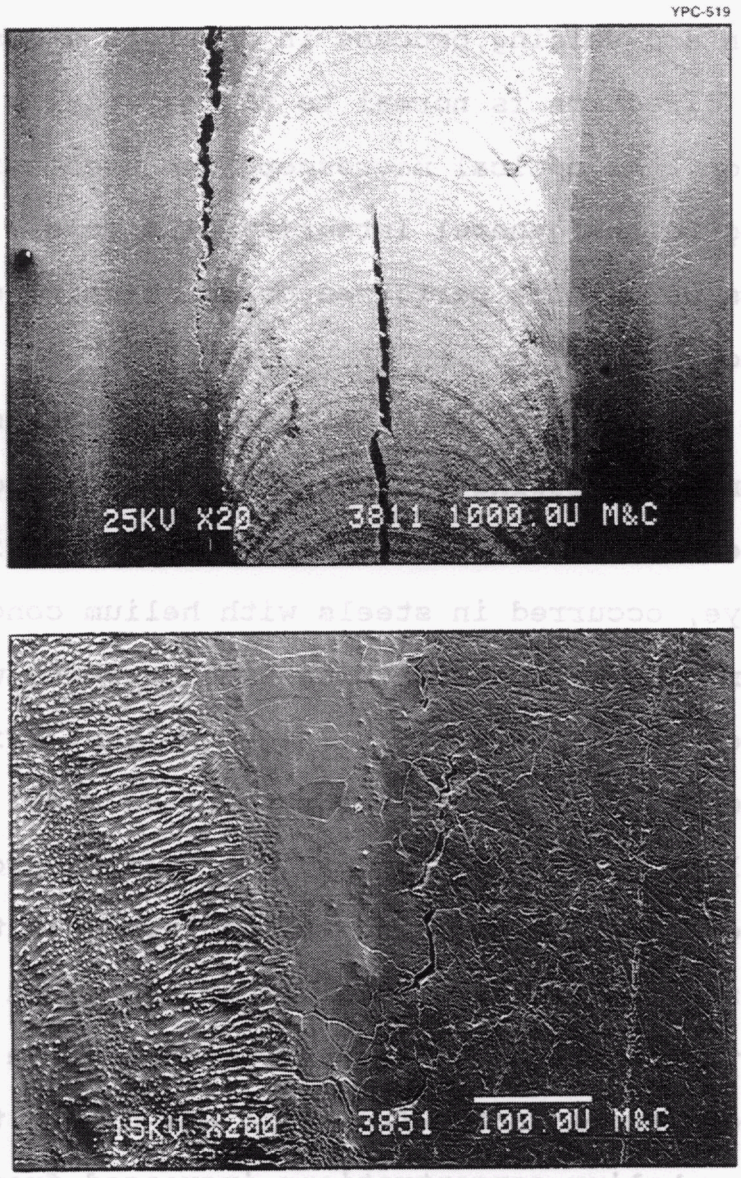

Figure 28. Weld cracking of type 316 stainless steel containing 5.2 appm helium using standard GTA welding process.

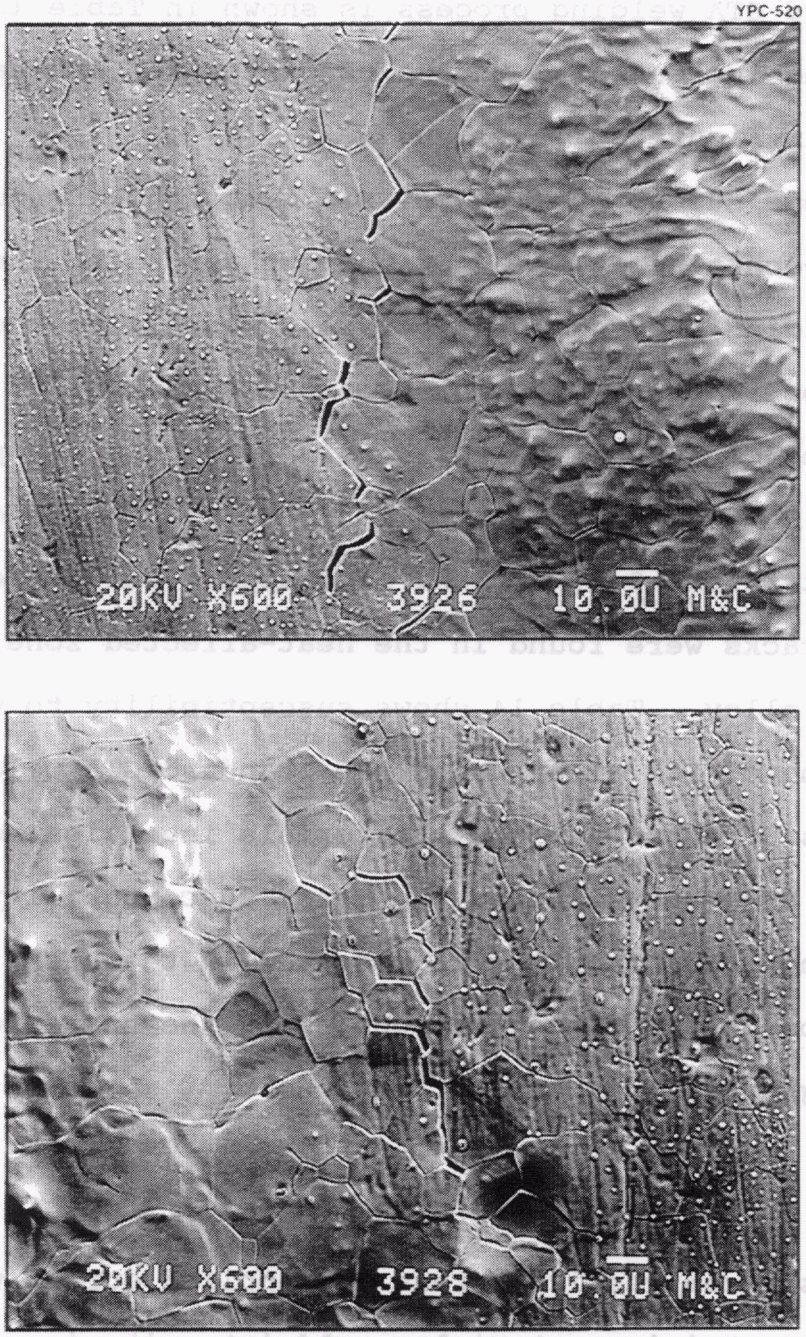

Figure 29. Microcracks in the heat-affected zone of type 316 stainless steel, 9.7 appm He. Cracking occurs perpendicular to stresses developed during cooling.

average weld cracking in type 316 stainless steel using the standard GTA welding process is shown in Table 13. Weld cracking increased as the He concentration increased as shown in Figure 30.

Less susceptibility to weld cracking was found in helium-containing PCA alloy when welded using the standard GTA welding process. Macrocracks, visible to the naked eye, were observed only at the fusion zone with up to a maximum cracking of 17% of the total weld length in one particular weld. However, cracks were found at all levels of helium concentration: 3.9, 6.0 and 11.4 appm. Only a few microcracks were found in the heat-affected zone regions for PCA-B3 alloy. Table 14 shows susceptibility to weld cracking of PCA alloy using the standard GTA welding process. Among all three materials investigated in this study, HT-9 steel showed the least susceptibility to weld cracking. No cracking was observed in the steel with up to 2.5 appm helium concentrations using the standard GTA welding process.

Stress Effects

As a compressive stress was applied during welding of helium containing materials, weld integrity improved significantly. Compressive stresses were applied via a hydraulic jack mounted on the welding table. The applied stress levels were measured using a series of 5 strain gages

Table 13

Susceptibility to weld cracking of type 316 stainless steel, standard GTA welding process

He (appm)	HAZ Cracking (%)	F.Z. Cracking (%)	Total (%)	Specimens Tested
0.7	0	0	0	5
1.5	5	0	5	5
5.2	23	8	31	5
9.7	66	6	72	5

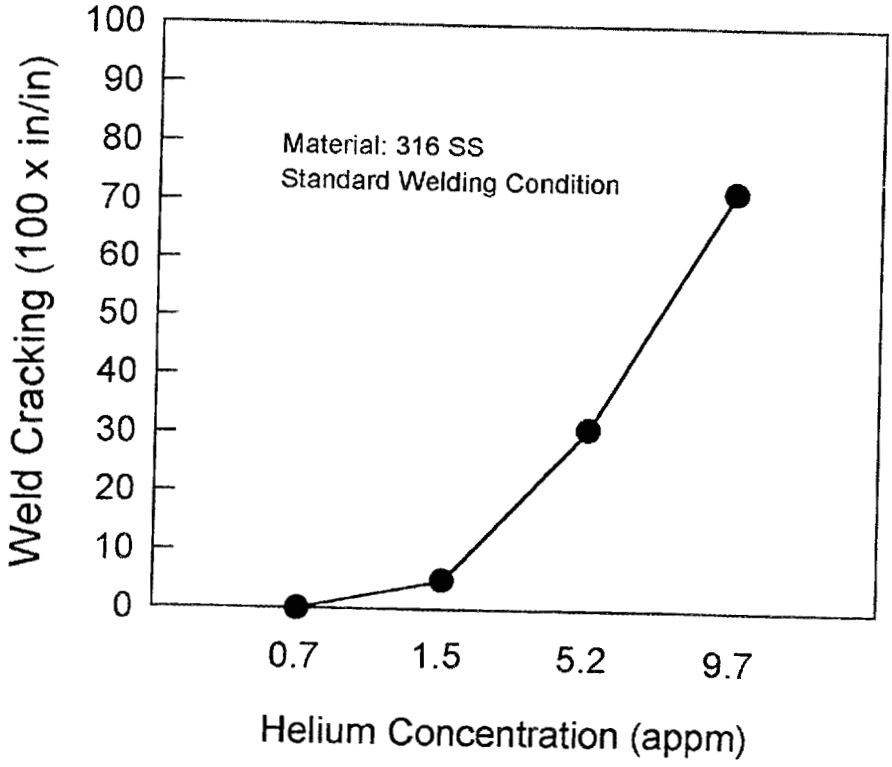

Figure 30. Weld cracking increases as the He concentration increases.

Table 14

Susceptibility to weld cracking of PCA alloy, standard GTA welding process

He (appm)	HAZ Cracking (%)	F.Z. Cracking (%)	Total (%)	Specimens Tested
3.9	few	3	3	3
6.0	few	3	3	3
11.4	few	9	9	3

attached to a type 316 stainless steel plate. Gage No.3 was located at the center of the welding line and gages No. 1 and 2 were located at the beginning end of the plate while gages No. 4 and 5 were at the other end. Figure 31 shows the schematic for the hydraulic jack pressure calibration. The applied stress levels generated by the hydraulic jack were calculated from the readings of the strain gages. Figure 32 shows the results of the hydraulic jack pressure calibration. Note that gage No.5 was damaged during setup so data from it were not included. Generally, a linear relation was observed between the pressure readings obtained from hydraulic jack and measured strains, until the calibration plate started to buckle at about 180 MPa.

As the applied compressive stress was increased in the modified welding process, heat-affected zone cracking decreased. The stress level required to eliminate weld cracking increased with increasing helium concentrations. Heat-affected zone cracking totally vanished at a compressive stress level of 165 MPa for type 316 stainless steel in this study as shown in Table 15. A compressive stress of 55 MPa was found to be sufficient to suppress the severe through thickness cracking found in the fusion zone.

In the case of PCA alloy, cracking was totally eliminated by the application of a 55 MPa compressive stress during welding as shown in Table 16.

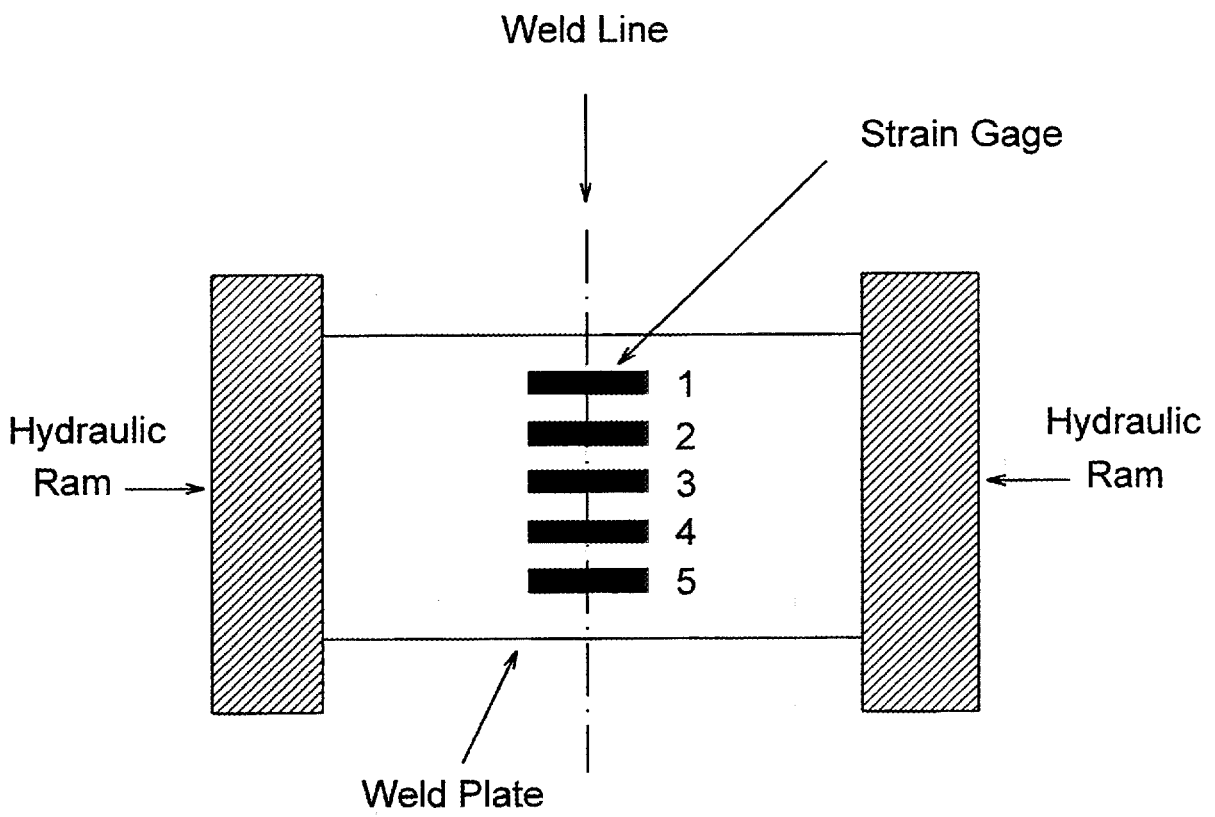

Figure 31. Hydraulic jack pressure calibration.

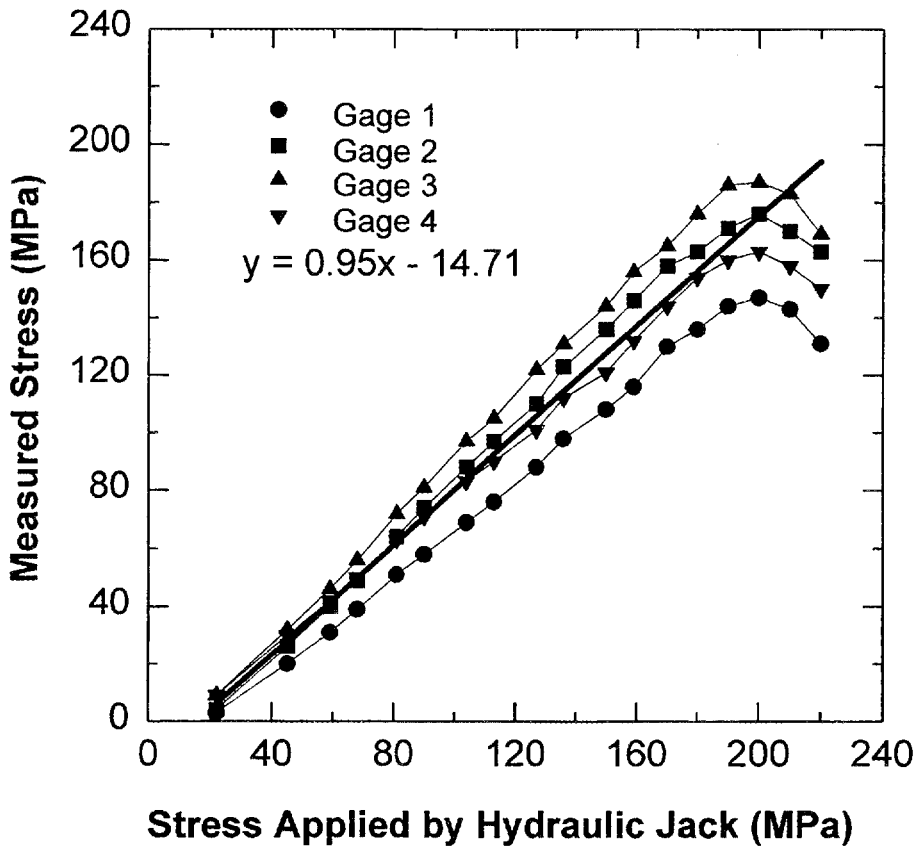

Figure 32. Results of the hydraulic jack pressure calibration.

Table 15

Weld cracking in type 316 stainless steel

Type 316 Stainless Steel Weld Cracking (%)				
Applied Stress (MPa)	Helium Concentration (appm)			
	0.7	1.5	5.2	9.7
0	0	5	31	72
55	0	3	10	22
110	0	0	2	7
165	0	0	0	0

Table 16

Weld cracking in PCA-B3 alloy

PCA-B3 Steel Weld Cracking (%)			
Applied Stress (MPa)	Helium Concentration (appm)		
	3.9	6.0	11.4
0	3	3	9
55	0	0	0
110	0	0	0
165	0	0	0

Microhardness Tests

As a means to ascertain microstructure-properties relationships, traverse diamond pyramid microhardness (DPH) measurements were conducted across the weld regions using a Micromet 3 microhardness tester (by Buehler Ltd., Lake Bluff, IL). Figures 33-35 show the results of microhardness tests for various materials.

Microhardness across the weld region of type 316 stainless steel is shown in Figure 33. No strengthening was observed in type 316 stainless steel containing helium up to 9.7 appm. Due to the presence of ferrite after welding, a minor decrease in microhardness was observed in the fusion zone, which also showed a larger variation in individual measurements. The increase of microhardness in the heat-affected zone area was attributed to the increase in dislocation density from rapid cooling.

Figure 34 shows the microhardness across the weld region of PCA alloy. Similarly, microhardness was also insensitive to the presence of helium up to 11.4 appm. The decrease in hardness in the heat-affected and the fusion zones was attributed to the recovery of dislocations from cold-work. Microhardness across the weld region of HT-9 steel is shown in Figure 35. Significant increases in microhardness were observed in the fusion and heat-affected zones for HT-9 steel. The microstructure in these regions is untempered martensite. The minor variation of

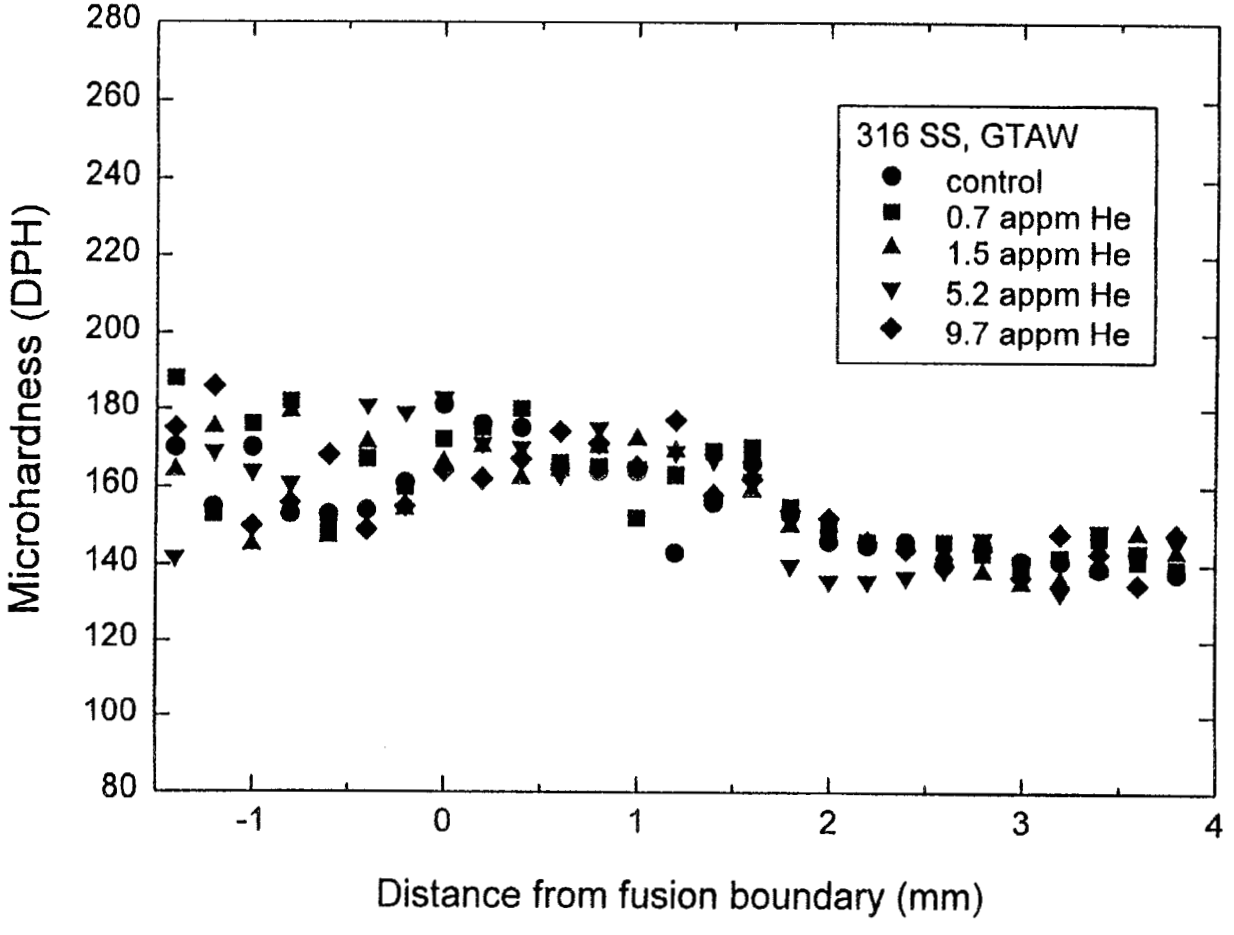

Figure 33. Microhardness across welds of type 316 stainless steel.

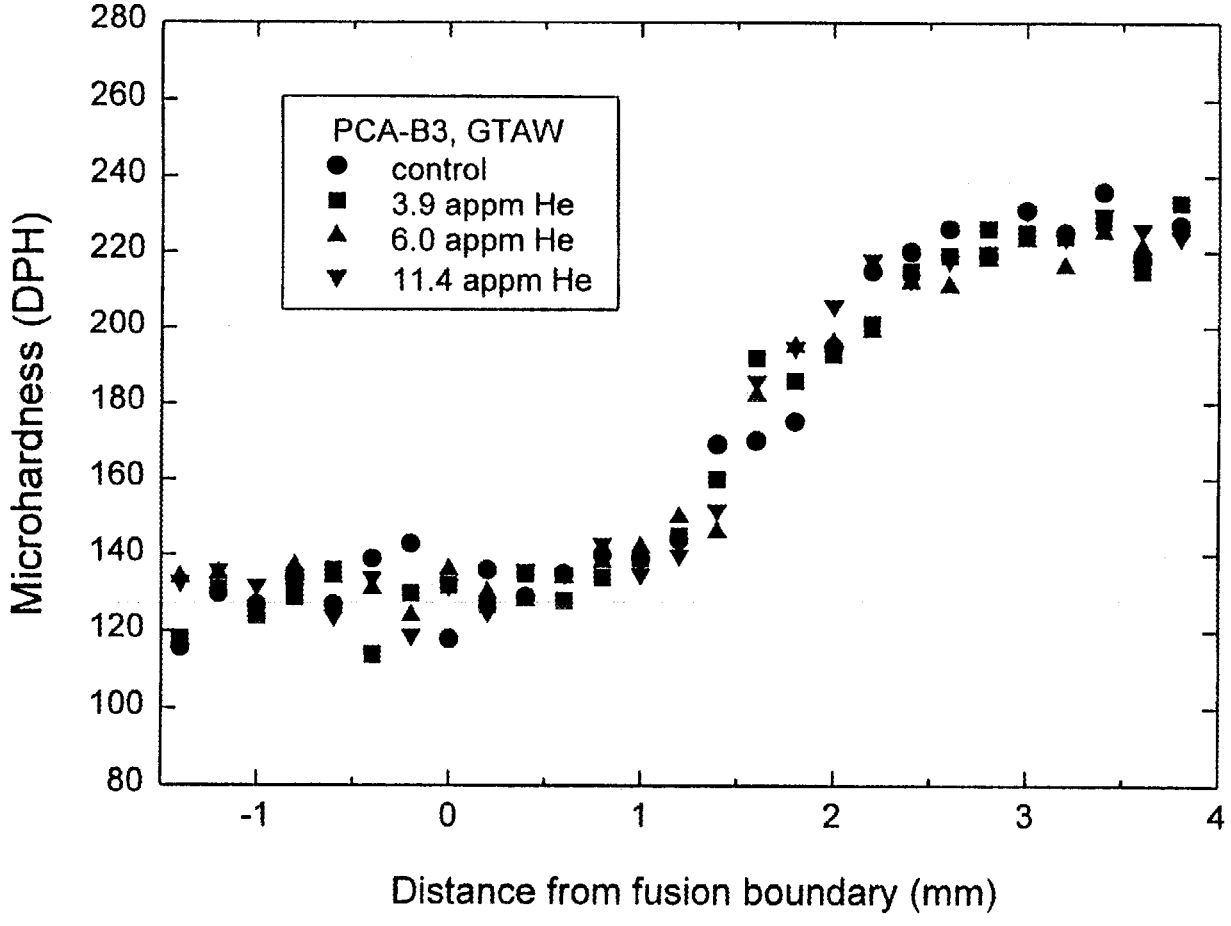

Figure 34. Microhardness across welds of PCA-B3 alloy.

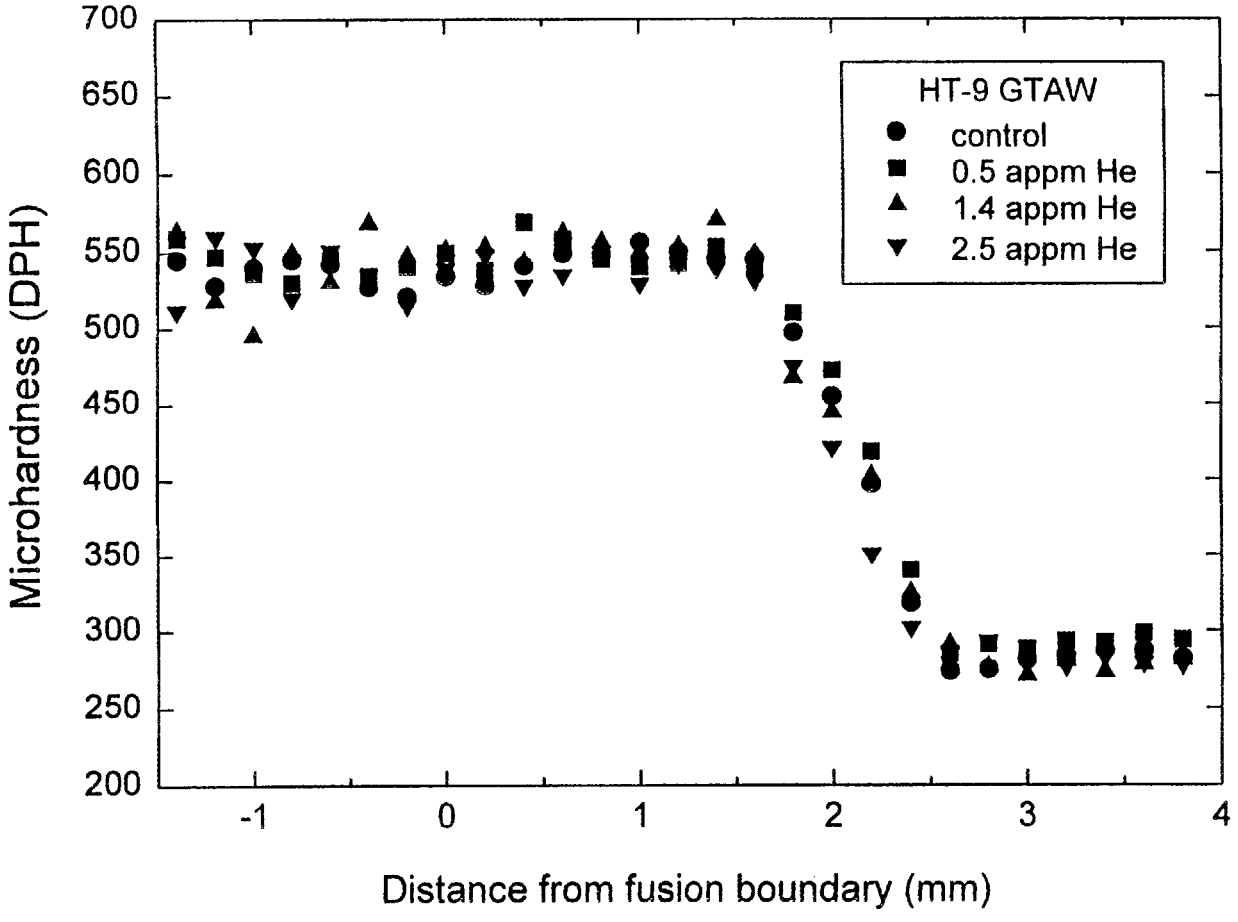

Figure 35. Microhardness across welds of HT-9 steel.

microhardness in the fusion zone was also attributed to the presence of a softer ferrite phase.

Tensile Tests

Tensile tests were conducted at room temperature with a strain rate of 5×10^{-4} s^{-1}. All specimens were tested with the stress axis parallel to the rolling direction. No apparent change in strength and ductility was observed for type 316 stainless steel containing up to 9.7 appm helium in the as-charged condition. Figure 36 shows the results of room temperature tensile tests for type 316 stainless steel in the as-charged condition. Although the application of a compressive stress during welding effectively suppressed the HAZ cracking, the weld ductility still decreased due to grain boundary bubble growth as shown in Figure 37. However, the strength of the 165 MPa compressed welds remains about the same as in the as-charged condition for type 316 stainless steel containing 9.7 appm helium. Results of room temperature tensile properties of type 316 stainless steel are shown in Tables 17 and 18.

Most of the tensile specimens failed in the base metal region, while a few specimens failed in the heat-affected zone due to severe helium bubble growth near the fusion boundary. For those specimens which failed in the HAZ, the total elongation decreased to as low as 6% while for others it was 38% on average. It should be noted that the sampling

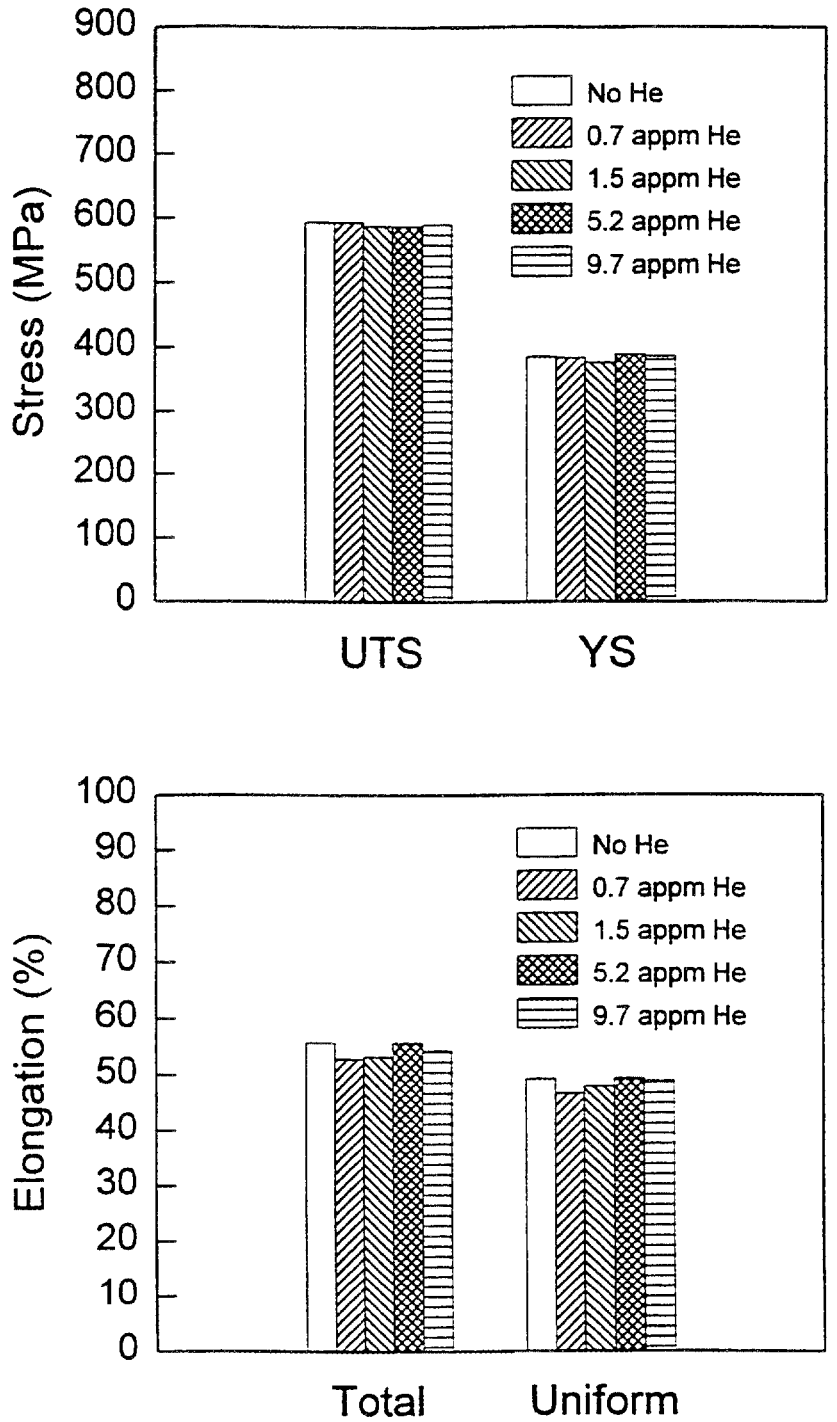

Figure 36. Results of room temperature tensile tests of type 316 stainless steel in the as-charged condition.

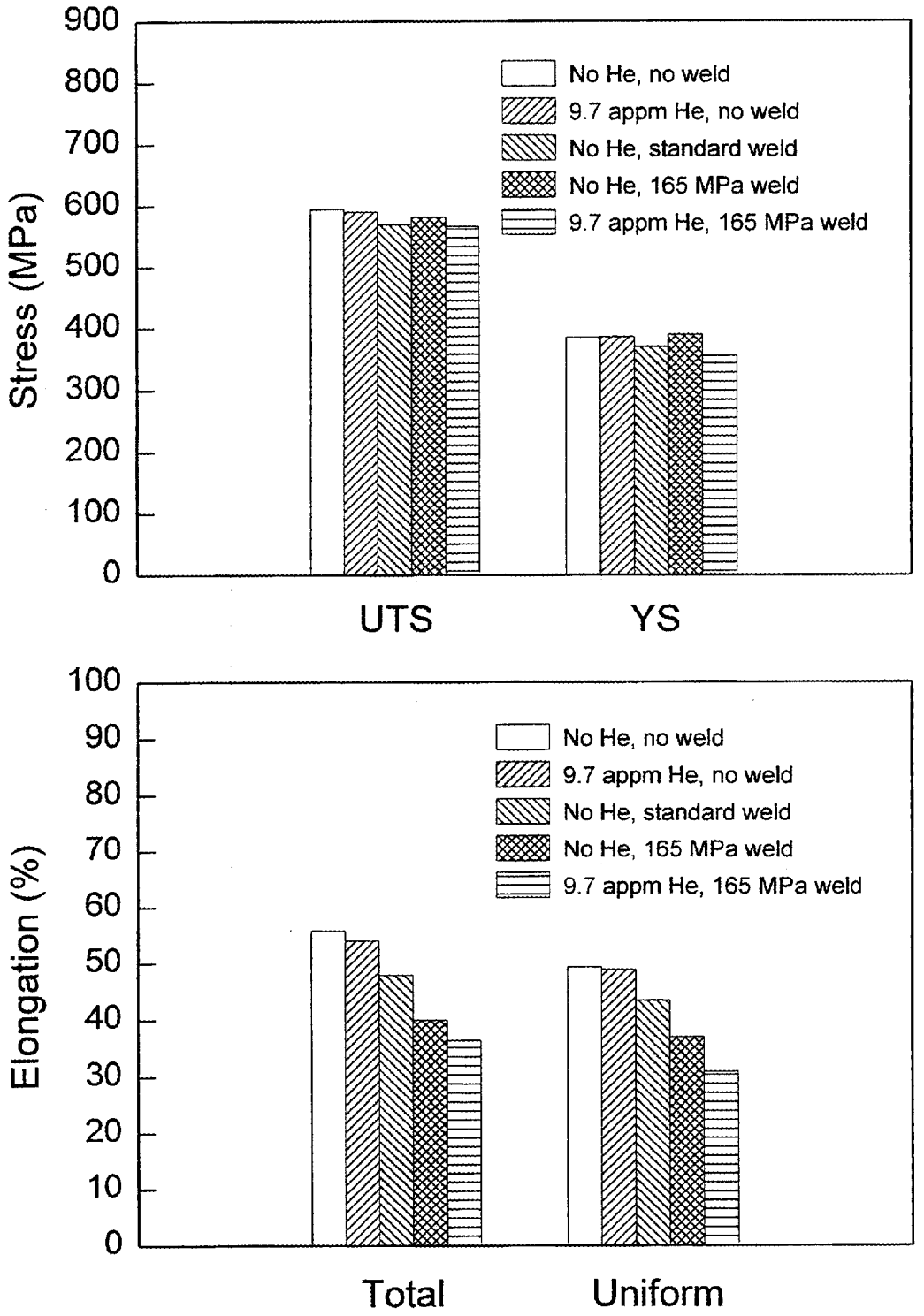

Figure 37. Tensile properties of He-doped type 316 stainless steel following welding.

Table 17

Room temperature tensile properties of stress modified welds and unwelded base material of type 316 stainless steel containing 0.7 and 1.5 appm helium

	0.7 appm He		1.5 appm He			
				Applied Stress (MPa)		
	Base	Weld	Base	0	55	110
YS(MPa)	383	357	376	350	355	350
UTS(MPa)	594	574	588	565	570	570
UE(%)	46.7	37.3	48.0	27.8	37.7	40.1
TE(%)	52.9	42.6	53.3	42.8	44.4	47.5

Table 18

Room temperature tensile properties of stress modified welds and unwelded base material of type 316 stainless steel containing 5.2 and 9.7 appm helium

	5.2 appm He					9.7 appm He				
		Applied Stress (MPa)					Applied Stress (MPa)			
	Base	0	55	110	165	Base	0	55	110	165
YS(MPa)	389	375	364	366	376	386	367	378	372	355
UTS(MPa)	587	583	576	575	584	590	579	577	590	567
UE(%)	49.4	42.0	33.0	38.1	31.8	48.9	36.1	34.9	32.8	31.0
TE(%)	55.8	46.6	38.0	44.0	37.6	54.4	43.5	40.6	38.5	36.4

of specimens played a key role in the results of tensile tests. Specimens were punched from sections of the weld where no visible cracks were observed. Although care was taken to prevent the inclusion of cracks in tensile specimens, the extent of microcracking beneath the surface and helium bubble growth at the HAZ were unknown, and; therefore, large variations in tensile results were possible.

Results of tensile tests for PCA and HT-9 are listed in Table 19 and 20. Helium presence caused no clear change in the mechanical properties in PCA-B3 and HT-9 similar to that in type 316 stainless steel. PCA-B3 tensile tests showed inconsistencies in fracture location. Failures of PCA-B3 were found in the base metal, HAZ and fusion zone although it retained about the same strength. All the HT-9 failed in the base metal region and also retained its strength up to 2.5 appm He concentration.

Scanning Electron Microscopy

Scanning electron microscopy was used to examine the detailed features of weld cracking and fracture surfaces. Heat-affected zone cracking of type 316 stainless steel containing 1.5 appm helium is shown in Figure 38. No fusion zone cracking was observed in type 316 stainless steel with 1.5 appm helium. Heat-affected zone cracking was fully intergranular in nature. The fracture surfaces showed a

Table 19

Room temperature tensile properties of stress modified welds and unwelded base material of PCA-B3 alloy

	He Concentration (appm)					
	3.9 appm		6.0 appm		11.4 appm	
	Base	Weld	Base	Weld	Base	Weld
YS(MPa)	435	413	429	403	419	440
UTS(MPa)	564	553	554	531	550	557
UE(%)	18.6	17.4	17.1	16.7	17.9	15.1
TE(%)	32.5	25.7	25.5	23.0	29.2	21.5

Table 20

Room temperature tensile properties of stress modified welds and unwelded base material of HT-9 steel

	He Concentration (appm)					
	0.5 appm		1.4 appm		2.5 appm	
	Base	Weld	Base	Weld	Base	Weld
YS(MPa)	881	843	876	833	899	785
UTS(MPa)	1023	950	1014	933	1010	905
UE(%)	7.8	6.9	8.0	6.8	8.1	7.1
TE(%)	11.3	10.8	11.6	10.4	10.5	11.2

YPC-518

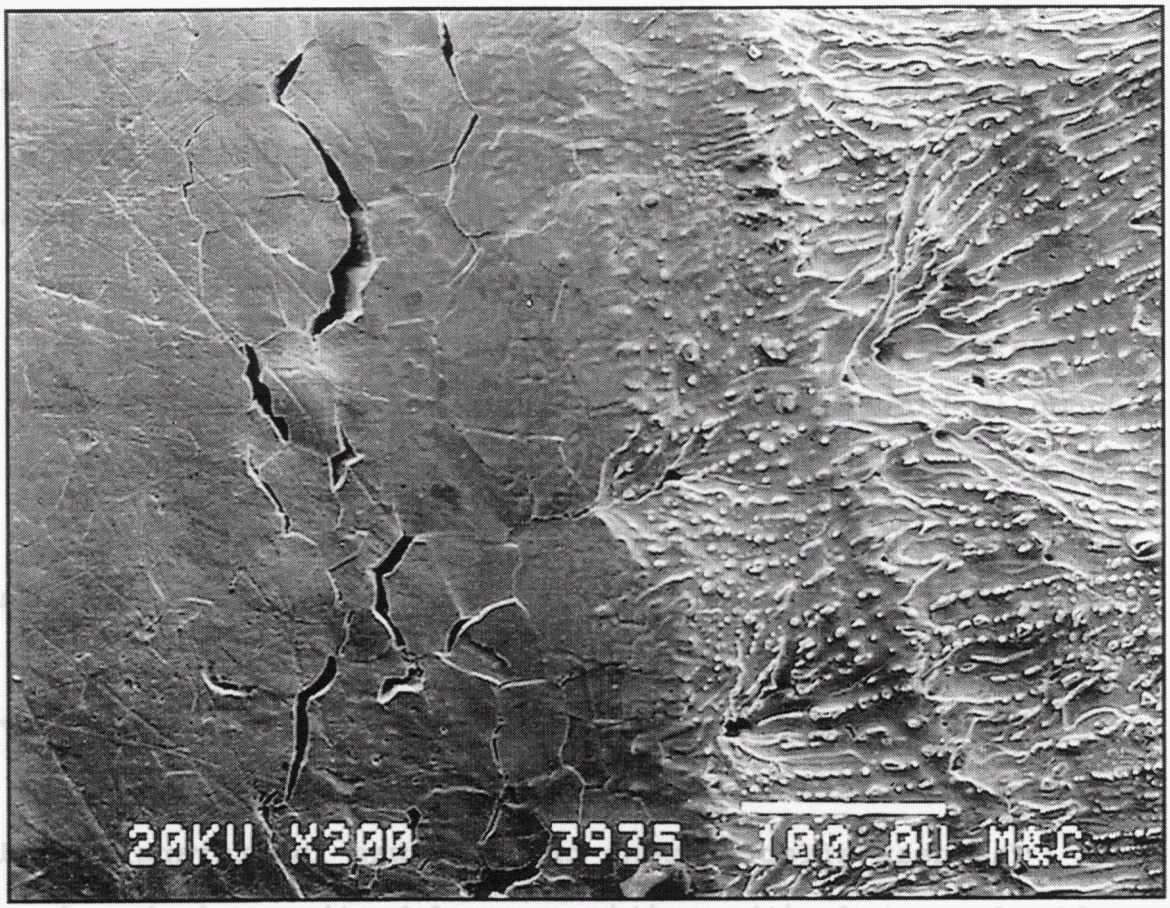

Figure 38. Heat-affected zone cracking of type 316 stainless steel containing 1.5 appm helium.

dimple structure, a sign of grain boundary cavity growth. Figure 39 shows the cavity size distribution and cavity volume average diameter ($VAD=(\Sigma N_i D_i^3/\Sigma N_i)^{1/3}$) of HAZ fracture surfaces in type 316 stainless steel.

Figure 40 shows the changes in weld integrity as a result of the applied compressive stress during welding in type 316 stainless steel with 5.2 appm He concentration. Continuous through-thickness fusion zone and HAZ cracking were observed in standard welds of type 316 stainless steel as shown in Figures 40a. Both cracks ran parallel to the welding direction. Microcracks were also observed at HAZs in standard welds as shown in Figure 40b. Results from stress-modified GTA welds revealed no visible cracks as shown in Figures 4c and 4d. Compressive stresses from 55 to 165 MPa were applied in these experiments. The result is consistent with the welding of type 316 stainless steel, containing 256 appm helium, under compressive stress in the earlier study [110].

Examinations revealed that fusion zone cracking in type 316 stainless steel was interdendritic as shown in Figure 41. The heat-affected zone cracking was intergranular and fully decorated with cavities caused by the grain boundary helium bubble growth, as shown in Figure 42. The cavity volume-averaged diameters (VAD) in HAZ fracture surfaces were calculated to be 0.96 and 0.92 μm for steels containing 5.2 and 9.7 appm He respectively. The results were

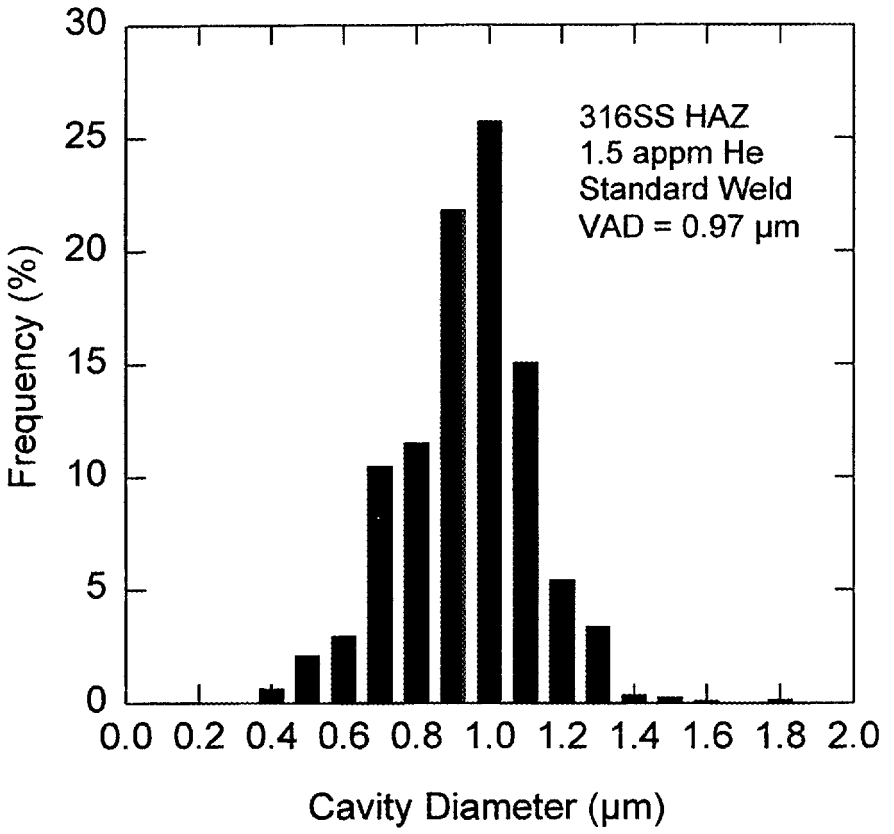

Figure 39. Cavity size distribution and cavity volume average diameter ($VAD=(\Sigma N_i D_i^3/\Sigma N_i)^{1/3}$) of HAZ fracture surfaces in type 316 stainless steel.

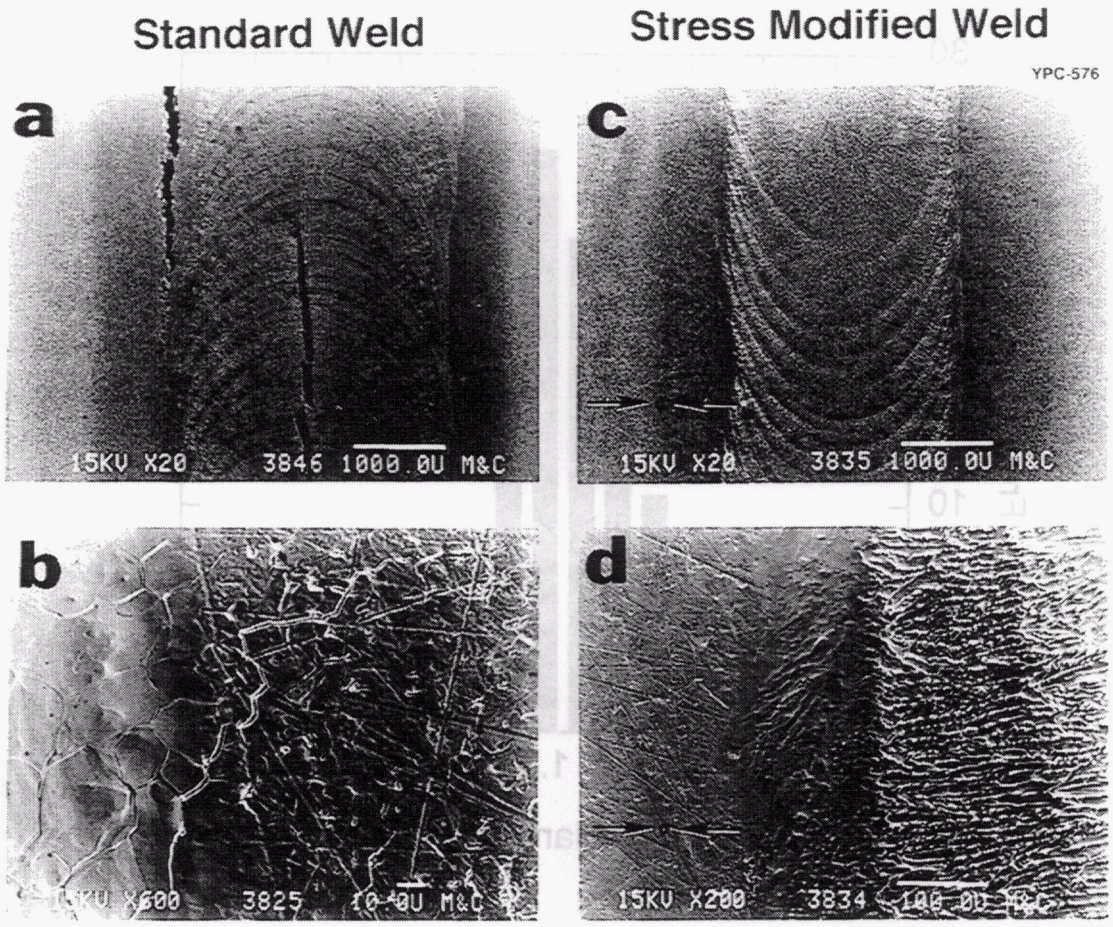

Figure 40. Comparison of heat-affected zone in standard and stress-modified welds of type 316 stainless steel containing 5.2 appm helium: (a,b) continuous through thickness fusion zone and heat-affected zone cracking in a standard weld; (c,d) no visible cracking in stress-modified weld.

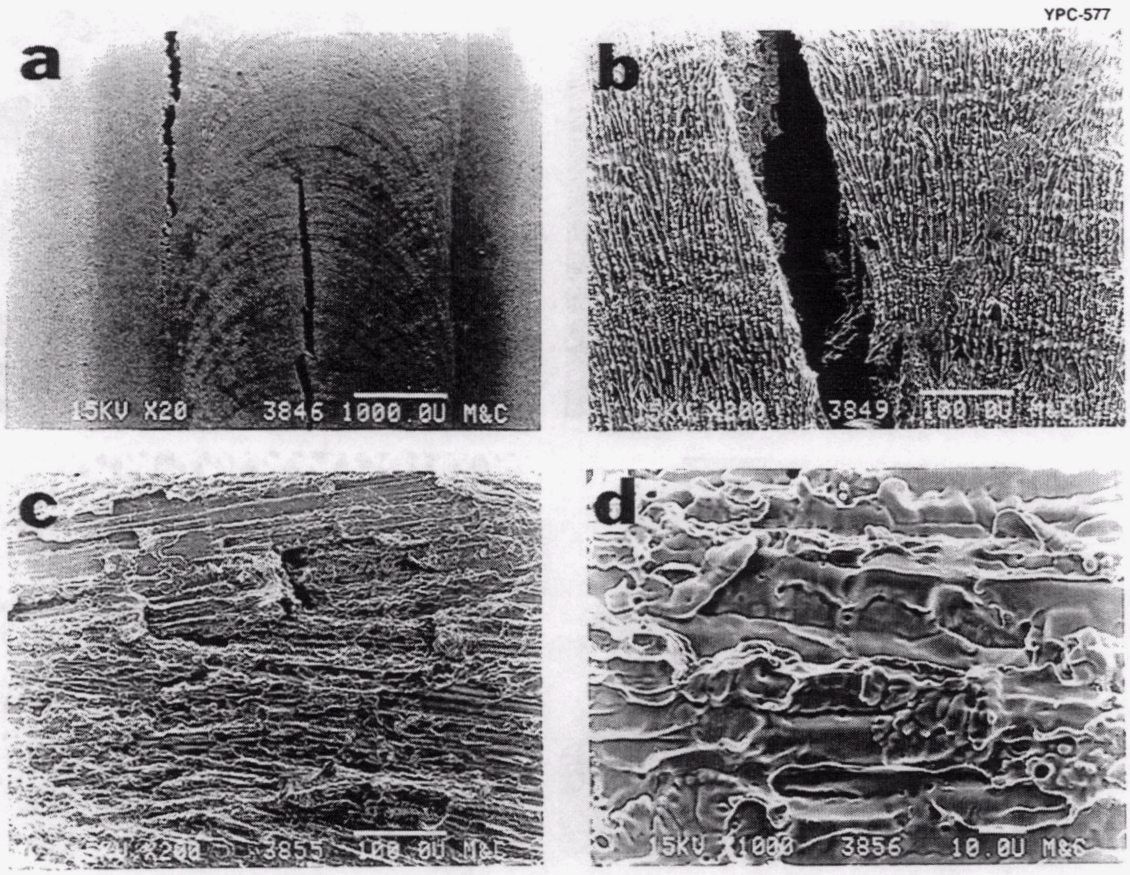

Figure 41. Interdendritic fusion zone cracking was observed in type 316 stainless steel containing as low as 5.2 appm He; b, c and d show increasing magnification of the fusion zone cracking.

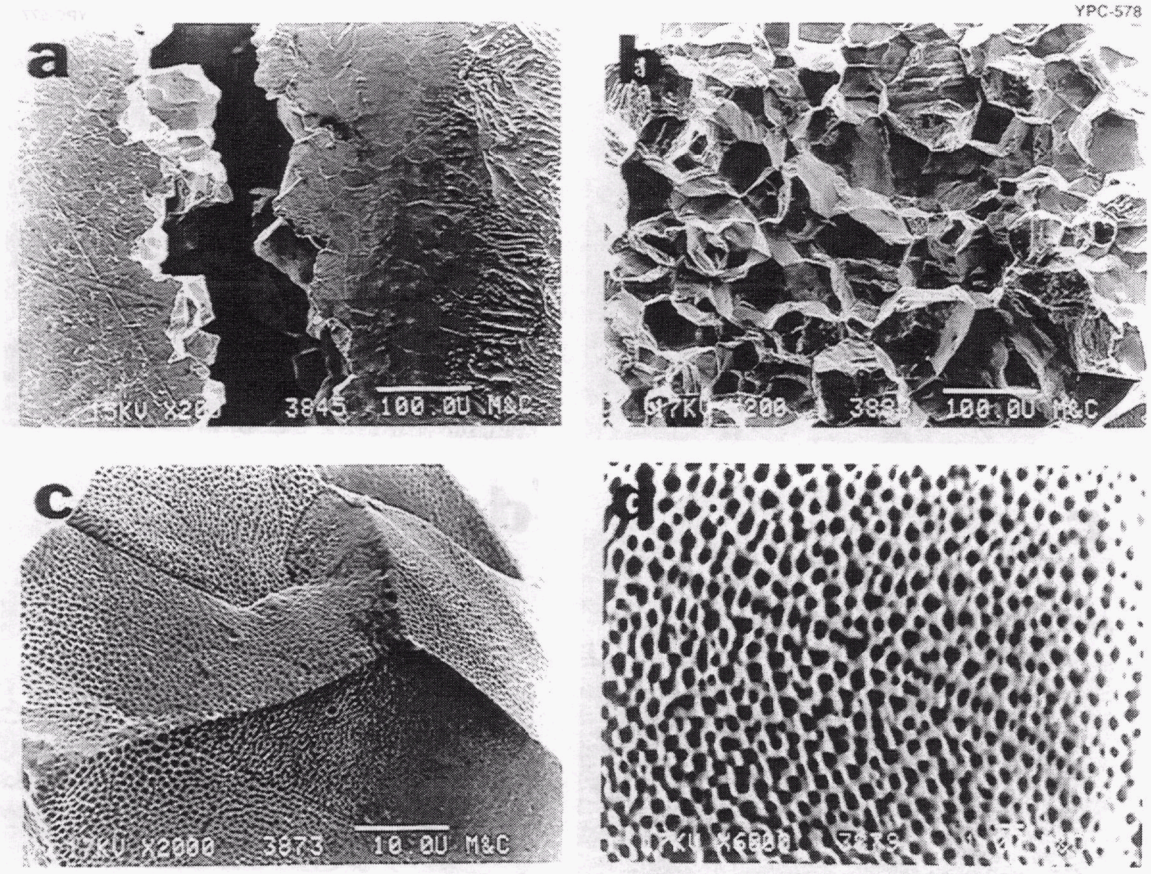

Figure 42. Intergranular HAZ cracking was fully decorated with cavities caused by grain boundary helium bubble growth in type 316 stainless steel containing 5.2 appm He; b, c and d show increasing magnification of the HAZ fracture surfaces.

consistent with previous studies [16]. The HAZ fracture surface cavity size distributions for type 316 stainless steel containing 5.2 and 9.7 appm He are shown in Figure 43.

Further examinations of TEM disks, prepared from the fusion zone/heat-affected-zone boundary, were conducted using SEM following jet thinning. In the standard GTA weld, as shown in Figure 44a, large perforations and cracking were observed with cracks tending to align parallel to the welding direction, indicated by the arrow. On the other hand, parallel cracking associated with grain boundary helium bubble growth had been suppressed by the application of a compressive stress in the stress-modified weld as shown in Figure 44b. In addition, the bubble growth had been altered such that bubbles grow predominantly along grain boundaries perpendicular to the weld direction, whereas previously they occurred principally on grain boundaries parallel to the weld. It should be pointed out that jet polishing during TEM specimen preparation attacked the grain boundaries and enlarged grain boundary cavities. Therefore, the grain boundary bubble sizes shown in Figure 44 were exaggerated as compared to the as-welded material.

Steady state welding on type 316 stainless steel was also investigated in this study. Heat-affected zone cracking was found around the weld pool as shown in Figure 45. The fracture facets revealed dimple structure as found in the previous section.

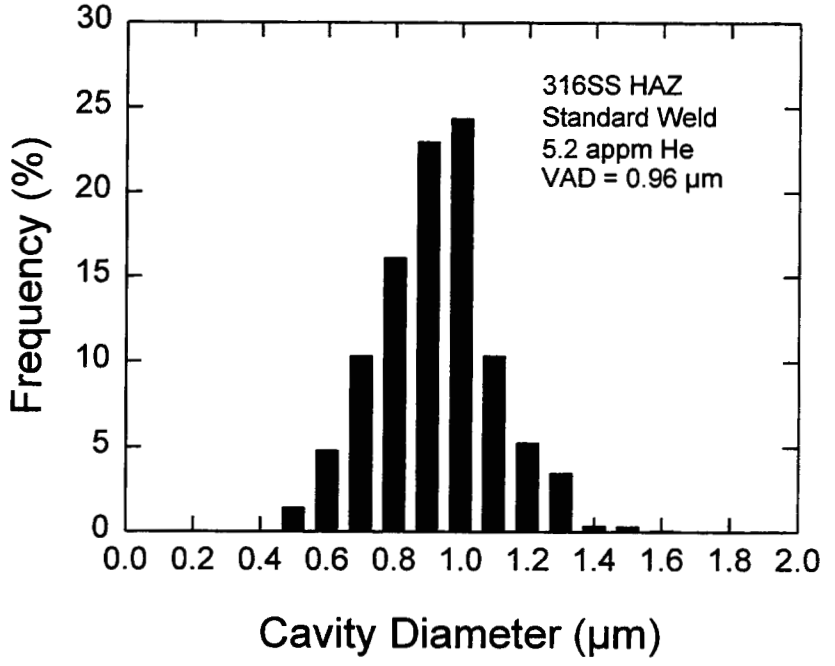

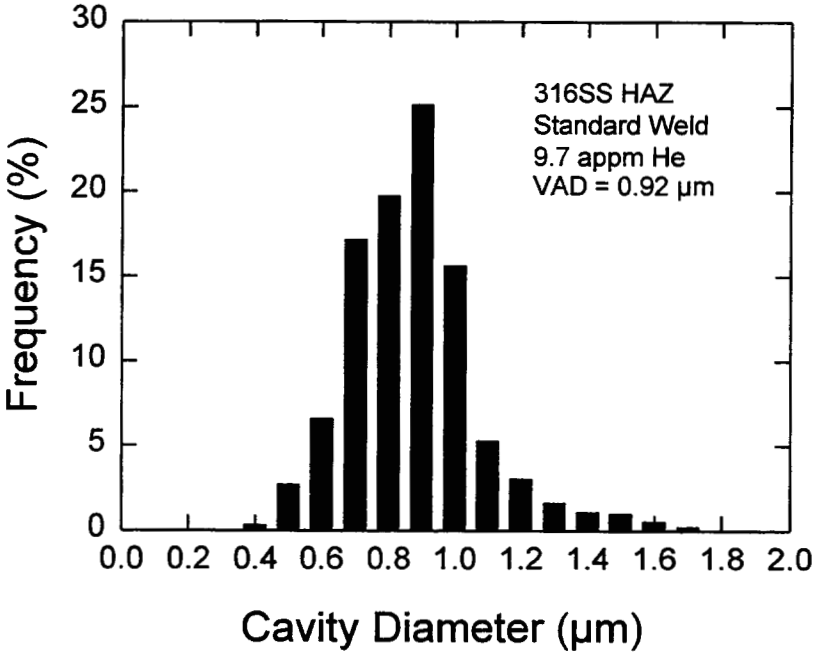

Figure 43. HAZ fracture surface cavity size distribution for type 316 stainless steel containing 5.2 and 9.7 appm He.

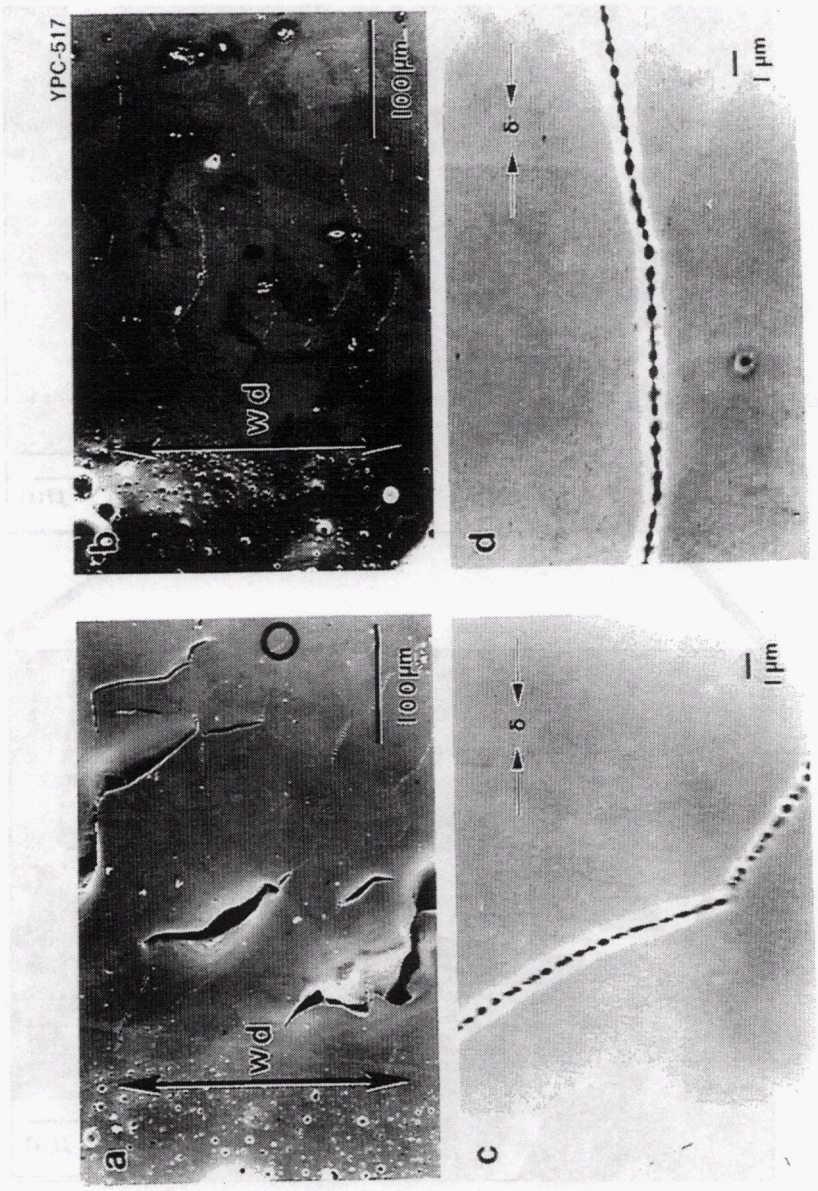

Figure 44. SEM photographs of jet-polished TEM discs from (a) standard GTA weld; (b) stress-modified GTA weld. Arrows indicate the welding direction (wd). (C) and (d) are magnified features of circle in (a) and (b) respectively.

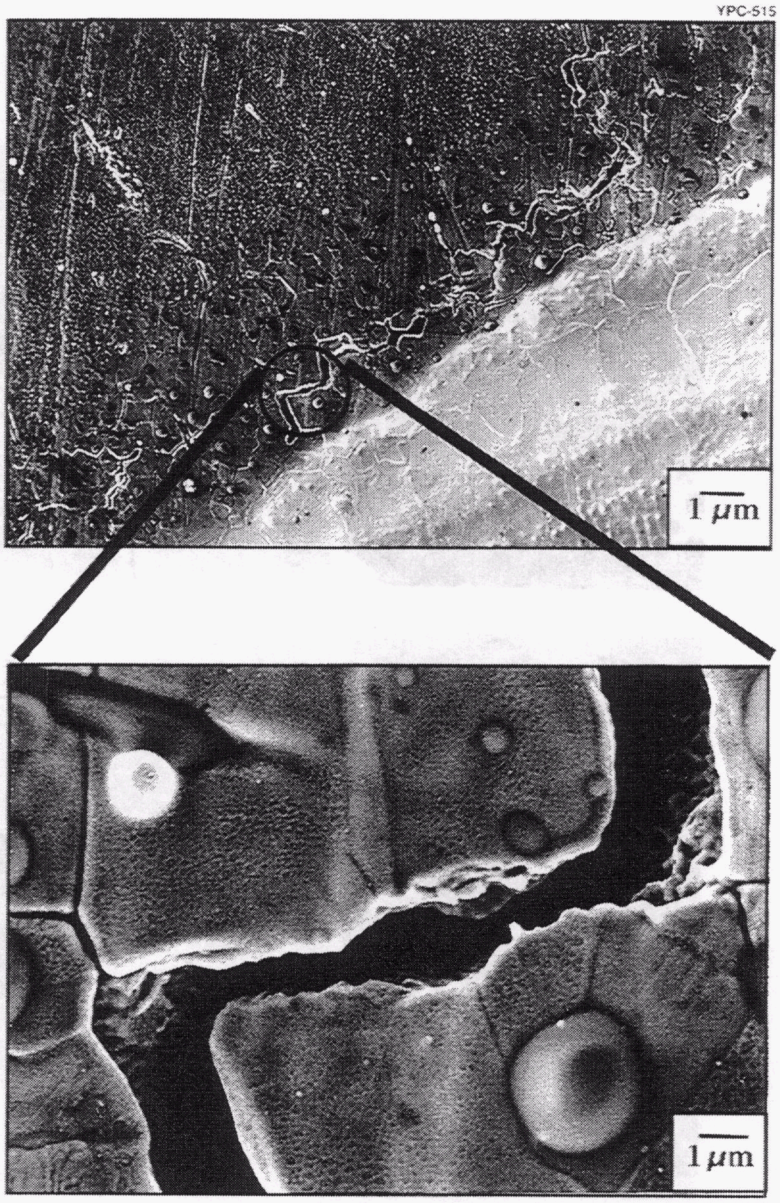

Figure 45. Heat-affected zone cracking was found around the weld pool of a steady state weld of type 316 stainless steel containing 1.5 appm He.

Measurements from gas mass spectrometry showed a 21% decrease of helium concentration in the fusion zone compared to as-charged material. Figure 46 shows the porosity morphology in the fusion zone of type 316 stainless steel after GTA welding. Porosity in the fusion zone is a result of helium gas bubbles which do not escape from the molten pool during welding. The decrease in helium concentration in the fusion zone indicated that a substantial volume of helium escaped form the molten pool during welding. No distinct difference of pore size in the fusion zone was observed with helium concentrations up to 9.7 appm.

Transmission Electron Microscopy

A transmission electron microscope, JAM 2000FX by JOEL Ltd., was used as a primary tool for the helium bubble observations. TEM foils were prepared from 3 mm diameter disks punched from the heat-affected zone. The disks were carefully positioned such that the final thinned hole would be located approximately 200 μm from the fusion boundary where the heat-affected zone cracking was most likely to occur. Magnifications of the microscope were calibrated using a standard replica grid. The results of TEM calibrations are shown in Figure 47.

A compressive stress of 55 MPa was found to inhibit helium bubble growth at heat-affected zone grain boundaries oriented parallel to the welding direction. In the matrix,

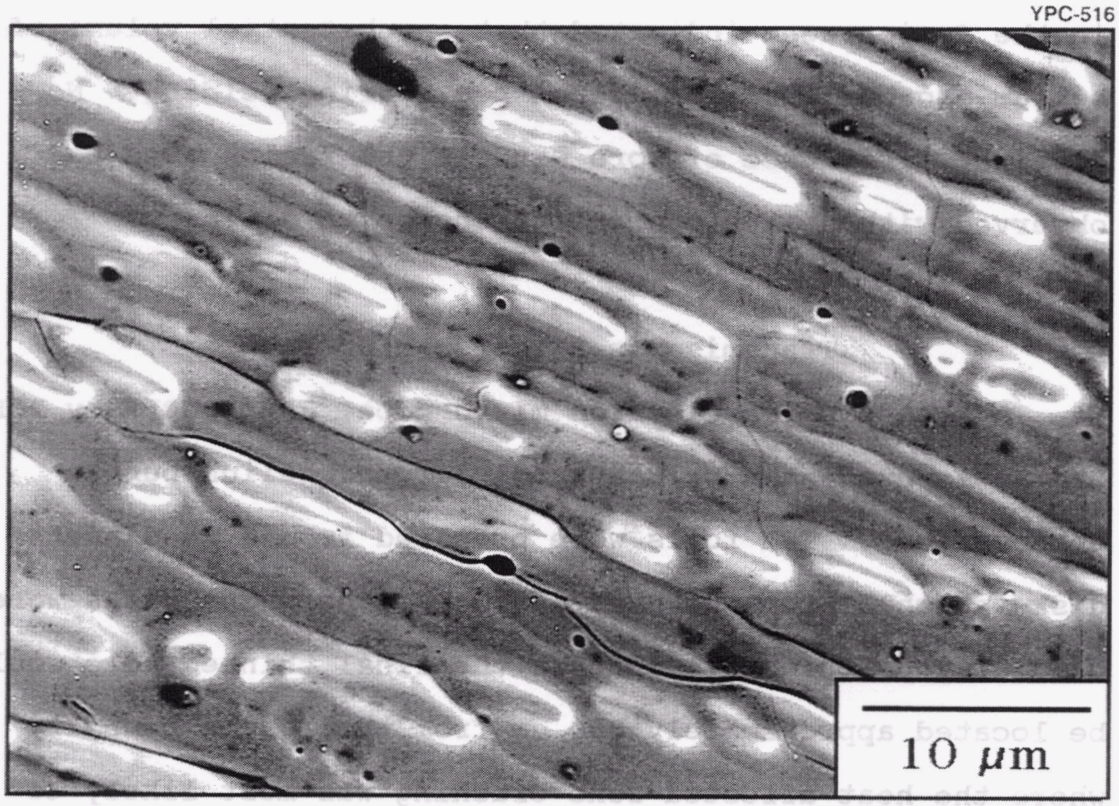

Figure 46. Fusion porosity morphology in type 316 stainless steel containing 9.7 appm He after GTA welding.

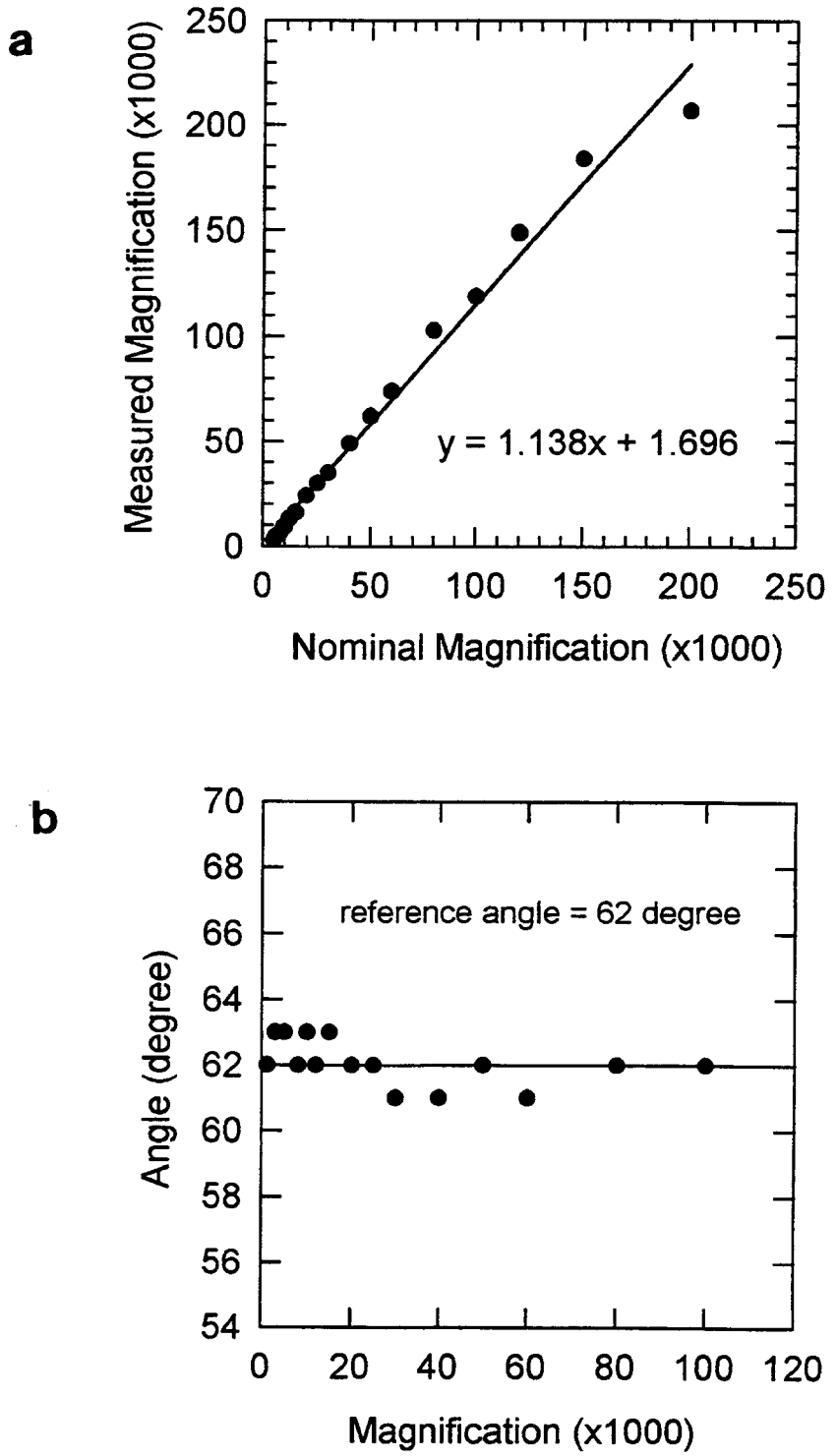

Figure 47. Results of TEM calibrations: (a) magnification and (b) image rotation.

the average helium bubble diameter was found to decrease with increases in applied compressive stress even though the number density remained constant. At the grain boundaries, however, the helium bubble number density increased with increasing compressive stress. It was also found that the helium bubbles located on grain boundaries parallel to the applied compressive stress are favored to grow due to bulk plate constraints with respect to those at grain boundaries parallel to the weld.

It is known that helium will nucleate and grow to form bubbles along defects, dislocations and grain boundaries at elevated temperature. Helium bubbles have been shown to grow and coalesce rapidly along grain boundaries subjected to a tensile stress [3,52]. This situation is found typically in autogenous welding upon cooling [5,6,27,33]. Internal tensile stresses are generated due to the volume contraction upon solidification and subsequent thermal contraction in the solid state. Catastrophic heat-affected zone (HAZ) intergranular cracking occurred following gas tungsten arc (GTA) welding, due to growth of helium bubbles along surfaces perpendicular to the internal stress.

In this study, solution-annealed type 316 stainless steel was doped with helium using tritium charging and decay. The tritium charging process was performed by Savannah River Laboratory, Aiken, SC. The charging conditions and results were tabulated in Tables 9 and 12.

TEM examinations revealed that Type 316 stainless steel remained in excellent annealed condition after tritium charging. Very few dislocations were found in as-charged steel containing as high as 9.7 appm helium.

During GTA welding, high temperature and shrinkage-induced tensile stress are the principal driving forces for helium bubble growth. Figure 48 shows the TEM micrograph of the HAZ helium bubble structure in a type 316 stainless steel containing 9.7 appm He in a standard GTA weld. The welding direction (wd) is indicated by an arrow. Large helium bubbles were found to be concentrated along grain boundaries as shown in Figure 49. The matrix, on the other hand, exhibited an extensive dislocation network which has been shown to be associated with helium bubbles. Large variations in helium bubble size and density were observed at adjacent grain boundaries. Few or no helium bubbles were found in some HAZ areas of a standard GTA weld as shown in Figure 50. One bubble was indicated by the arrowhead. In the base metal however, a limited dislocation structure was found as shown in Figure 51 and no helium bubbles were found in this region. Finally, in the fusion zone, helium bubbles were found to grow rapidly by coalescence at high temperature as shown in Figure 52. Helium bubbles grew as large as 1 μm in diameter.

The effect of an applied compressive stress during welding on the heat-affected zone helium bubble growth is

Figure 48. TEM micrograph of the HAZ helium bubble structure in type 316 stainless steel containing 9.7 appm He in a standard GTA weld. Welding direction (wd) is indicated by an arrow.

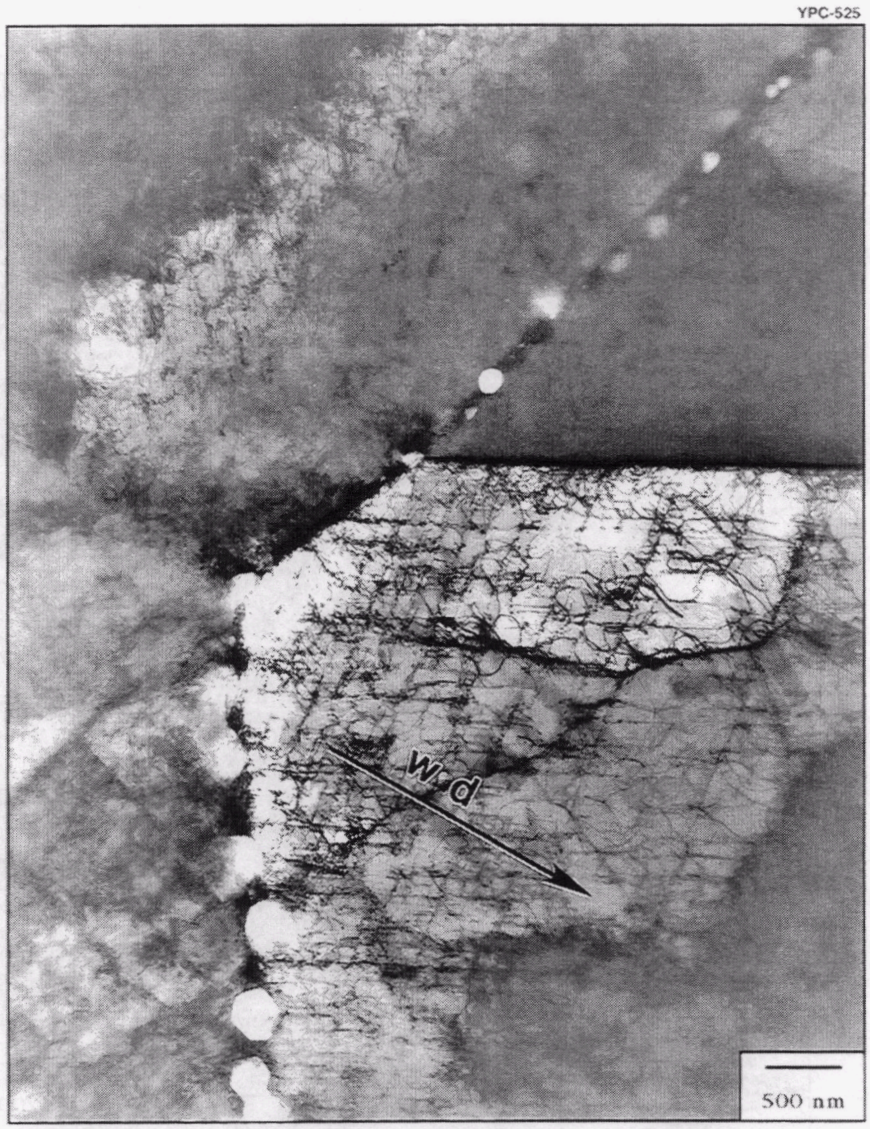

Figure 49. Extensive dislocation network was observed in the matrix of standard weld HAZ and helium bubbles were found to be concentrated at grain boundaries, 9.7 appm He concentration.

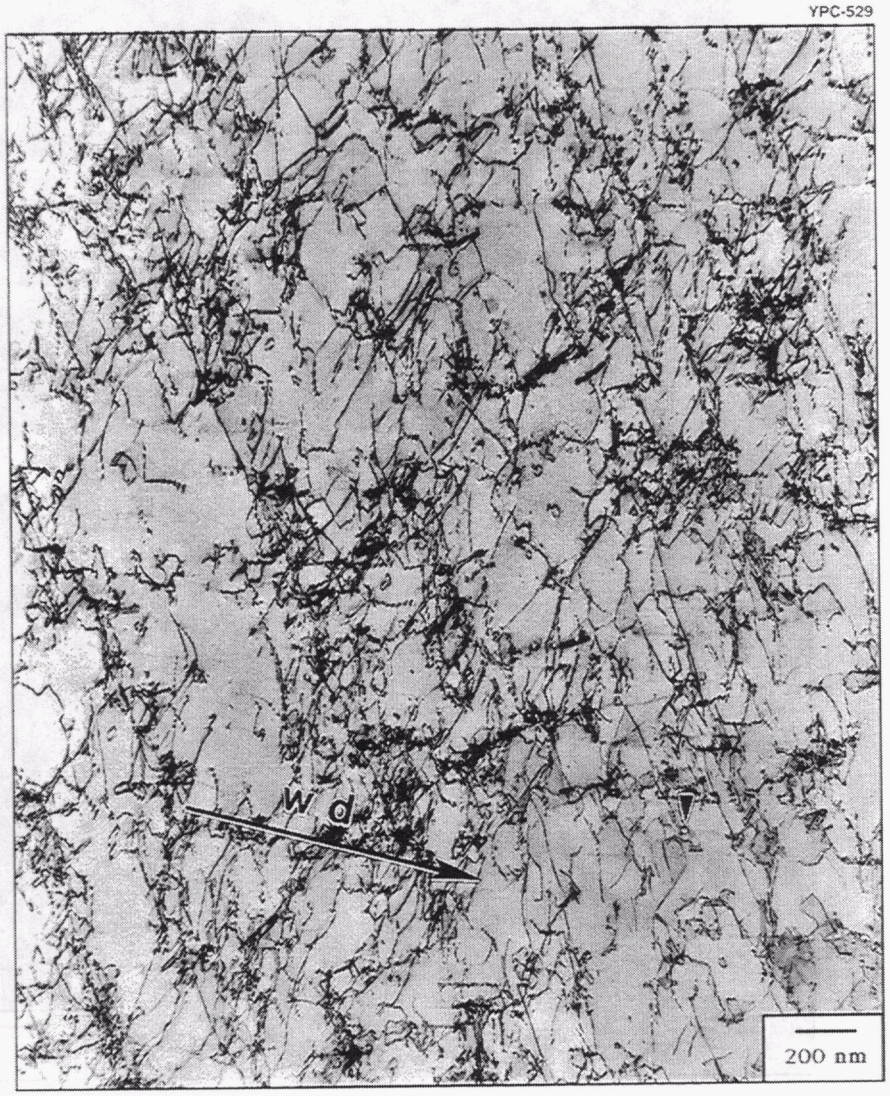

Figure 50. Very few or no helium bubbles were observed in some areas of the standard weld HAZ, 9.7 appm He concentration. One of the bubbles is indicated by the arrowhead.

Figure 51. TEM micrograph of base metal of a standard GTA weld of type 316 stainless steel containing 9.7 appm He. No helium bubbles were observed. Welding direction (wd) is indicated by an arrow.

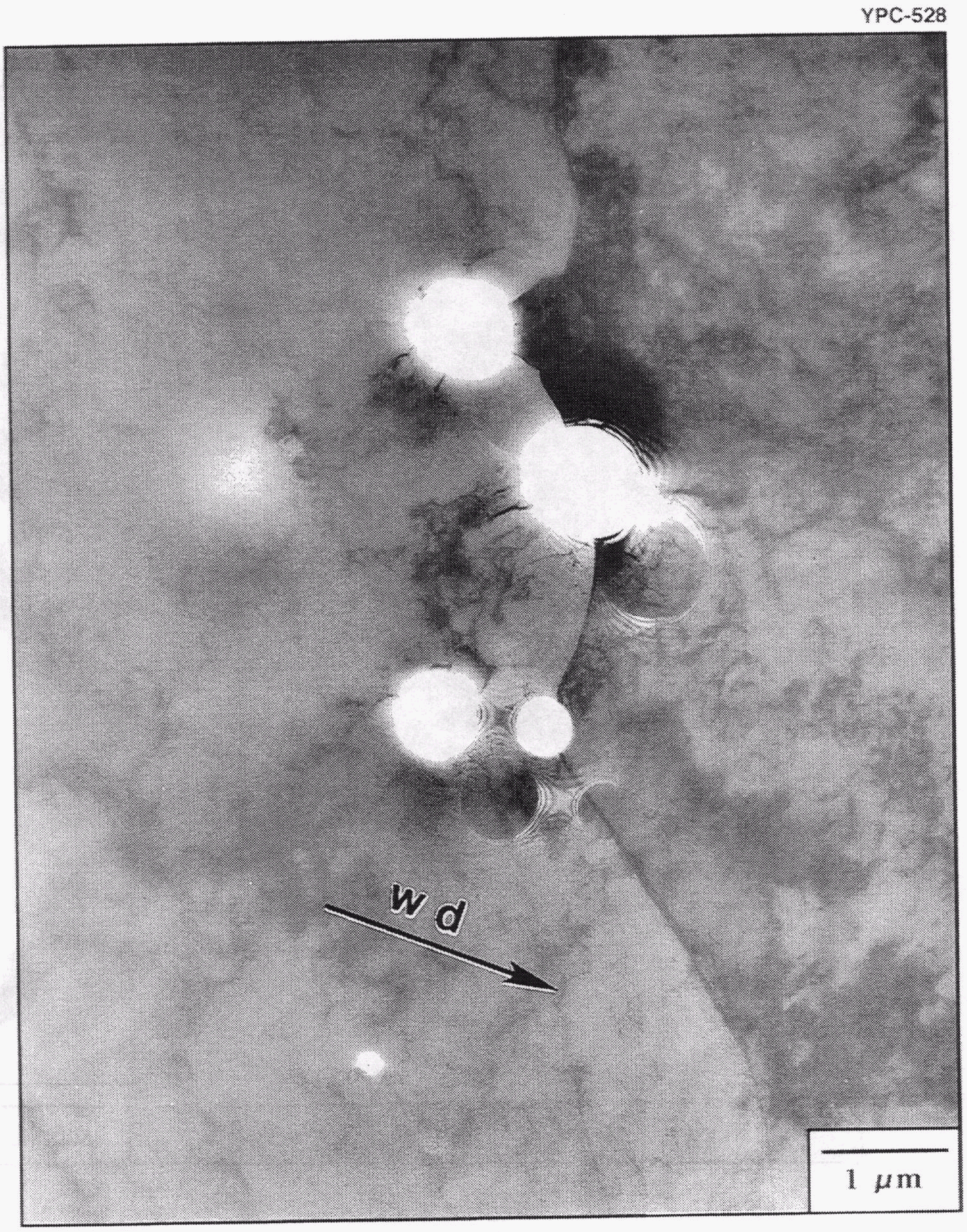

Figure 52. TEM micrograph of helium bubbles as large as 1 μm at the fusion zone of a standard weld, 9.7 appm He concentration.

shown in Figure 53. In standard welds with no applied stress, excessive grain boundary helium bubble growth occurred under the combined actions of high temperature and shrinkage-induced tensile stress and lead to catastrophic cracking. The grain boundary helium bubble volume average diameter ($VAD=(\Sigma N_i D_i^3/\Sigma N_i)^{1/3}$) at the HAZ of a standard weld with 9.7 appm He reached as high as 181.6 nm, whereas VAD in the matrix was only about 20 nm in diameter.

A sharp decrease of VAD in HAZ grain boundary helium bubbles was observed when a 55 MPa compressive stress was applied perpendicular to the welding direction during GTA welding as shown in Figure 53. The stress generated during cooling was effectively compensated by the applied compressive stress. Grain boundary helium bubble growth was retarded and did not reach the critical size to initiate catastrophic cracking. The VAD of grain boundary helium bubbles was then slowly decreased as the applied compressive stresses during welding were increased from 55 MPa to 165 MPa. The effect of stress on the suppression of helium bubble growth in the matrix was, however, not as explicit as that at grain boundaries. Helium bubble VAD in the matrix decreased from 20.5 nm in the standard weld to about 15 nm through the entire applied compressive stress range as shown in Figure 53.

In contrast to the VAD, the density of grain boundary helium bubbles was found to increase with increasing applied

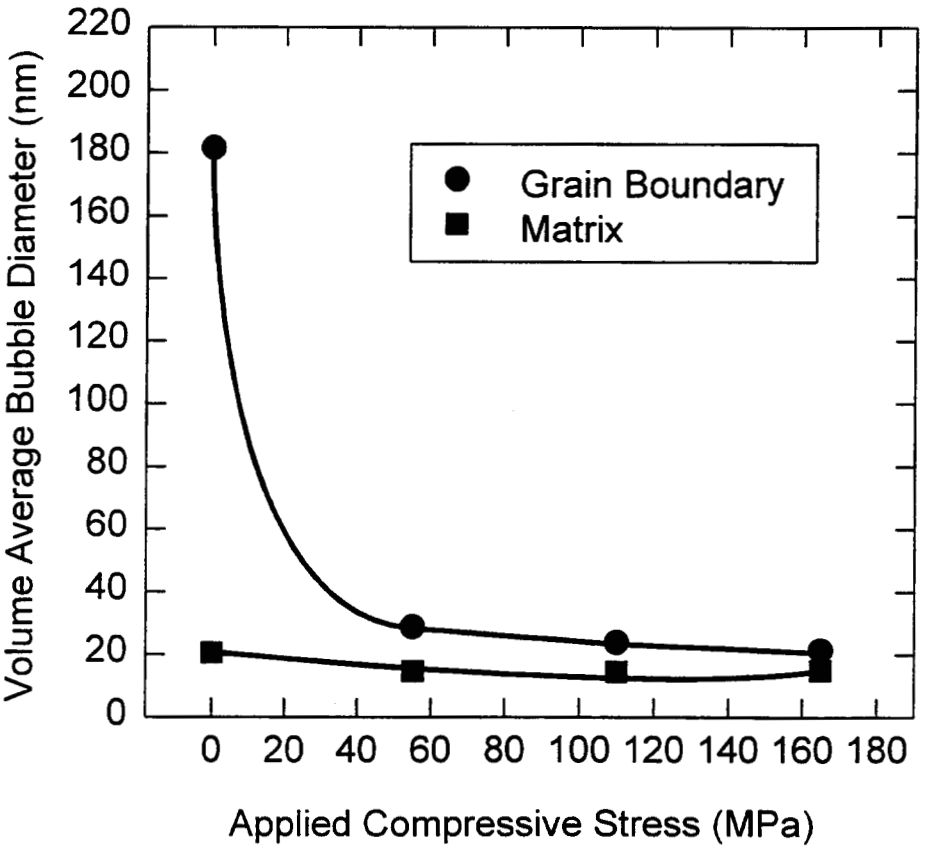

Figure 53. Effect of applied compressive stress during welding on the growth of helium bubbles of a type 316 stainless steel weld containing 9.7 appm He.

compressive stress as shown in Figure 54. However, bubble density in the matrix remained at about the same level as in the standard weld.

Figure 55 shows a TEM micrograph of a grain boundary triple junction at the HAZ of type 316 stainless steel, 9.7 appm He, with 55 MPa applied compressive stress during welding. One of the grain boundaries contains several helium bubbles as large as 200 nm in diameter while the other grain boundaries contain bubbles only about 20 nm in diameter. While in some cases no bubbles were observed in the grain boundaries at a triple junction (Figure 56), extensive helium bubble nucleation and growth were found to occur at the subgrain structure as shown in Figure 57.

In standard welding processes, a shrinkage-induced tensile stress perpendicular to the weld caused excessive helium bubble growth at grain boundaries parallel to the weld and lead to catastrophic cracking. As a compressive stress was applied during welding, coalescence and growth of helium bubbles at grain boundaries parallel to the weld were suppressed and cracking susceptibility was reduced as shown in Figure 58. The general trend of a decrease in the weld cracking phenomenon was observed at various helium concentrations. However, helium bubbles located at grain boundaries parallel to the applied compressive stress, perpendicular to the weld, were favored to grow due to bulk plate constraints with respect to the helium bubbles

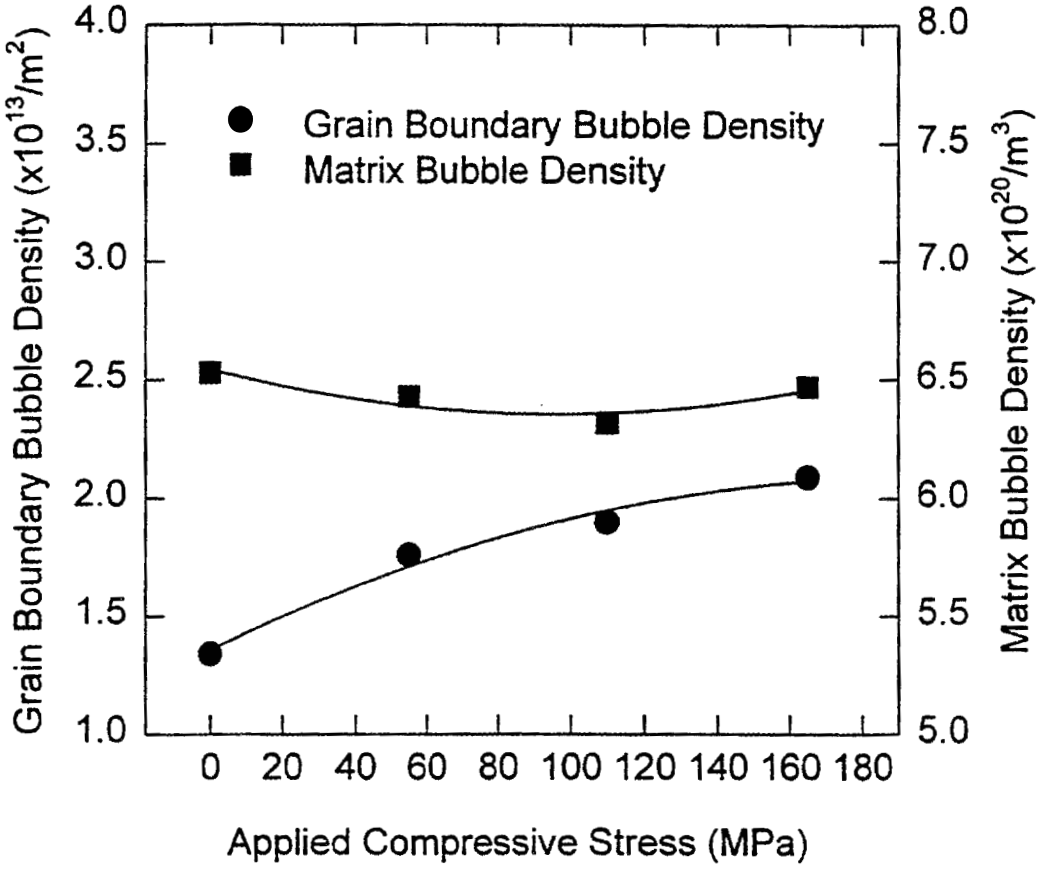

Figure 54. Effect of applied compressive stress during welding on the helium bubble density of type 316 stainless steel weld containing 9.7 appm He.

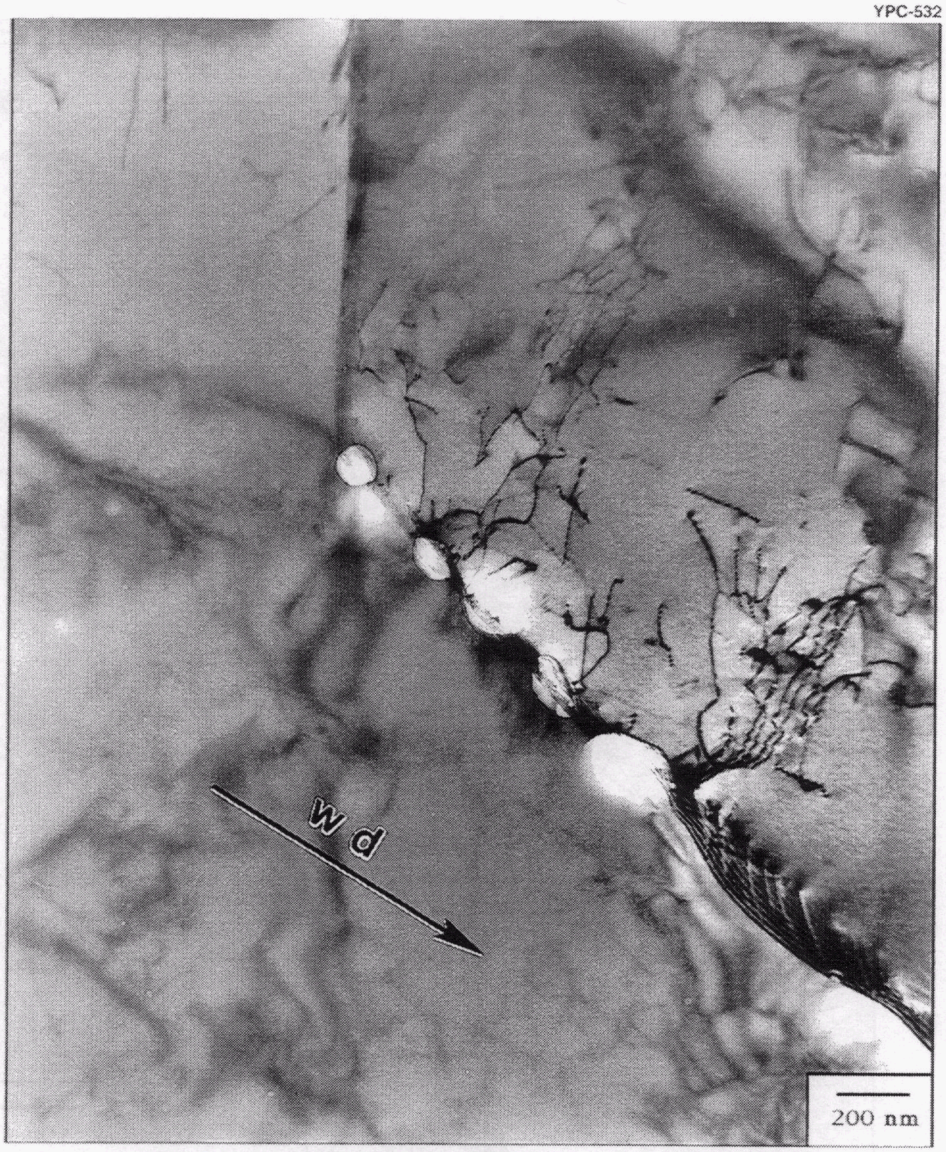

Figure 55. TEM micrograph of a grain boundary triple junction at the HAZ of type 316 stainless steel, 9.7 appm He, with 55 MPa applied compressive stress during welding. Welding direction (wd) is indicated by an arrow.

Figure 56. No bubbles were observed in grain boundaries of a junction at the HAZ of type 316 stainless steel, 9.7 appm He, with 110 MPa applied compressive stress during welding.

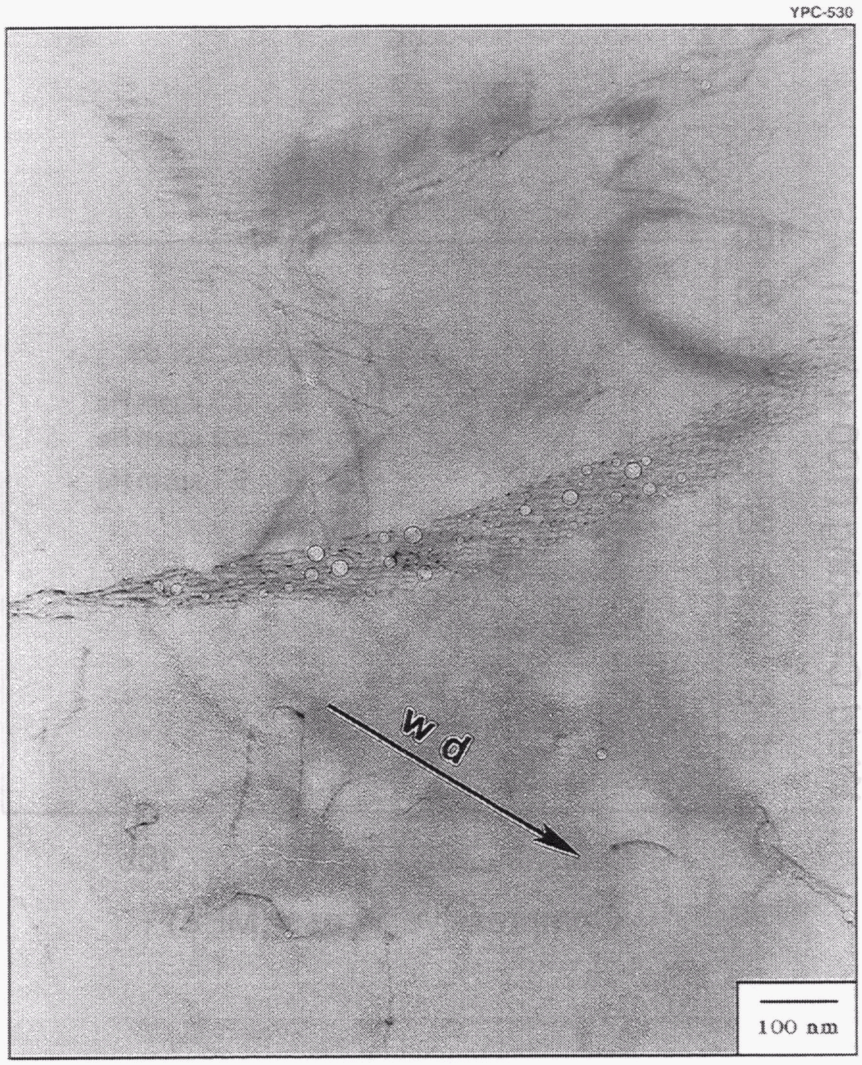

Figure 57. HAZ subgrain structure with extensive bubble nucleation and growth in type 316 stainless steel, 9.7 appm He, with 55 MPa applied compressive stress during welding.

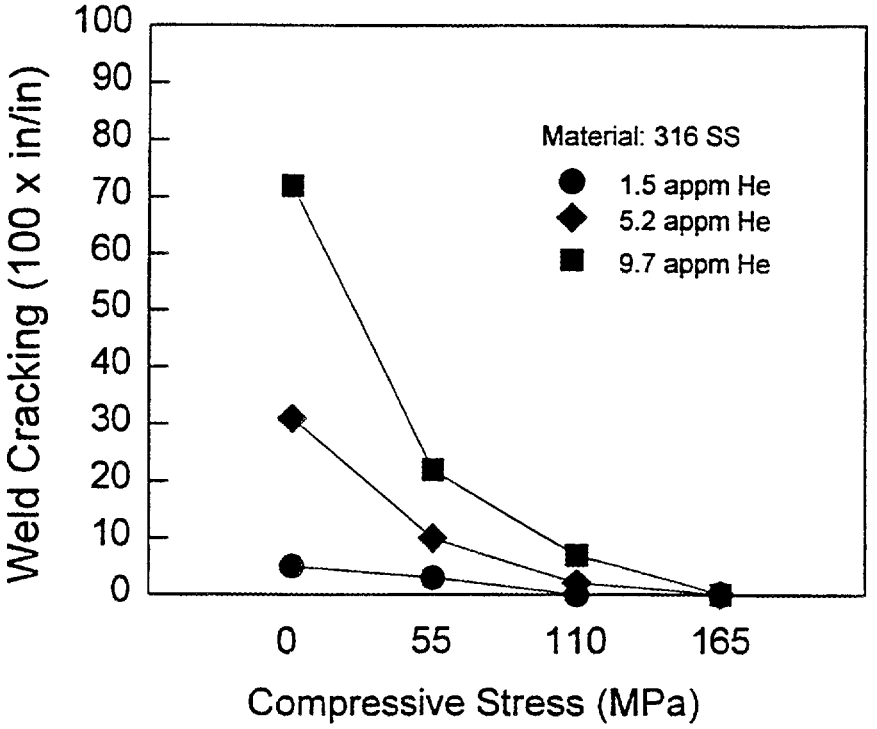

Figure 58. Weld cracking in terms of crack length per length of a weld as a function of applied stress. Weld cracking is effectively suppressed as applied compressive stress increases during welding.

residing at grain boundaries parallel to the weld. Figure 59 shows the relationship between grain boundary bubble density and grain boundary direction with respect to the weld in the modified compressive welds. Grain boundary bubble density decreased due to preferred bubble coalescence and growth as its angle to the weld increased from 0 to 90 degrees.

Further studies were performed on the grain boundary junctions to investigate the relationship between grain boundary resolved stress and grain boundary helium bubble density. Results of this study are shown in Figure 60. When two adjacent grain boundaries both contain helium bubbles, there is a 67% probability that the grain boundary with a higher resolved stress contains more helium bubbles. When one of the adjacent boundaries does not contain helium bubbles, there is a 74% probability that the bubble-containing grain boundary has a higher resolved stress than the other. The overall study shows that when a grain boundary has a higher resolved stress, there is a 70% probability that this grain boundary contains more helium bubbles than the other adjacent grain boundaries.

TEM examinations showed that grain boundary helium bubble size varied from boundary to boundary and was generally larger than those distributed in the matrix. No distinct relationship between grain boundary bubble size and the applied stress direction was observed. This was

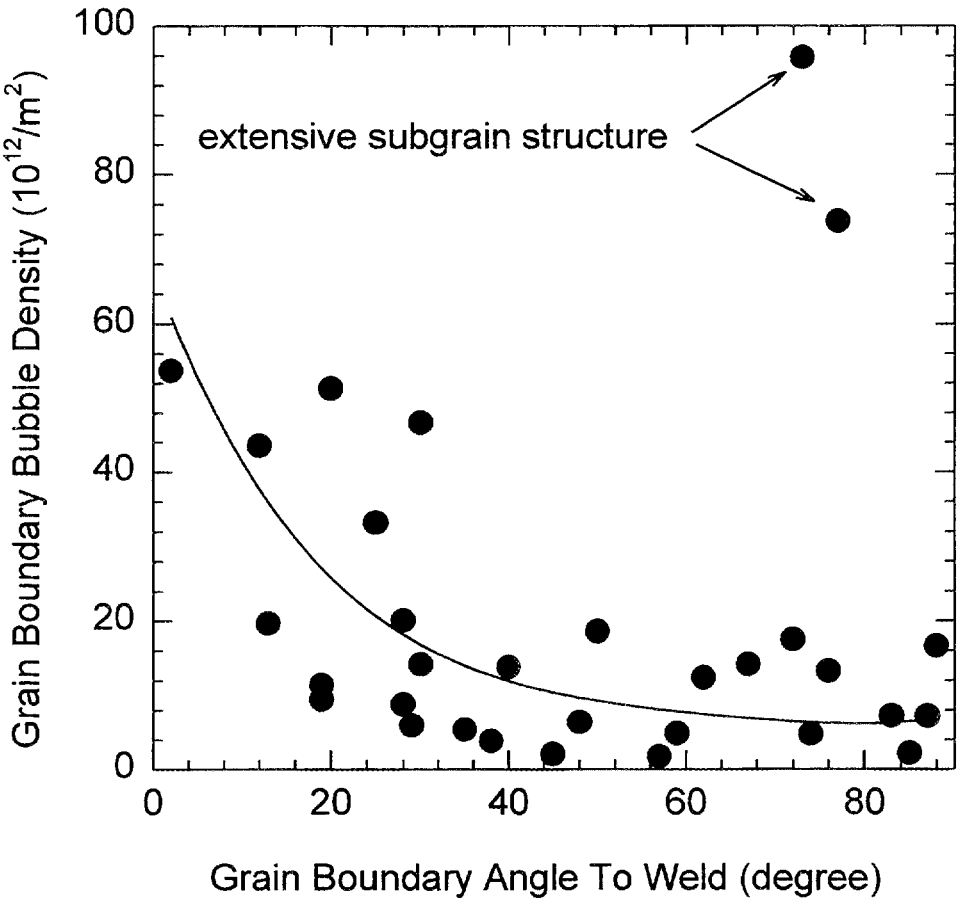

Figure 59. Relationship between grain boundary bubble density and grain boundary direction with respect to the weld in the modified compressive welds.

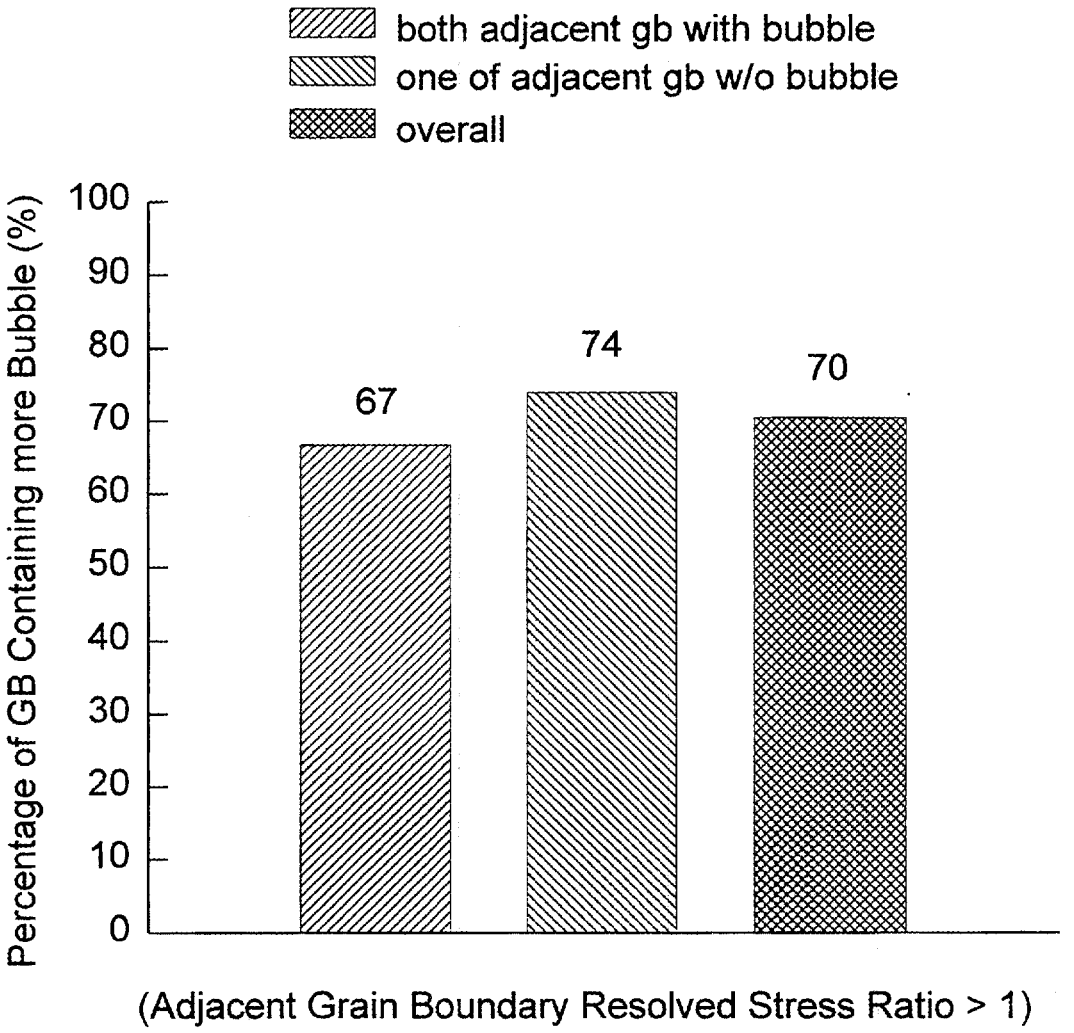

Figure 60. Relationship between adjacent grain boundary resolved stress and grain boundary helium bubble number.

attributed to the differences in the grain orientation and the location of examination, i.e., the distance away from the fusion boundary. In addition, some localized area may populate with a large amount of small bubbles associated with subgrain structures as shown in Figure 59.

Welding of Neutron Irradiated Materials

Review of previous attempts to join irradiated materials using GTA and GMA welding processes has shown varying degrees of success [7,8,11,94]. Hall et al. [7] observed intergranular cracking in the HAZs of a small fraction of welds during GTA welding of thin wall type 304 stainless steel tubing which was irradiated in the Experimental Breeder Reactor-II (EBR-II). In these materials, helium concentrations were estimated to be between 3 to 15 appm. Atkin [94] GTA welded 20% cold-worked 316 stainless steel, irradiated in EBR-II, in an unconstrained condition. Helium concentrations in these steels were estimated to be in the range of 4 to 25 appm. Bend tested samples from these welds indicated that welds were sound and free of cracks. At Savannah River Laboratory [8,11] attempts have been made to repair stress corrosion cracks in irradiated type 304 stainless steel in C-reactor and R-reactor containing different levels of helium. In steel containing 0.8 appm helium with intrinsic constraint, successful welds were made. However, later attempts to

repair similar material at a level of 1 to 3 appm helium were unsuccessful.

Crack growth specimens irradiated at 200°C in the Oak Ridge Research Reactor (ORR) in capsule ORR-MFE-6J were welded in a radiation hot cell using standard and stress-modified gas tungsten arc welding processes in this study. These materials included type 316 stainless steel with 20% cold-worked, Prime Candidate Alloy (PCA) with 25% cold-worked and tempered HT-9 steel. Figure 61 shows the crack growth specimen. Specimens were salvaged from a program that was designed to study the crack growth mechanisms but was terminated due to the inability to make a sound joint with tabs. The radioactivity level was measured to be 0.3 Ci, mainly ^{60}Co, for 316 stainless steel.

A compressive welding stage similar to the one used in the helium-doped steels was used to conduct the welding. Table 21 shows the parameters used in GTA welding of neutron irradiated materials.

Results of hot cell welding are given in Table 22. Helium concentrations in these neutron irradiated materials were calculated from the Ni content and based upon the average damage gradients for type 316 stainless steel in the ORR-MFE-6J experiment [111]. No cracking was observed in irradiated HT-9 steel with up to 2.5 appm helium. Fusion zone cracking was observed in both type 316 stainless steel and PCA alloy, using the standard GTA welding process, no

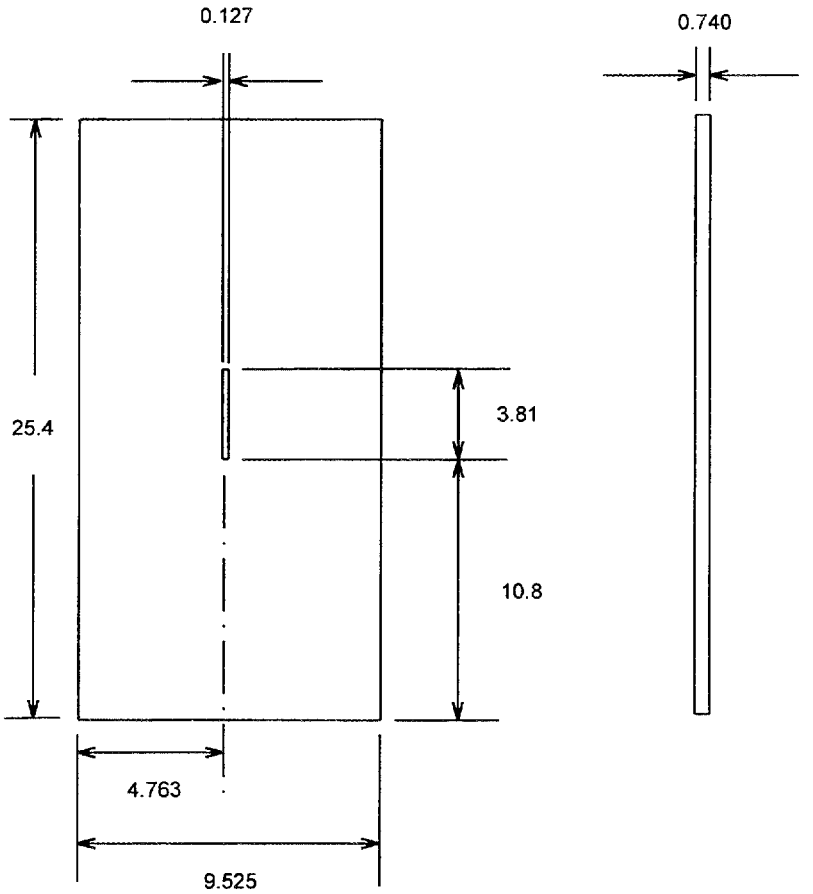

Dimensions In Millimeters

Figure 61. Crack growth specimen.

Table 21

Parameters used for the welding of neutron irradiated materials

Voltage	14 V-DC
Current	
Type 316SS, PCA	22 A
HT-9	24 A
Torch Speed	3.2 mm/s
Gas Flow	1.57×10^{-4} m^3/s
Tungsten Electrode	1.6 mm dia.
	2% thoriated

Table 22

Test matrix of crack growth specimens from the ORR-MFE-6J capsule

Alloy	Cond.	dpa	He,appm	ID	Stress	Result
316SS	20%CW	6.8	72.7	AH-17	165 MPa Comp.	Good
316SS	20%CW	6.9	74.6	AH-19	no stress	68% FZ Cracking
316SS	20%CW	6.9	74.6	AH-20	no stress	Bad Weld
316SS	20%CW	6.9	75.2	AH-24	55 MPa Comp.	Good
316SS	20%CW	6.8	75.2	AH-25	110 MPa Comp.	Good
PCA	25%CW	6.6	86.6	AT-33	165 MPa Comp.	Good
PCA	25%CW	6.3	81.1	AT-37	no stress	18% FZ Cracking
HT-9	Tempered	6.0	2.5	EH-01	165 MPa Comp.	Good
HT-9	Martensite	5.6	2.2	EH-03	no stress	Good

compressive stress applied. PCA welds were more resistant to fusion zone cracking, 18% cracking of the total weld length, as compared to 68% cracking in type 316 stainless steel. Severe fusion zone cracking was eliminated in both materials as a compressive stress as low as 55 MPa was applied during welding. Figures 62-64 show the photographs of welds of ORR irradiated materials using standard and the stress-modified welding process.

Preliminary examinations showed no macroscopic heat-affected zone cracking in any of the alloys. More detailed examination using scanning electron microscopy is necessary to evaluate the weld integrity in the heat-affected zone.

a

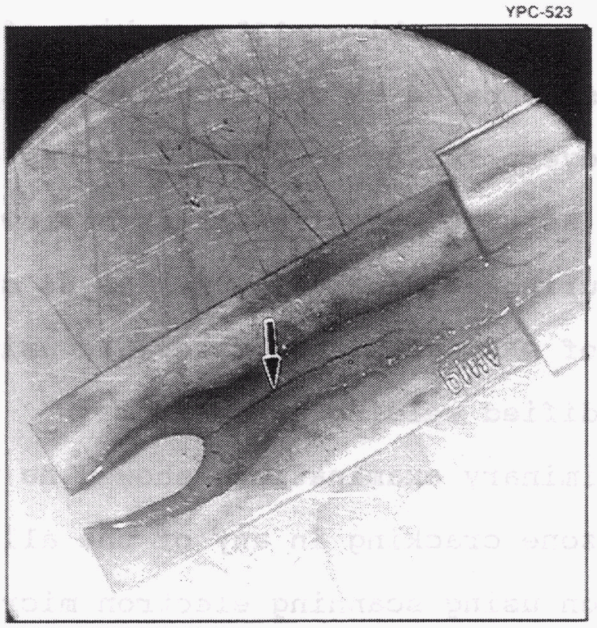

b

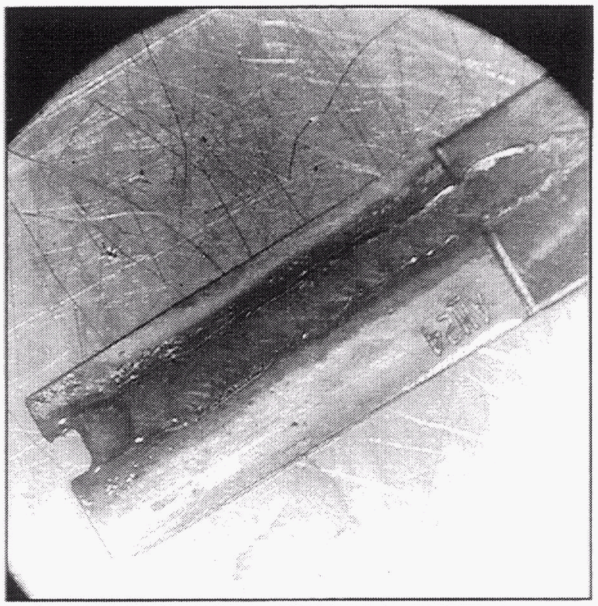

Figure 62. Photographs of welds of irradiated type 316 stainless steel using (a) standard welding process - fusion zone cracking indicated by an arrow (b) stress-modified welding process, 55 MPa - no cracking.

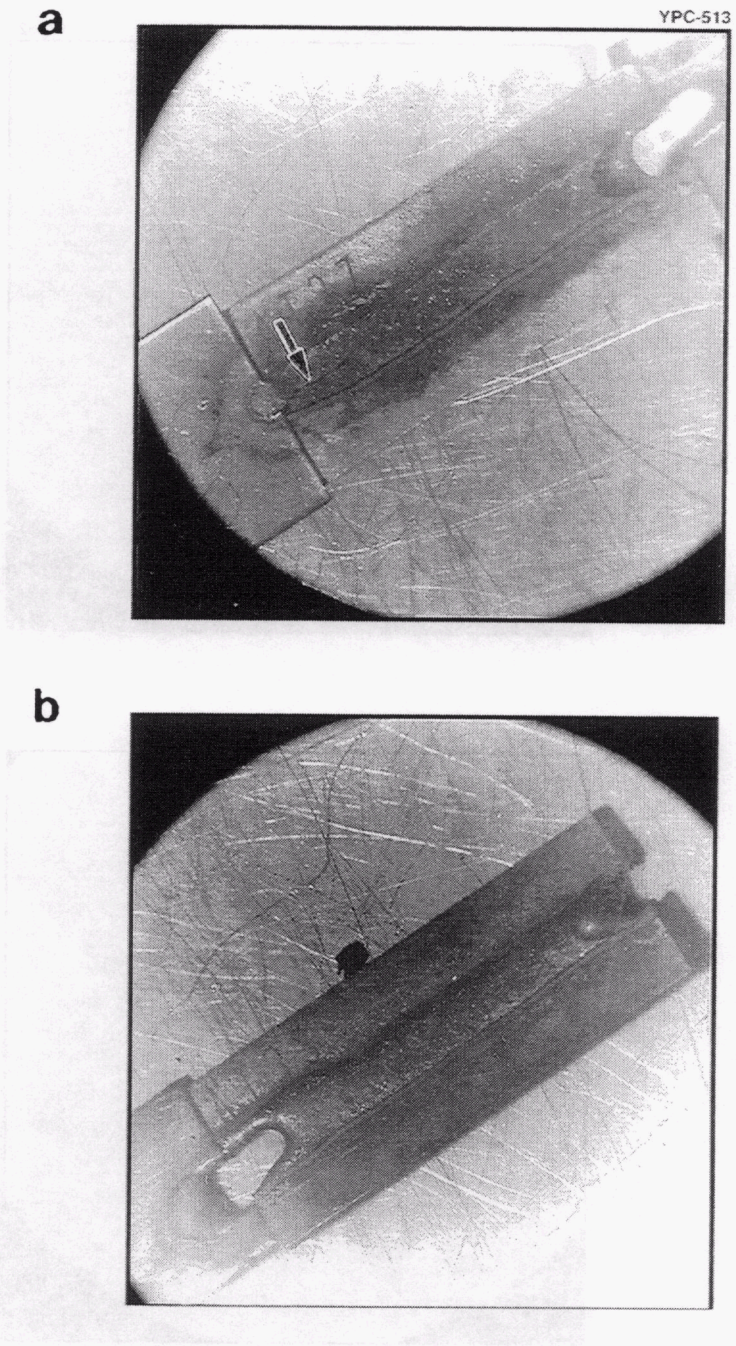

Figure 63. Photographs of welds of irradiated PCA alloy (a) standard welding process - fusion zone cracking indicated by an arrow (b) stress-modified welding process, 165 MPa - no cracking.

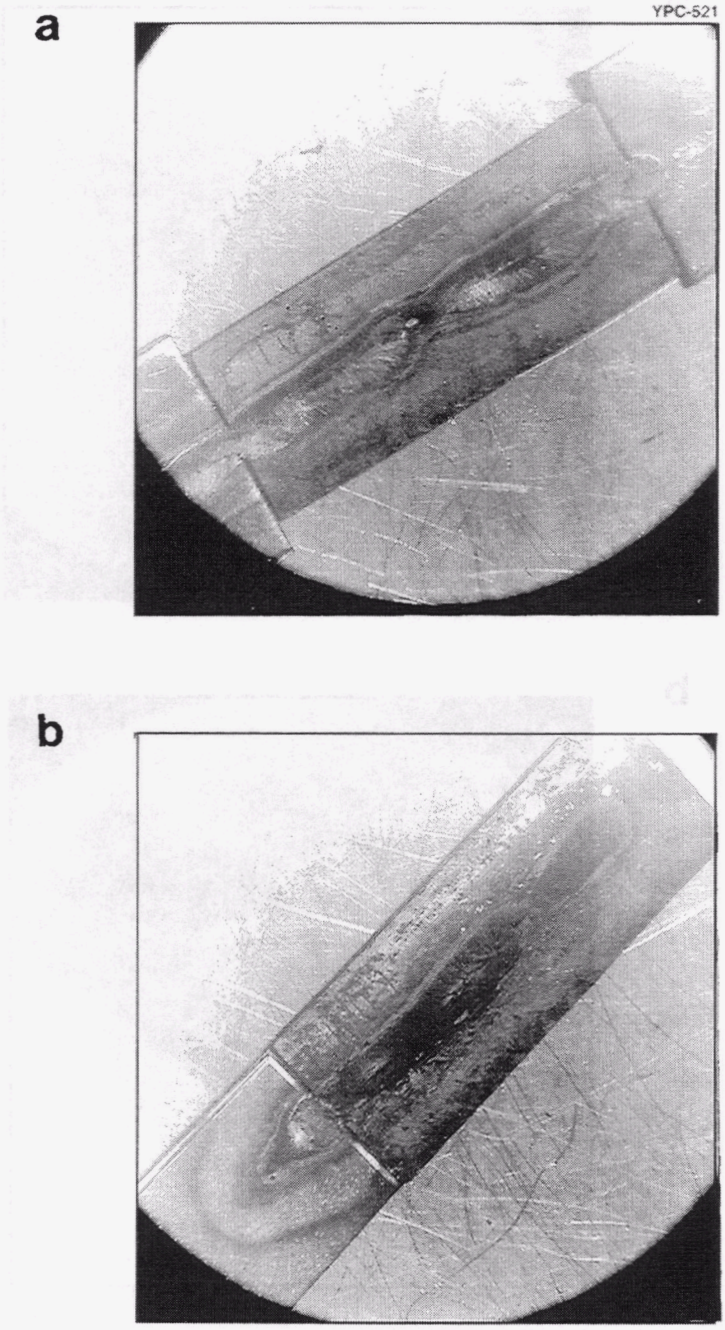

Figure 64. Photographs of welds of irradiated HT-9 steel using (a) standard welding process (b) stress-modified welding process, 165 MPa. No cracking was observed.

V. THEORETICAL INTERPRETATION

The theoretical model described by Lin et al. [16-20], has provided a scientific basis toward understanding the mechanism of helium bubble growth and weld cracking. According to the model, most of the grain boundary helium bubble growth which occurs during GTA welding is stress-assisted. The growth of grain boundary helium bubbles in the HAZ can be divided into three regimes:

In Regime I, the heat-up regime before the material reaches its melting temperature, compressive stresses are introduced normal to the welding direction due to thermal expansion of the plates. Although grain boundary helium bubbles may grow by thermal vacancy absorption and grain boundary sliding in this regime, the compressive stress tends to retard the bubble growth. Consequently, it was concluded that there is no bubble growth occurs in this heat-up period.

In Regime II, where the welding torch passes through, the material reaches its melting temperature, and a stress-free state is achieved in the melted region. Therefore, the stress is assumed to be zero in areas adjacent to the melted region. Grain boundary helium bubbles grow mainly by

vacancy absorption during this stage due to the high vacancy concentration and high diffusivity at this near-melt temperature. The grain boundary bubble growth in this regime is derived based on the theory of helium bubble growth in the matrix by vacancy absorption, presented by Greenwood and Speight [37].

Vacancy concentration, C_v, along a grain boundary available for radial diffusion (Figure 65) into the bubble can be derived from Fick's second law in cylindrical coordinates as follows [112]:

$$d^2C_v/dR^2 + (1/R)dC_v/dR = 0 \qquad (14)$$

where R is the distance from the center of the grain boundary bubble. The general solution to the above equation can be expressed as

$$C_v = A + B\ln R \qquad (15)$$

where A and B are constants. The flux of vacancies diffusing into the bubble therefore can be expressed as

$$J_v = -D_{gb}(dC_v/dR) = -D_{gb}B/R \qquad (16)$$

The constant B can be determined by applying boundary conditions.

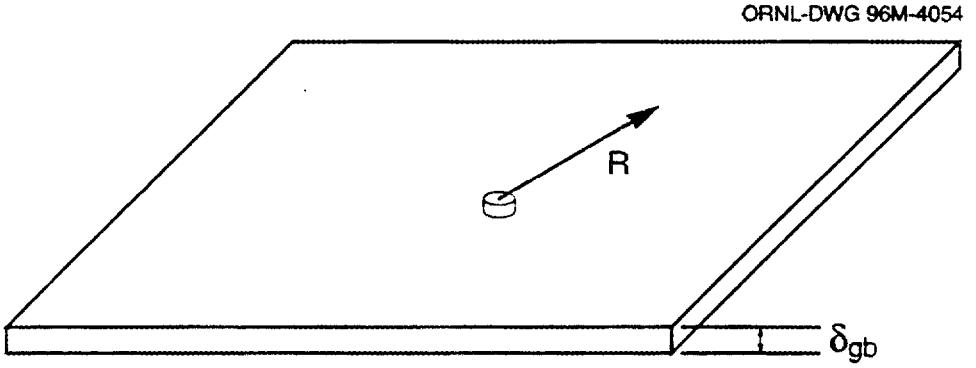

Figure 65. Vacancy diffusion into a bubble along a grain boundary is everywhere radial.

At grain a boundary bubble surface, where $R=R_i$, the vacancy concentration, C_v can be expressed as

$$C_v = C_v^e \exp[-(p-2\gamma/R_i)\Omega/kT] \tag{17}$$

where p is internal gas pressure, γ is the bubble surface energy, Ω is the atomic volume, k is the Boltzmann's constant and T is the temperature. C_v^e is the equilibrium vacancy concentration at temperature T and has the form of

$$C_v^e = \exp[-(\Delta H-T\Delta S)/kT]/\Omega \tag{18}$$

where ΔH is the vacancy formation energy and ΔS is the vacancy formation entropy.

At a distance away from the center of a bubble, R_e, the vacancy concentration is in the equilibrium state, i.e.,

$$C_v = C_v^e \tag{19}$$

therefore the constant B can be expressed as

$$B = C_v^e\{1-\exp[-(p-2\gamma/R_0)\Omega/kT]\}/\ln(R_e/R_i) \tag{20}$$

Since R_e is generally much greater then R_i [19], the vacancy flux can be approximated by

$$J_v \approx D_{gb}C_v^e\{1-\exp[-(p-2\gamma/R_0)\Omega/kT]\}/R \qquad (21)$$

The interface between the grain boundary and bubble has an area of $2\Pi R\delta_{gb}$. Therefore, the grain boundary bubble growth rate can be expressed as

$$dV/dt = 2\Pi R\delta_{gb}*J_v*\Omega \qquad (22)$$

where δ_{gb} is the grain boundary thickness.

The growth rate of a grain boundary bubble radius is hence,

$$dR/dt = D_{gb}\delta_{gb}\Omega C_v^e\{1-\exp[-(p-2\gamma/R_0)\Omega/kT]\}/2R^2 \qquad (23)$$

Since the term $\exp[-(p-2\gamma/R_0)\Omega/kT]$ is found to be much smaller than 1, the above equation can then be simplified as

$$dR/dt = D_{gb}\delta_{gb}\Omega C_v^e/2R^2 \qquad (24)$$

Therefore, the bubble radius after Regime II, R_{ii}, can be expressed by

$$R_{ii}^3 - R_i^3 = 3\delta_{gb}\Omega D_{gb}C_v^e\Delta t/2 \qquad (25)$$

where

R_{ii} = bubble radius, m,

R_i = bubble radius at the end of Regime I, m,

δ_{gb} = grain boundary thickness, m,

Ω = atomic volume, m^3,

D_{gb} = grain boundary vacancy diffusivity, m^2/s,

C_v^e = equilibrium vacancy concentration, m^{-3}, and

Δt = elapsed time in Regime II, s.

Grain boundary vacancy diffusivity [113] in Regime II can be expressed by

$$D_{gb}\delta_{gb} = 7.7 \times 10^{-8}\exp(-1.65eV/\kappa T),\ m^3/s \qquad (26)$$

Parameters used for the above calculation are listed in Table 23. The elapsed time in Regime II is calculated to be 1.57 seconds (weld bead size, 5 mm long, divided by the welding speed, 3.2 mm/s). Figure 66 shows the predicted grain boundary helium bubble growth in Regime II during welding.

Ostwald ripening [42,43] and coalescence [36-38,115] are two of the other possible bubble growth mechanisms in Regime II. Assuming ideal gas behavior and spherical gas bubbles, in thermal equilibrium, the relation between the

Table 23

Parameters used in Regime II calculation

Parameter	Symbol	Value
Lattice parameter [114]	a_0	3.64×10^{-10}m
Bubble radius at end of Regime I	R_i	1×10^{-9}m
Atomic volume	Ω	1.2057×10^{-29}m^3
Equilibrium vacancy concentration	C_v^e	6.3523×10^{23}m^{-3}
Elapsed time in Regime II	Δt	1.57s
Initial temperature	T_i	293K
Peak temperature	T_{peak}	1573K
Activation energy for diffusion	Q_{diff}	1.65eV
Vacancy formation energy [114]	ΔH	1.8eV
Vacancy formation entropy [114]	ΔS	1.5κ
Boltzmann's constant	κ	8.62×10^{-5}eV/K

$\Omega = a_0^3/4$, m^3

$D_{gb}\delta_{gb} = 7.7 \times 10^{-8}\exp(-1.65\text{eV}/\kappa T)$, m^3/s [113]

$C_v = [\exp(-\Delta H/\kappa T)\exp(\Delta S/\kappa)]/\Omega$, m^{-3}

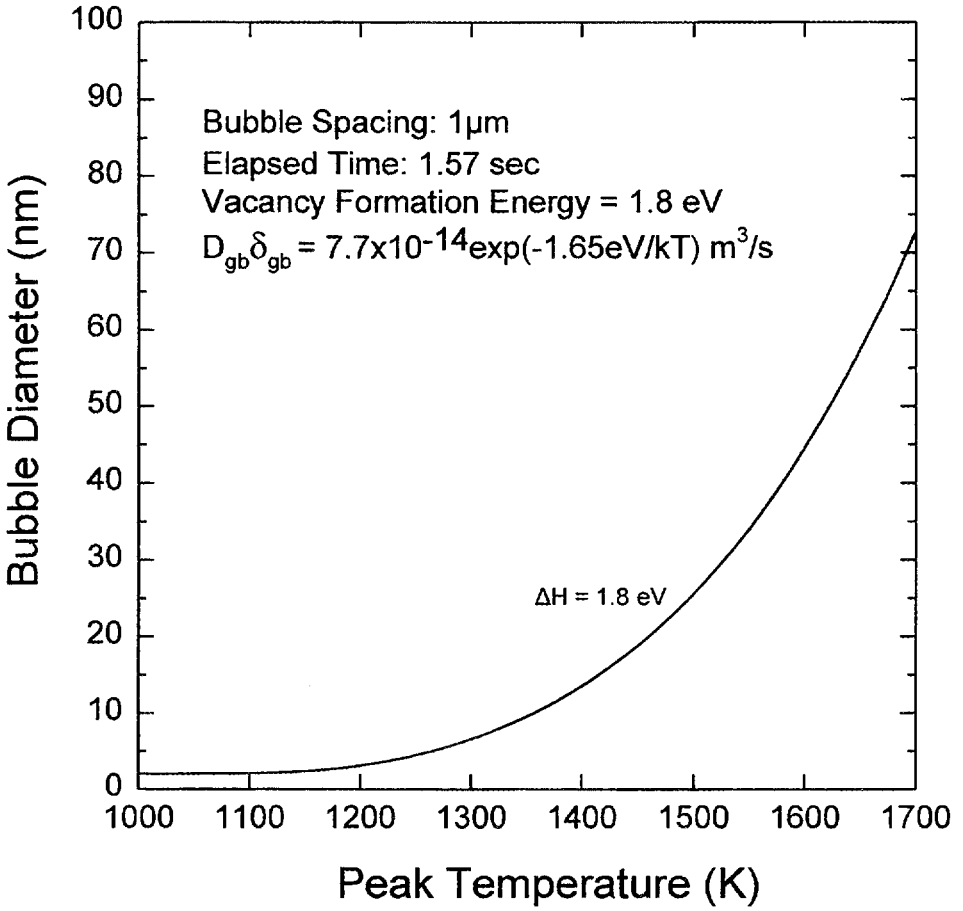

Figure 66. Predicted grain boundary helium bubble growth in Regime II during welding.

bubble gas pressure P and the atomic concentration of gas C_g in the surrounding metal can be expressed as

$$C_g \propto P*\exp(-G_g/kT) \tag{27}$$

where G_g is the solution energy of a gas atom. Since the bubble gas pressure depends on the bubble radius, $p=2\gamma/r$, concentration gradients exist between various sizes of bubbles leading to gas atom permeation from small to large bubbles. This process is called Ostwald ripening. The dissolution of small bubbles reduces the free energy as the mean bubble volume is increased. The radius growth rate of a bubble by Ostwald ripening is given by [43]

$$dR/dt=D_g(1/R_m-1/R)\exp(-G_g/kT) \tag{28}$$

Where D_g is the gas atom diffusivity, G_g is the solution energy of a gas atom, and R_m is the arithmetic mean of bubble radii. The growth of a gas bubble by Ostwald ripening is primarily dominated by the re-dissolution of gas atoms in the metal. However, since helium is practically insoluble in metal, helium bubble corasening by this mechanism is assumed negligible.

Bubble coalescence in metal is believed to result when collisions occur between bubbles as they migrate by surface diffusion through the metal [116]. In Barnes and Mazey's

experiment, copper foils deposited with helium atoms were examined in an electron microscope. It was found that helium bubbles formed during pulse heating in the electron beam and that bubbles indeed migrated and collided so their number steadily reduced and their size increased [117]. The migration speed varied approximately as the reciprocal of the bubble radius. Their observation also supports that the re-dissolution of gas atoms from bubbles does not occur in the case of helium bubbles. After several generations of coalescence, the mean bubble radius R can be expressed as [36]

$$dR/dt = 0.74 D_s m a_0^4 kT/\gamma R^4 \qquad (29)$$

where D_s is the surface diffusivity, m is the total number of gas atoms a_0 is the interatomic distance, and γ is the surface energy. The above equation assumes that the bubbles migrate by surface diffusion, that the gas behaves ideally, that the gas pressure is in equilibrium with the surface tension, that there is no bubble interaction occurs except immediate coalescence, and that the solid is a perfect, infinite crystal.

Figure 67 shows the predicted results of bubble coalescence after GTA welding of type 316 stainless steel. Helium bubbles grow rapidly by coalescence in the heat-up period as the bubble radii are still small. As bubbles

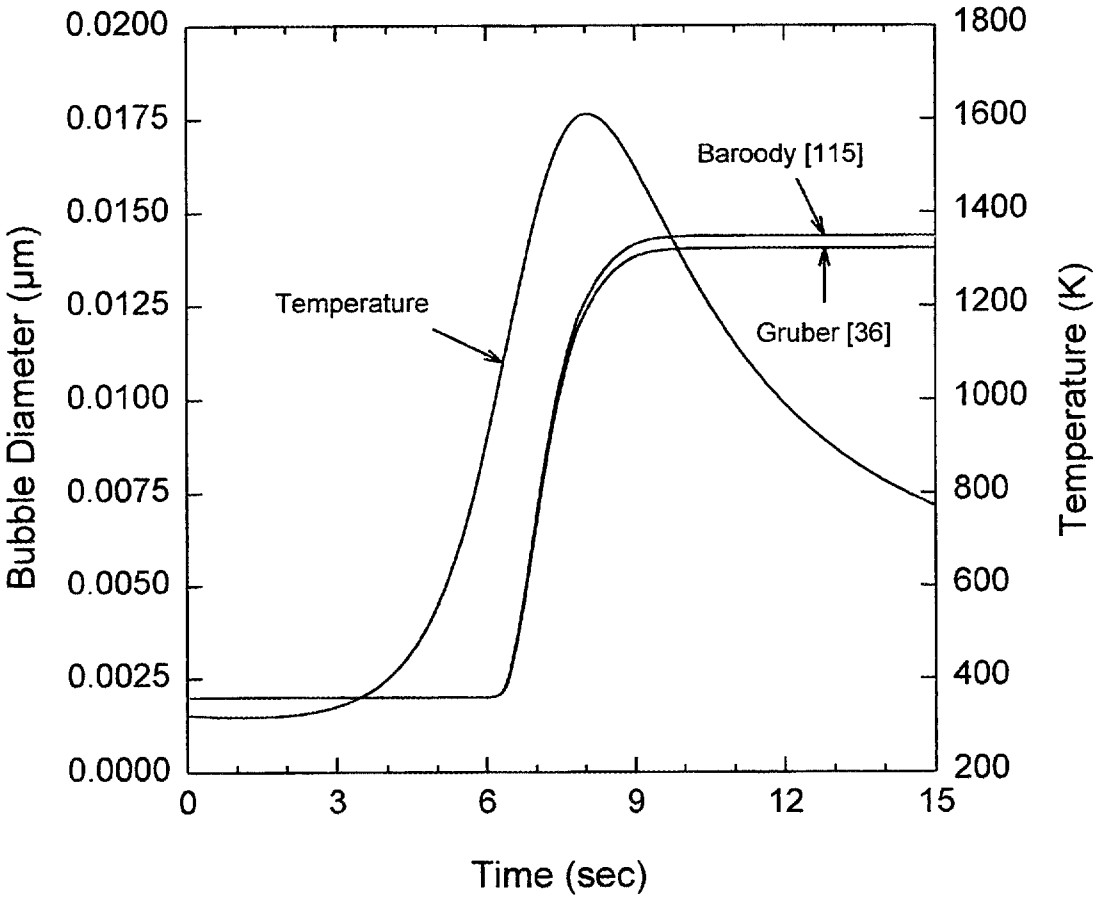

Figure 67. Predicted results of bubble coalescence after GTA welding of helium containing type 316 stainless steel.

continue to grow, the bubble radii become large, the rate of growth slows, as seen by equation (29) and bubble coalescence becomes negligible.

As the heat source passes through, the onset of Regime III, molten metal solidifies and subsequently cools down. The contraction of weld metal generates tensile stresses perpendicular to the weld in the nearby regions as discussed in the previous section. Helium bubbles located at heat-affected zone grain boundaries parallel to the weld grow rapidly under the influence of this thermal shrinkage stress. Stress-assisted bubble growth dominates in this regime, and most of the grain boundary bubble growth during welding occurs here.

The grain boundary bubble growth processes can be categorized into two mechanisms: surface diffusion controlled [118,119] and grain boundary diffusion controlled [2,46,50-53] mechanisms. Grain boundary bubbles grow as the atoms are transported from bubble surfaces to the adjacent grain boundaries. In surface diffusion controlled bubble growth, the surface diffusivity is smaller than the grain boundary diffusivity and therefore bubbles tend to grow into an elongated shape. In contrast, in grain boundary diffusion controlled bubble growth, grain boundary diffusivity is smaller than the surface diffusivity and bubbles tend to maintain the equilibrium spherical shape due to rapid surface atom redistribution.

Results from the TEM examinations revealed spherical helium bubbles attached to the grain boundaries indicating grain boundary diffusion controlled bubble growth occurred during welding. Figure 68 shows the surface and grain boundary diffusivities of type 316 stainless steel as a function of temperature.

Extensive studies [46,51-53,121,122] have been performed on the theory of stress-assisted bubble/cavity growth after the first introduction by Hull and Rimmer in 1959 [46]. Speight and Harris [52] advanced the theory through further analysis in 1967 and a similar analysis was brought out by Weertman [51] in 1973. A more complete analysis on the kinetics of stress-induced grain boundary void growth was performed by Speight and Beere in 1975 [53].

The growth of a grain boundary bubble is due to the continuous release of atoms from within a ring around each bubble along the grain boundary. The following derivation follows Herring [123]. The rate of bubble growth is determined by the gradient of chemical potential, ∇f, in the plane of the grain boundary. The flux, J_g ,can be expressed as

$$J_g = \nabla f(D_{gb}/kT\Omega) \tag{30}$$

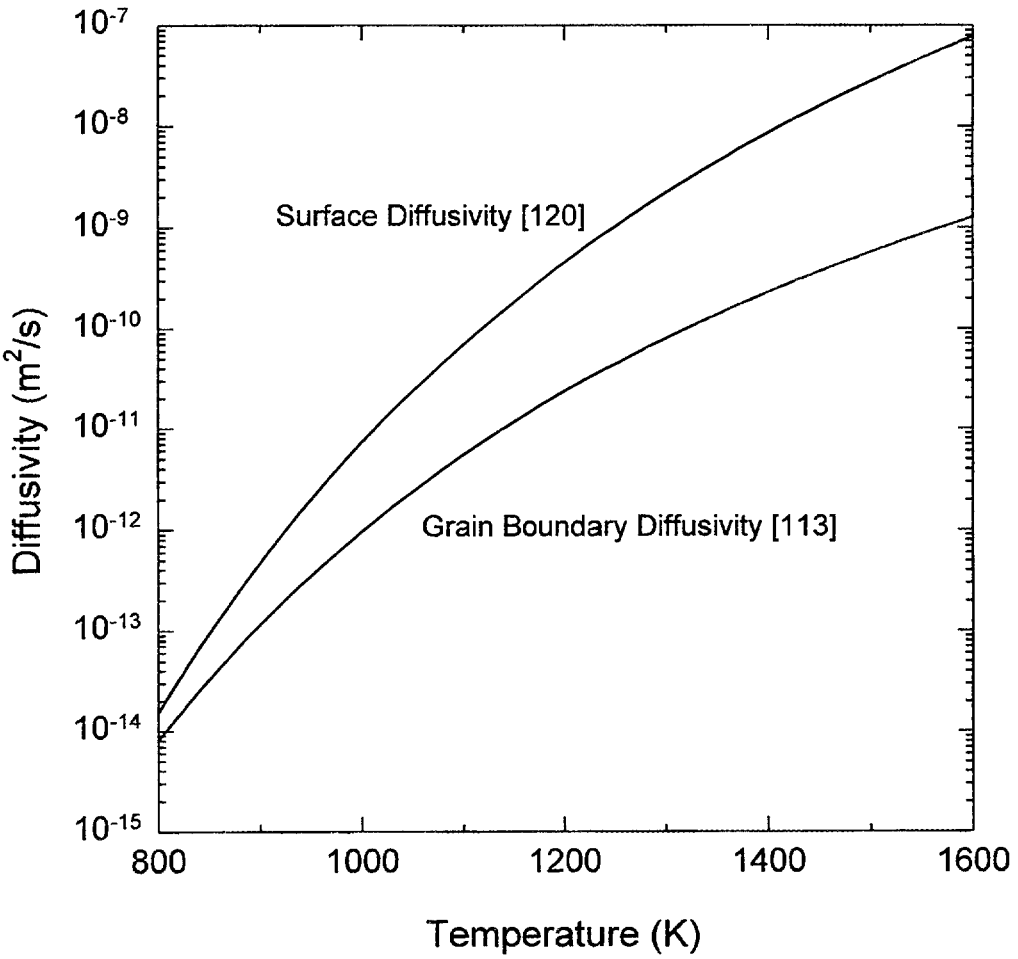

Figure 68. Surface and grain boundary diffusivities of type 316 stainless steel as a function of temperature.

where D_{gb}, k, T and Ω have the same definition as in the previous section, and ∇f is to be determined at the bubble surface.

The grain boundary potential can be approximated by $-\sigma_g\Omega$, where σ_g is the tension acting normal to the grain boundary. The σ_g has a maximum value of σ-P on a grain boundary normal to the direction of externally applied stress σ. On the other side, the potential of a bubble on the surface is equal to surface tension of the metal $-2\gamma\Omega/R$.

Therefore, the flux J_g can be expressed as

$$J_g \approx D_{gb}(\sigma-P-2\gamma/R)/akT \tag{31}$$

where a is the center to center bubble spacing and, P is the internal bubble pressure. With an area of $2\pi R\delta_{gb}$ available for diffusion to take place, the rate of the increase in bubble volume is given by

$$dV/dt \approx 2\pi R\delta_{gb}D_{gb}\Omega(\sigma-P-2\gamma/R)/akT \tag{32}$$

Assume surface diffusivity is high enough to maintain the spherical shape of the bubbles, then the growth rate of an isolated grain boundary bubble can be approximated as

$$dR/dt \approx \delta_{gb}D_{gb}\Omega(\sigma-P-2\gamma/R)/2RakT \tag{33}$$

The shrinkage stress induced by weld solidification and subsequent cooling is the largest contribution to the thermal stress, σ_t, which is much greater than P. Therefore, the approximated expression of the thermal stress during welding can be described as

$$\sigma_t(t) = \sigma_s(t) - 2\gamma(t)/R(t) \tag{34}$$

where

$\sigma_s(t)$ = shrinkage stress at time t, Pa,

$\gamma(t)$ = surface energy of bubbles, at time t, J/m^2, and

$R(t)$ = bubble radius at time t, m.

In the case of this study, the initial grain boundary helium bubbles are assumed to be equal in size and populated in a square array such that the growth rate of grain boundary helium bubbles can be expressed by [46]

$$dR/dt = 2\Pi\delta_{gb}D_{gb}\Omega\sigma_t/akTR \tag{35}$$

where

κ = Boltzmann's constant, eV/K,

a = average bubble spacing, m,

R = bubble radius, m,

T = temperature, K,

Ω = atomic volume, m^3,

δ_{gb} = grain boundary thickness, m,

σ_t = thermal stress, Pa, and

D_{gb} = grain boundary vacancy diffusivity, m^2/s.

Equation (36) clearly indicates that not only temperature and grain boundary diffusivity affect bubble growth, changes in thermal stress, σ_t, can also significantly alter the bubble growth rate.

In this study, grain boundary thickness is assumed to be 4 Å. The average bubble spacing on grain boundaries was assumed to be 1 μm based on the results of SEM examination of the HAZ fracture surfaces, which were fully decorated with dimples about 1 μm in diameter. The initial bubble radius at the beginning of Regime III, i.e., the final radius at the end of Regime II, was calculated to be 0.019 μm using equation (26).

The shrinkage stresses which arise during welding are not easy to describe explicitly. This transverse shrinkage stress across the weld can be approximated by the following equation according to elasticity theory,

$$\sigma_s(t) = E(t)\alpha(t)\Delta T \tag{36}$$

where

$E(t)$ = modulus of elasticity at time t, Pa,

ΔT = temperature increment, K, and

$\alpha(t)$ = thermal expansion coefficient at time t, 1/K.

It should be emphasized that this study is not meant to predict the resulting stress state of the weld but rather to give physical insight into what may be occurring during the welding of helium containing materials.

The modulus of elasticity and the instantaneous thermal expansion coefficient up to the melting point, ~1400°C, are obtained by extrapolating the known data (Table 24) for type 316 stainless steel [124].

The surface energy used in the calculation in Regime III is based on the results of a study by Murr et. al. [125] on type 304 stainless steel as shown in Table 25. The results show a temperature dependent surface free energy (Figure 69), which can be approximated as

$$\gamma(t) = -0.00151 \times T(t) + 4.11 \qquad (37)$$

where T(t) is the temperature at time t in Regime III.

Results of grain boundary bubble growth calculations for the final stage during welding, Regime III, are shown in Figure 70. In the standard weld (no compressive stress) heat-affected zone cracking occurs approximately 1.8 seconds

Table 24

Temperature dependent Young' modulus and thermal expansion coefficient of type 316 stainless steel [124]

Temperature T(°F)	Modulus E(GPa)	Temperature T(°F)	Ther. Exp. Coff. $\alpha(10^{-6}/°F)$
167	191.4	70	8.4632
212	190.1	100	8.6148
257	188.7	200	9.0875
302	187.2	300	9.5127
347	185.6	400	9.8931
392	184.0	500	10.232
437	182.3	600	10.532
482	180.5	700	10.796
527	178.6	800	11.028
672	176.7	900	11.229
617	174.7	1000	11.404
662	172.6	1100	11.555
707	170.5	1200	11.685
752	168.3	1300	11.797
797	166.0	1400	11.894
842	163.7	1500	11.979
887	161.4	1600	12.056
932	159.0		
977	156.6		
1022	154.1		
1067	151.6		
1112	149.1		
1157	146.5		
1202	143.9		
1247	141.3		
1292	138.6		
1337	135.9		
1382	133.2		
1427	130.5		

$$E(t) = 28.33669-2.882211*10^{-3}T-3.697849*10^{-6}T^2+7.709188*10^{-10}T^3$$

$$\alpha(T) = 8.09139+5.496948*10^{-3}T-2.679852*10^{-6}T^2+4.95473*10^{-10}T^3$$

Table 25

Surface free energy of type 304 stainless steel [125]

Temperature (°C)	Surface free energy J/m^2
1060	2.190
1160	1.925
1260	1.585
1360	1.800

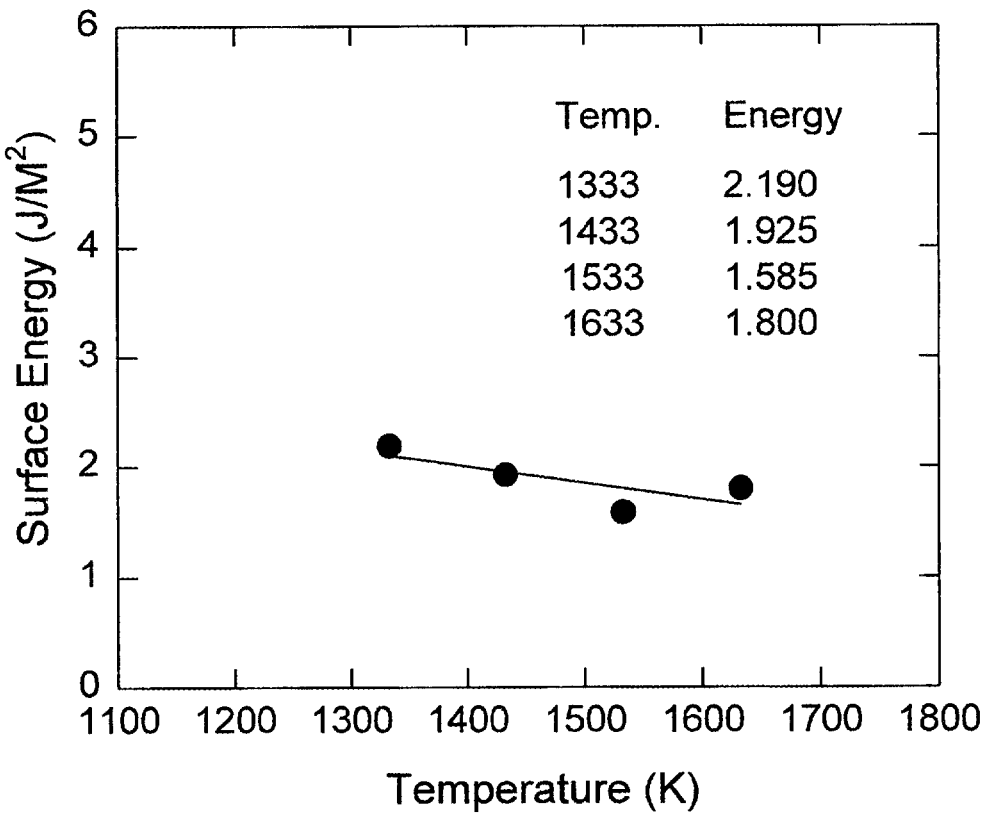

Figure 69. Surface free energy as a function of temperature.

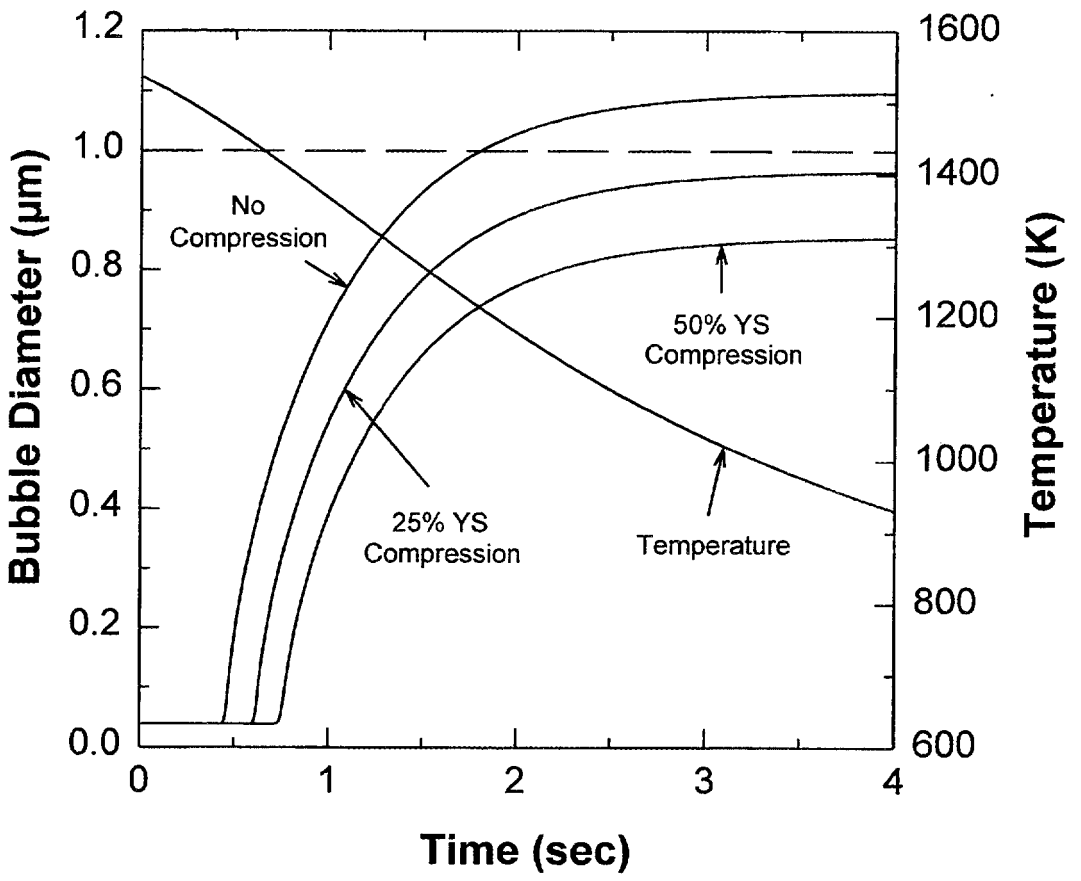

Figure 70. Predicted grain boundary bubble growth in final stage, Regime III, during welding.

after the onset of Regime III, when bubbles reach 1 μm. This is consistent with the results of videotaping during welding, which showed cracks that initiate 1 to 2.2 seconds after passage of the weld pool. When a compressive stress is applied during welding, bubble growth is retarded, and bubble size may never reach the critical size which leads to cracking. Bubble growth was also retarded when the bubble surface tension is greater than thermal tensile stresses, as indicated at the beginning region of Figure 70.

A comparison of various models of grain boundary bubble/cavity growth in Regime III is given in Figure 71. A greater bubble growth rate was predicted by Weertman [51] than by Hull and Rimmer's model by considering different geometry factor, a function of bubble radius and spacing [46]. As bubble size approaches the critical size, i.e., bubble spacing, Speight and Harris [52] showed a significant increase in bubble growth rate while Speight and Beere predicted the highest growth rate among all the models. With the consideration of vacancy volume relaxation, similar grain boundary bubble growth patterns were predicted by Loh [122] and Dobes and Cadek [121] as in Hull and Rimmer's model. However, both models predict much lower bubble growth rate compare to others.

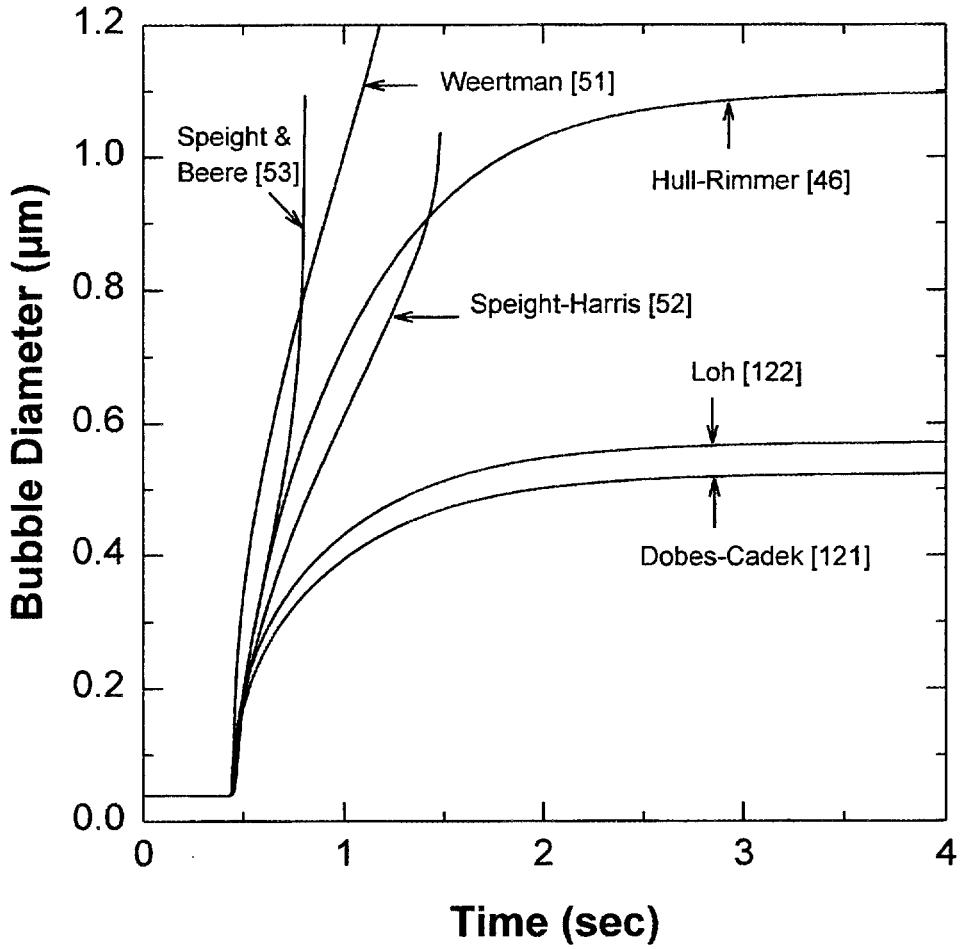

Figure 71. Comparison of grain boundary bubble growth models in Regime III.

VI. DISCUSSIONS

Theoretical interpretation

During the heat-up period of the welding process, compressive stresses arise due to thermal expansion of the material and it is therefore logical to assume the bubble growth will be suppressed in this regime. In Regime II, high temperatures prevail and thermal vacancies are abundant. Heat-affected zone grain boundary bubbles grow principally by vacancy condensation in this period. The degree of vacancy condensation is controlled by the vacancy formation energy in this regime as shown in Figure 72. High temperature aging experiments [19] of type 316 stainless steel containing 256 appm helium were found to yield much smaller bubble sizes compared to the predicted values using the vacancy condensation model as described in Regime II. TEM disks were thermally aged at 800, 900 1050 and 1300°C for one hour. Figure 73 shows the relationship between results of the aging experiment and theoretical models. However, further analyses [16,19] showed that bubbles grow so rapidly under the influence of shrinkage stress that the difference in predicted bubble sizes between Regime II and III is so great that growth in Regime II is insignificant.

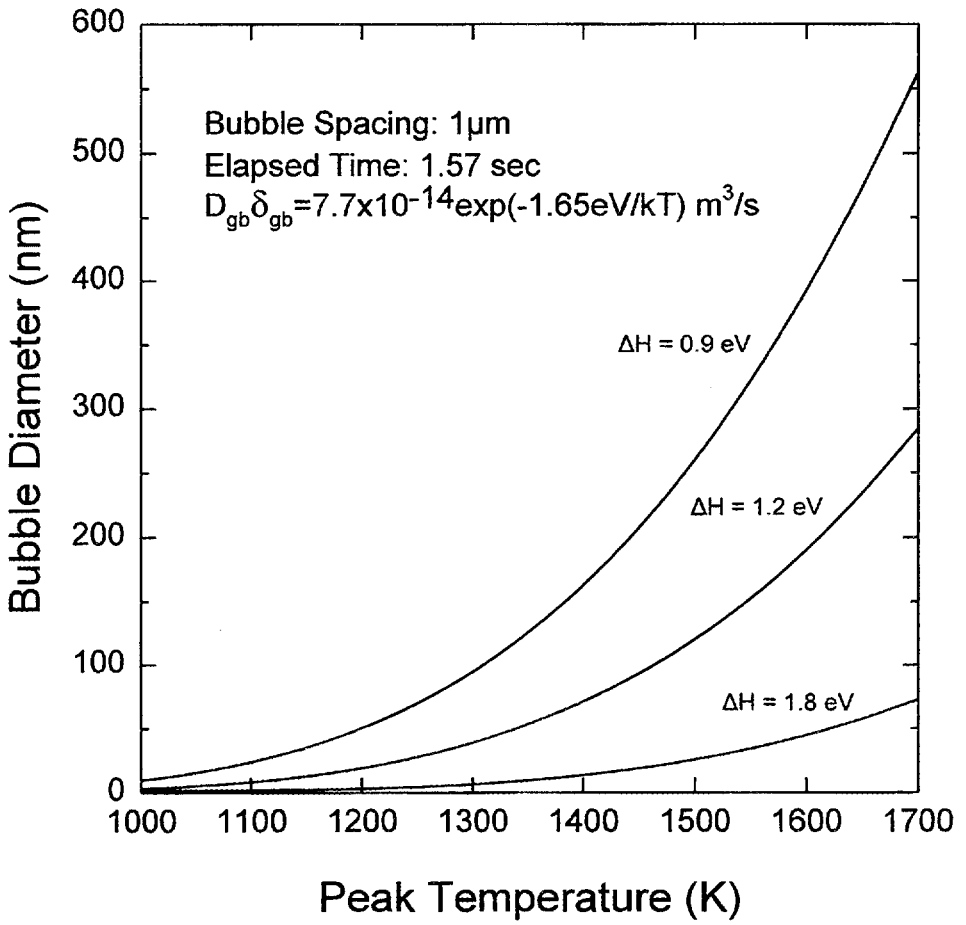

Figure 72. Bubble diameter as a function of peak temperature for three typical values of vacancy formation energy.

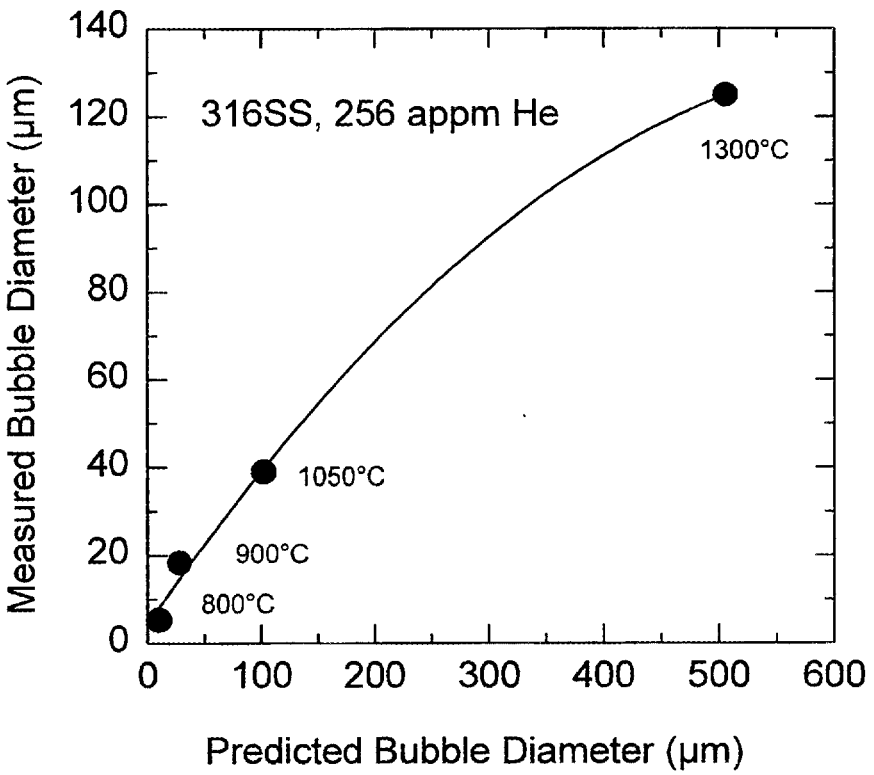

Figure 73. Relationship between results of aging experiment [19] and theoretical model of grain boundary bubble growth.

Failure occurs when grain boundary bubbles grow to a critical size, 1 μm as determined from experiments. Intergranular cracking at the HAZs was dominated by the stress-assisted grain boundary bubble growth during cooling of a weld where the combined effects of high temperature and shrinkage-induced tensile stress prevailed.

In the heat-affected zone location 0.5 mm, about 7 grains, away from the fusion boundary, the peak temperature during welding was measured to be 1092°C. Grain boundary bubbles grow with a much slower rate at this position during welding and never reach the critical size to cause cracking. Figure 74 shows the predicted results of grain boundary bubble growth at different location in the heat-affected zone, i.e., different peak temperatures, during welding. This result is consistent with observations that weld cracking always occurring in the HAZ about three grains distance from the fusion boundary.

Release of Helium during Welding

At the melting temperature, the agitation of the molten metal is believed to result in the observed porosity in the fusion zone. The entrapped helium bubbles in the molten steel will coalesce, grow and many will escape from the surface of the weld by buoyancy effect. The result from the gas mass spectrometry showed a 21% reduction of helium concentration in the fusion zone, indicating the release of

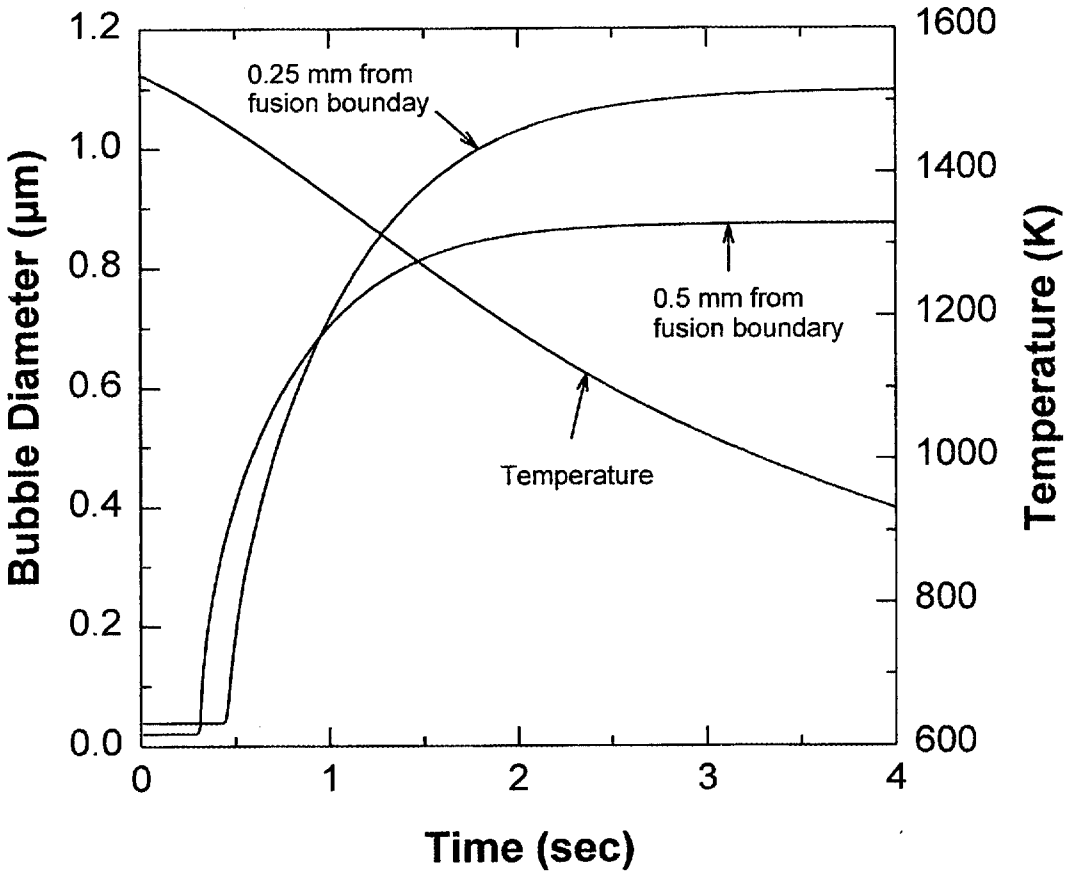

Figure 74. Predicted results of grain boundary bubble growth at different peak temperatures during welding.

He from welds during welding. The heat-affect zone retains essentially the same level of measured He concentration before and after welding as shown by measurements made in the current study. This phenomenon suggests that helium atoms are deeply entrapped in the solid metal. Even at the near-melting temperature, helium atoms were not able to escape from the heat-affected zone to the fusion boundary via thermal diffusion and hence could not escape through the molten metal surface.

Stress And Weld Cracking

Helium bubbles grow rapidly at interdendritic interfaces in the fusion zone and at grain boundaries in the heat-affected zone under the combined actions of high temperature and shrinkage tensile stress [16-20]. Rupture occurs as the cohesive strength of the grain boundaries, reduced by the growing bubbles, can no longer bear the shrinkage-induced tensile stress created during cooling of the weld. Since the near-melting temperature at the heat-affected zone is inevitable in the conventional fusion welding process, modifications of thermal stress become the logical choice to overcome the catastrophic failure.

The relation between helium concentration and total weld cracking of type 316 stainless steel, following the stress-modified GTA welding process is shown in Figure 59. The tendency toward severe weld cracking increased as the He

concentration increased. As the applied compressive stress increased in the modified welding process, the severe weld cracking decreased and totally disappeared at a compressive level of 165 MPa. The threshold helium concentration required to cause severe cracking in type 316 stainless steel using the conventional GTA welding process is shown to be 0.9 appm based upon experimental results in this study as shown in Figure 75.

Stress Direction and Bubble Growth

During weld solidification and cooling, the principal shrinkage-induced tensile stress is perpendicular to the welding direction. The stress level is enhanced by the lateral constraints as in the repair welding of large structural components. This stress causes the helium bubbles to grow rapidly at the grain boundaries at high temperatures, preferentially along grain boundaries aligned perpendicular to the stress (parallel to the weld). Since the shrinkage-induced tensile stress is reduced by applying an initial compressive stress perpendicular to the welding direction, the helium bubble growth process is retarded along grain boundaries parallel to the weld, therefore, heat-affected zone cracking is less likely to occur. However, a small number of grain boundary helium bubbles still grow preferentially along the direction perpendicular

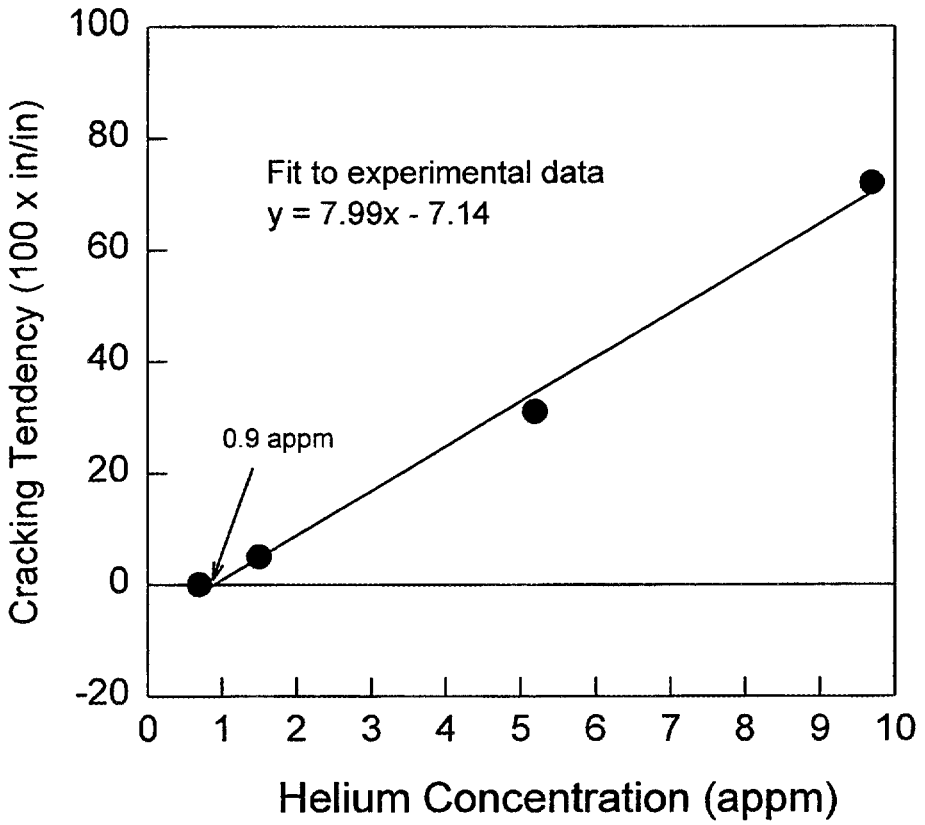

Figure 75. The threshold helium concentration required to cause severe cracking in type 316 stainless steel using a conventional GTA welding process was predicted to be 0.9 appm by the experimental data.

to the weld. This may be due to the internal tensile stresses generated by bulk body constraint of the steel along the weld direction during cooling or simply elastic deformation in response to the applied stress.

For type 316 stainless steel, grain boundary diffusivity is much higher than that in the matrix, therefore; the growth of helium bubbles at the grain boundary is much more sensitive to any changes in the stress. It has also reported that grain boundary sliding [126,127] can provide an additional driving force for the grain boundary bubble growth. Figure 76 shows evidence that grain boundaries are more favorable for helium bubble growth than the matrix.

It is a complex task to analyze the stress field around a bubble along a grain boundary. The simplified approaches taken in the current study, however, give a meaningful insight into the effects of an applied stress on the grain boundary helium bubble growth during welding.

The relation between grain boundary helium bubble densities and the angle between the welding direction and the grain boundary is given in Figure 59. Large variations were found by quantitative analyses of bubble size and density with respect to the stress direction since physical properties, such as crystal orientation, of each grain boundary vary. In some cases, bubble grow processes are relatively localized. Presence of subgrain microstructure

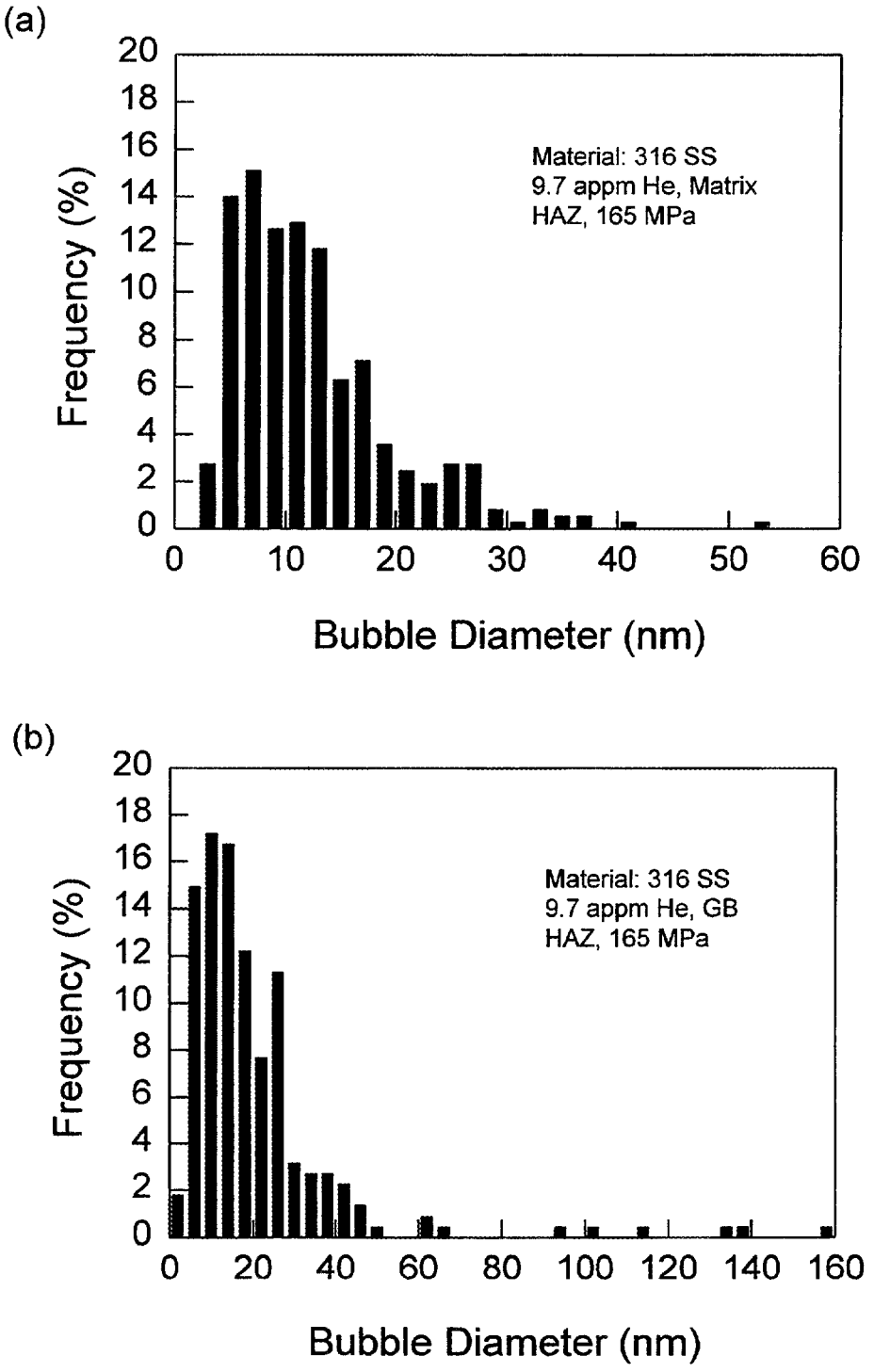

Figure 76. Distribution of bubble size in the matrix (a) and at grain boundaries (b) as determined by transmission electron microscopy.

will further distort any findings. One grain boundary may have large helium bubbles with low density, while another one has small bubbles but with very high bubble number density. Generally speaking, bubbles grow with tensile stress. The higher the stress the more they will grow.

Figure 77 shows the relationship between the resolved stress ratio and the actual bubble number ratio on the adjacent grain boundaries (within the same grain). In some cases, the grain boundaries do not have any bubbles so that the actual bubble number ratio becomes either zero or infinity as shown in Figure 77. When a grain boundary subjected to a resolved stress three times larger than the adjacent boundary, i.e., the resolved grain boundary stress ratio is greater than 3, it almost always has more helium bubbles than the other. This indicates that a minimum stress level three times higher than an adjacent boundaries is required to insure preferred grain boundary bubble growth.

Welding of Neutron Irradiated Materials

No other information is available for the welding properties of ORR irradiated materials. However, the results of welding of ORR irradiated materials are consistent with results of welding of tritium-charged materials. Type 316 stainless steel has the worst weld cracking resistance in both irradiated and tritiated

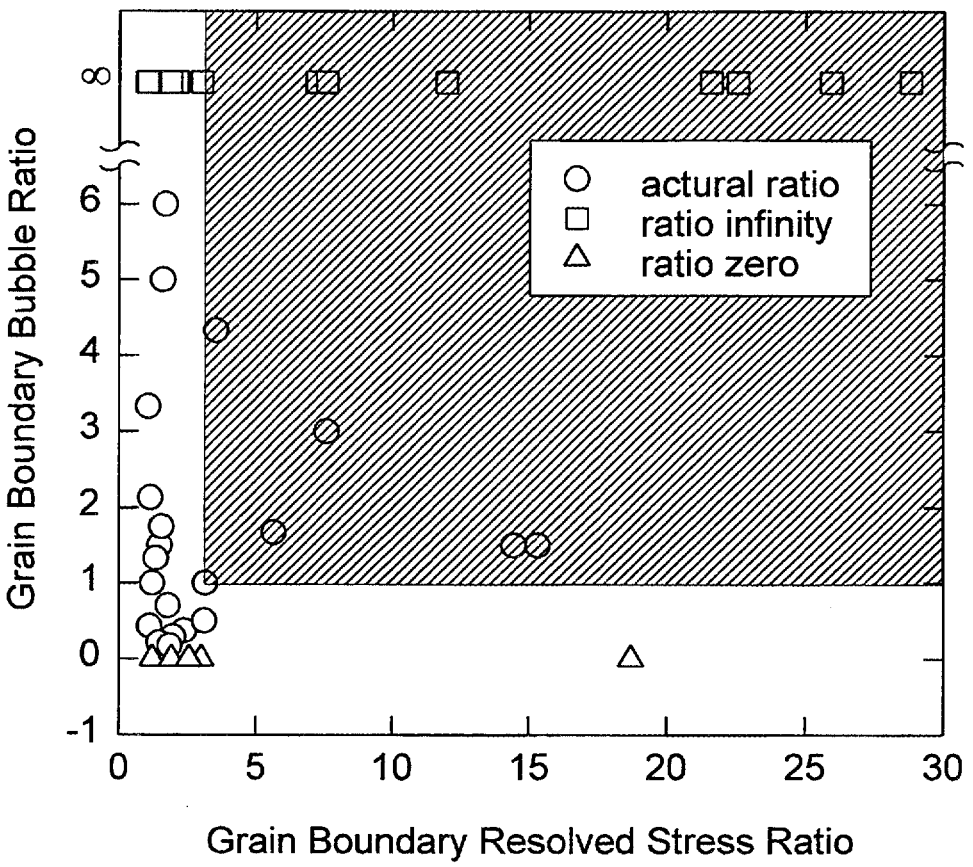

Figure 77. Relationship between the resolved stress ratio and actual bubble number ratio on the adjacent grain boundaries. Shaded area indicates preferred grain bounday bubble growth.

conditions. Results from welding irradiated PCA-B3 are somewhat unexpected. The formation of MC precipitates during thermal treatment prior to irradiation is expected to hinder void growth. However, MC precipitates were unstable, and were all dissolved after irradiation at 200°C in the ORR [128]. HT-9 steel exhibited the best resistance to helium induced cracking among these steels. However, HT-9 also had the lowest helium concentration.

Welding Techniques

The embrittlement effect of helium during welding was first suggested by Hall [7] in 1978. Helium embrittlement cracking during welding was not substantiated until 1988 when weld repair cracks in a Savannah River reactor tank were investigated [11] and further characterized by Lin et al. [16-20].

In addition to the stress-modified GTA welding technique used in the current study, a gas metal arc (GMA) overlay welding technique was developed [12,14,15,98] by other investigators. The technique minimizes the heat input at the base material while providing sufficient weld penetration, approximately 0.076 mm, to produce a bond between weld and base metal. Fusion zone and heat-affected zone cracking were observed in type 304 stainless steel, charged with up to 221 appm He, using the GMA weld overlay technique [98]. However, this technique showed a pronounced

reduction in cracking as compared to the repair welds of same steel in the reactor tank [13-15,98]. No external constraint was applied to the plates during overlay welding. Underbead cracking was also observed in the overlay welds and became significant at higher helium concentrations.

Similar results were observed in irradiated type 304 stainless steel with 5.0 to 10.4 appm He using GMA weld overlay technique reported by Kanne et al. [130]. No toe cracking was found while underbead cracking was observed in the HAZ. At several locations, underbead cracking extended into the fusion zone. Approximately twice the amount of underbead cracking was observed in irradiated steel with 10.4 appm He compared to the steel with 5.0 appm He.

Although the GMA overlay welding technique demonstrated an improvement in weld integrity, the stress-modified welding technique developed in the current study shows the most promising results for repair welding of helium containing materials. Studies [110] have shown that successful welds can be made by an application of compressive stress of 55 MPa during GTA welding of type 316 stainless steel containing 256 appm He. No cracking was found in the fusion and heat-affected zones.

Weld cracking decreased as applied compressive stress increased and was totally eliminated at 165 MPa for type 316 stainless steel. Results from tensile tests also showed similar strength between as-doped unwelded base materials

and stress modified welds as presented in Tables 17 and 18. This indicated that sound welds can be achieved using the stress modified welding technique for type 316 stainless steel containing helium concentrations up to 9.7 appm, while welds from GMA overlay welding showed a significant decrease in tensile strength [15].

Similar weld cracking susceptibility was observed for type 316 stainless steel, PCA-B3 and HT-9 in tritiated and ORR irradiated conditions. This result indicates that the nature of helium from tritium charging, ^{3}He, and neutron irradiation, ^{4}He, was similar, although quantitatively different, with respect to weld cracking in the current study. However, Kanne et al. [130] have found that the underbead cracking in irradiated type 304 stainless steel was considerably higher than that experienced in tritiated steel at the same He concentrations using either conventional or overlay welding techniques.

To minimize the extent of weld cracking in repair of helium containing materials, the following factors should be considered:

1. Materials:

HT-9 steel had the best resistance to helium induced weld cracking and type 316 stainless steel the worst. PCA-B3 showed moderate improvement over type 316 stainless steel. Cold-working can be used to improve weld integrity of materials by the introduction of extensive dislocation

networks. Dispersed carbide precipitates in the matrix can also significantly improve resistance to helium induced weld cracking.

2. Welding condition:

The higher the heat input, the higher the temperature and thermal stress gradients which increase weld cracking tendencies. Full penetration and a wider heat-affected zone welding processes are also considered unfavorable with respect to weld cracking.

3. Welding process:

Conventional fusion welding processes cause severe fusion and HAZ cracking. The GMA overlay welding process can reduce the level of weld cracking, but the stress-modified welding technique can eliminate weld cracking. Resistance welding [11] and solid state welding [129] may be viable techniques for joining material with entrapped helium.

VII. CONCLUSIONS

The following conclusions can be drawn from this study of welding helium-containing materials:

1. Severe fusion zone and heat-affected-zone cracking during welding of helium-containing type 316 stainless steel and PCA alloy is caused by helium bubble growth along interdendritic interfaces and grain boundaries.
2. No Cracking was found in welding HT-9 steel with helium concentrations up to 2.5 appm using the conventional GTA welding. Type 316 stainless steel had the worst weld cracking resistance among materials tested in this study.
3. Grain boundary helium bubble growth is enhanced by the shrinkage-induced tensile stress generated during the welding process; high temperature alone is insufficient to cause cracking.
4. No apparent change of strength was observed in steels doped with helium in type 316 stainless steel, PCA-B3 and HT-9. However, the presence of helium decreased the weld ductility due to grain boundary bubble growth.
5. The threshold helium concentration required to cause severe heat-affected zone cracking using GTA welding was

predicted to be 0.9 appm for type 316 stainless steel based on helium doped material experiments.

6. Catastrophic weld cracking can be eliminated in helium-containing materials by the application of a compressive stress during welding to alter grain boundary bubble growth kinetics.

7. A 55 MPa compressive stress was found to eliminate weld cracking in PCA with up to 11.4 appm charged helium.

8. Helium bubbles located at grain boundaries parallel to the applied compressive stress are favored to grow due to bulk plate constraints with respect to those at grain boundaries parallel to the weld.

9. Severe fusion zone cracking was observed in 316SS, 20% cold-worked and PCA-B3 irradiated at 200°C in the ORR. Cracking was eliminated using the stress-modified welding technique.

The results of this study indicate that the stress-modified welding technique can effectively suppress the grain boundary helium bubble growth and can be applied to eliminate the severe HAZ cracking which occurs during GTA repair welding of irradiated materials.

REFERENCES

1. R. Buende, S. Fabritsiev and V. Rybin, "Reliability of Welds and Brazed Joints in Blankets and its Influence on Available," Fusion Engineering and Design, 16(1991)59-72.

2. M. V. Speight and J. E. Harris, "The Kinetics of Stress-Induced Growth of Grain-Boundary Voids," Metal Science Journal, Vol.1, 1967, pp.83-85.

3. G. W. Greenwood and M. V. Speight, "An Analysis of the Diffusion of Fissile Gas Bubbles and its Effect on the Behaviour of Reactor Fuels," Journal of Nuclear Materials, 10(1963)140-144.

4. H. Trinkaus, "Stress Induced Drift Diffusion in Grain Boundaries - Application to Creep and to the Growth of Grain boundary Voids." Berichte der Bundes Gesellschaft fur Physikalische Chemie, 82(1978)249-253.

5. R. S. Barnes, "Embrittlement of Stainless Steel and Nickel-Based Alloys at High Temperature Induced by Neutron Irradiation," Nature, 206(1965)1307-1310.

6. J. P. Maloney, D. Baker, W. A. Day, W. G. Fraser, H. R. Huxford, K. E. Kehr, W. R. Kennedy, J. B. McClain, D. H. McKenney, C. A. Meyer, R. F. Mittelberg and J. E. Walls, "Repair of a Nuclear Reactor Vessel", DP-1199, E. I. du Pont de Nemours & Co., Savannah River Laboratory, Aiken, SC, June 1969.

7. M. M. Hall, Jr., A. G. Hins, J. R. Summers,and D. E. Walker, "Fusion Welding of Irradiated AISI 304L Stainless Steel Tubing", Weldment: Physical Metallurgy and Failure Phenomena, Proceedings of the Fifth Bolton Landing Conference, August 1978, pp. 365-378.

8. W. K. Kanne, C. L. Angerman and B. J. Eberhard, "Weldability of Tritium-Charged 304L Stainless Steel", DP-1740, E. I. du Pont de Nemours & Co., Savannah River Laboratory, Aiken, SC, February 1987.

9. W. R. Kanne, "Helium Embrittlement Cracking During Patch Welding in Savannah River C reactor," DPMS-8940, E. I. Dupont Co., Savannah River Laboratory, Aiken, SC, 1989.

10. A. K. Birchenall, "Helium Induced Weld Cracking in Irradiated 304 Stainless Steel," DPMS-8941, E. I. Dupont Co., Savannah River Laboratory, Aiken, SC, 1989.

11. W. R. Kanne, Jr., "Remote Reactor Repair: GTA Weld Cracking Caused by Entrapped Helium," Welding Journal, 67(8)1988, pp. 33-39.

12. W. R. Kanne, Jr., D. A. Lohmeier, K. A. Dunn and M. H. Tosten, "Metallographic Analysis of Helium Embrittlement Cracking of Repair Welds in Nuclear Reactor Tanks," WSRC-MS-90-1351, Rev.1, Westinghouse Savannah River Company, Savannah River Laboratory, Aiken, SC, 1991.

13. E. A. Franco-Ferreira and W. R. Kanne, Jr., "Remote Reactor Repair: Avoidance of He-Induced Cracking with GMAW," Abstract of Papers, American Welding Society 71st Annual Meeting, April 1990, pp. 20-22.

14. W. R. Kanne, Jr., E. A. Franco-Ferreira, M. R. Louthan, Jr. and M. H. Tosten, "Weld Repair of Austenitic Stainless Steels Containing Helium," Abstract of Papers, American Welding Society 72nd Annual Meeting, April 1991, pp. 157-158.

15. W. R. Kanne, Jr., D. A. Lohmeier, M. R. Louthan, Jr., D. T. Rankin, E. A. Franco-Ferreira, G. J. Bruck, A. Madeyski, R. P. Shogan and G. G. Lessmann, "Weld Repair of Helium Degraded Reactor Vessel Material", Proceedings of the Fifth International Symposium on Environmental Degradation of Materials in Nuclear Power System - Water Reactors, August 25-29, 1991, Monterey, CA, pp. 390-402, American Nuclear Society.

16. H. T. Lin, M. L. Grossbeck and B. A. Chin, "Cavity Microstructure and Kinetics During Gas Tungsten Arc Welding of Helium Containing Stainless Steel," Metallurgical Transactions A, V21A, September 1990, pp. 2585-2596.

17. H. T. Lin and B. A. Chin, "The Feasibility of Welding Irradiated Materials," Journal of Nuclear Materials, 179(1991)1131-1134.

18. H. T. Lin, S. H. Goods, M. L. Grossbeck, and B. A. Chin, "Helium-Induced Degradation in the Weldability of an Austenitic Stainless Steel", Effect of Radiation on Materials, 14th International Symposium, Volume I, ASTM STP 1046, N. H. Packan, R. E. Stoller, and A. S. Kumar, Eds., American Society for Testing and Materials, Philadelphia, 1989, pp. 301-314.

19. H. T. Lin, "Simulation of the Welding of Irradiated Materials", ORNL/TM-11158, Oak Ridge National Laboratory, Oak Ridge, TN, 1989.

20. H. T. Lin and B. A. Chin, "Helium-Induced Weld Cracking in Austenitic and Martensitic Steels," Journal of Materials Science, 26(1991)2063-2069.

21. M. Ma Benjamin, Nuclear Reactor Materials and Applications, Van Nostrand Reinhold Company, New York, 1983.

22. Robert A. Gross, Fusion Energy, John Wiley & Sons, Inc., 1984. pp. 13-15.

23. Kenneth Evans, Jr. et al., "Wildcat: A Commercial Deuterium-Deuterium Tokamak Reactor", Nuclear Technology/Fusion, Vol. 4, No. 2, Part 1, Sep. 1983, pp.226-236.

24. H. Ullmaier, "The Influence of Helium in the Bulk Properties of Fusion Reactor Structural Materials", Nuclear Fusion, Vol.24, No. 8, 1984, pp.1039-1083.

25. J. J. Harwood et al., Effects of Radiation on Materials, Reinhold Publishing Corporation, New York, 1958.

26. H. Ullmaier, "Helium in Metals", Radiation Effect, 78 (1983), 1-10.

27. R. B. McLellan, "Solution Thermodynamics," Treatise on Materials Science and Technology, H. Herman Ed., Vol 5, pp. 1-43.

28. W. D. Wilson, M. I. Baskes and C. L. Bisson, "Atomistic of Helium Bubble Formation in a Face-Centered-Cubic Metal," Physical Review B, 13(1976), pp. 2470-2478.

29. C. L. Bisson and W. D. Wilson, "Atomistic of Tritium and Helium-3 in Metal," Proceedings of Tritium Technology in Fission, Fusion and Isotopic Applications, Dayton, Ohio, 1980, pp.78-84.

30. W. D. Wilson , C. L. Bisson and M. I. Baskes, "Self-Trapping of Helium in Metals," Physical Review B, 24(1981), pp.5616-5624.

31. W. D. Wilson, "Theory of Small Clusters of Helium in Metals," Radiation Effects, 78(1983), pp. 11-24.

32. G. W. Greenwood, A. J. E. Foreman and D. E. Rimmer, "The Role of Vacancies and Dislocations in the Nucleation and Growth of Gas Bubbles in Irradiated Fissile Materials," Journal of Nuclear Materials, 4(1959)305-324.

33. J. H, Evans, A. V. Veen and L. M. Caspers, "Direct Evidence for Helium Bubble Growth in Molybdenum by the Mechanism of Loop Punching," Scripta Metallurgica, Vol. 15, 1981, pp. 323-326.

34. G. J. Thomas and R. Bastasz, "Direct Evidence for Spontaneous Precipitation of Helium in Metals," Journal of Applied Physics, 52(1981), pp.6426-6428.

35. W. Jager, R. Lasser, T. Schober and G. J. Thomas, "Formation of Helium Bubbles and Dislocation Loop in Tritium-Charged Vanadium," Radiation Effects, 78(1983),pp. 165-176.

36. E. E. Gruber, "Calculated Size Distributions for Gas Bubble Migration and Coalescence in Solids," Journal of Applied Physics, Vol. 38, No. 12, 1967, pp.243-250.

37. G. W. Greenwood and M. V. Speight, "An Analysis of the Diffusion of Fissile Gas Bubbles and its Effect on the Behaviour of Reactor Fuels," Journal of Nuclear Materials, 10(1963)140-144.

38. R. S. Barnes, "A theory of Swelling and Gas Release for Reactor Materials," Journal of Nuclear Materials, 11(1964)135-148.

39. S. K. Tyler and P. J. Goodhew, "Direct Evidence for the Brownian Motion of Helium Bubbles," Journal of Nuclear Materials, 92(1980), pp. 210-206.

40. H. Trinkaus and H. Ullmaier, "High Temperature Embrittlement of Metals due to Helium: Is the Lifetime Dominated by Cavity Growth or Crack Growth" ? Journal of Nuclear Materials, 212-215(1994), pp. 303-309.

41. D. N. Braski, H. Schroeder and H. Ullmaier, "The Effect of Tensile Stress on the Growth of Helium Bubbles in an Austenitic Stainless Steel," Journal of Nuclear Materials, 83(1979), pp. 265-277.

42. J. Rothaut, H. Schroeder and H. Ullmaier, "The Growth of Helium Bubbles is Stainless Steel at High Temperatures," Philosophical Magazine, 1983, Vol. 47, NO. 5, pp. 781-795.

43. G. W. Greenwood and A. Boltax, "The Role of Fission Gas Re-solution during Post-Irradiation Heat Treatment," Journal of Nuclear Materials, 5(1962)234-240.

44. A. J. Markworth, "On the Coarsening of Gas-Filled Pores in Solids," Metallurgical Transactions, Vol.4, Nov. 1973, pp. 2651-2656.

45. S. K. Khera, C. Schwaiger and H. Ullmaier, "The Influence of Stress on the Early Stage of Void Formation in a Model Stainless Steel," Journal of Nuclear Materials, 92(1980), pp. 299-305.

46. D. Hull and D. E. Rimmer, "The Growth of Grain-Boundary Voids Under Stress," Philosophical Magazine, 4(1959)673-687.

47. B. L. Eyre and R. Bullough, "The Formation and Behaviour of Gas Bubbles in a Non-uniform Temperature Environment," Journal of Nuclear Materials, 26(1968)249-266.

48. D. G. Martin, "The Migration of Equilibrium Gas Bubbles in a Solid Subject to a Stress Gradient," Journal of Nuclear Materials, 33(1969)23-29.

49. G. W. Greenwood, "The Growth of Inert Gas Bubbles within Grains and at Grain Boundaries - A Comparison of Mechanisms," Radiation Effects, Vol. 53, 1980, pp. 203-208.

50. R. Raj and M. F. Ashby, "Intergranular Fracture at Elevated Temperature," ACTA Metallurgica, Vol. 23, pp. 653-666, June 1975.

51. J. Weertman, "Hull-Rimmer Grain Boundary Void Growth Theory - A Correction," Scripta Metallurgica, Vol. 7, 1973, pp. 1129-1130.

52. M. V. Speight and J. E. Harris, "The Kinetics of Stress-Induced Growth of Grain-Boundary Voids," Metal Science Journal, Vol.1, 1967, pp.83-85.

53. M. V. Speight and W. Beeré, "Vacancy Potential and Void Growth on Grain Boundaries," Metal Science Journal, Vol. 9, 1975, pp.190-191.

54. K. Masubuchi, Analysis of Welded Structures, Pergamon Press, New York, 1980, pp. 148-149.

55. D. R. Harries, "Neutron Irradiation-Induced Embrittlement in Type 316 and other Austenitic Steels and Alloys," Journal of Nuclear Materials, 82(1979), pp. 2-21.

56. K. Sonnenberg, G. Antesberger and B. Brown, "Influence of He Implantation on the Fatigue Properties of Stainless Steel under Different Atmospheric Conditions," Journal of Nuclear Materials, 102(1981), pp. 333-345.

57. I. S. Batra, H. Ullmaier and K. Sonnenberg, "Frequency Dependence of the High Temperature Fatigue Properties of He-Implanted Stainless Steel," Journal of Nuclear Materials, 116(1983), pp. 136-140.

58. K. Sonnenberg and H. Ullmaier, "Fatigue Properties of Type 316 Stainless Steel under Helium and Hydrogen Bombardment," Journal of Nuclear Materials, 103&104(1981), pp. 859-864.

59. R. L. Klueh and J. M. Vitek, "Postirradiation Tensile Behavior of Nickel-Doped Ferritic Steels," Journal of Nuclear Materials, 150(1987), pp. 272-280.

60. J. M. Vitek, W. R. Corwin, R. L. Klueh and J. R. Hawthorne, "On the Saturation of the DBTT Shift of Irradiated 12Cr-1MoVW with Increasing Fluence," Journal of Nuclear Materials, 141-143(1986), pp. 948-953.

61. M. L. Grossbeck, J. M. Vitek and K. C. Liu, "Fatigue Behavior of Irradiated Helium-Containing Ferritic Steels for Fusion Reactor Applications," Journal of Nuclear Materials, 141-143(1986), pp. 966-972.

62. S. S. Vagaradi and G. R. Odette, "A Creep Fracture Model for Irradiated and Helium Injected Austenitic Stainless Steels," Journal of Nuclear Materials, 103&104(1981), pp. 1239-1244.

63. E. E. Bloom and F. W. Wiffen, "Mechanical Properties of Materials in Fusion Reactor First-Wall and Blanket System", Journal of Nuclear Materials, 85&86(1979), pp. 795-804.

64. F. A. Garner and R. J. Puigh, "Irradiation Creep and Swelling of the Fusion Heats of PCA, HT9 and 9Cr-1Mo Irradiated to High Neutron Fluence," Journal of Nuclear Materials, 179-181(1991), pp. 577-580.

65. A. F. Rowcliffe and M. L. Grossbeck, "The Response of Austenitic Steels to Radiation Damage," Journal of Nuclear Materials, 122&123(1984), pp. 181-190.

66. E. A. Little and D. A. Stow, "Void-Swelling in Iron and Ferritic Steels," Journal of Nuclear Materials, 87(1979), pp. 25-39.

67. R. L. Klueh and J. M. Vitek, "The Resistance of 9Cr-1MoVNb and 12Cr-1MoVW Steels to Helium Embrittlement," Journal of Nuclear Materials, 117(1983), pp. 295-302.

68. E. E. Bloom, J. M. Leitnaker and J. O. Steigler, "Effect of Neutron Irradiation on the Microstructure and Properties of Titanium-Stabilized Type 316 Stainless Steels," Nuclear Technology, 31(1976), pp. 232-243.

69. P. J. Maziasz, R. L. Klueh and J. M. Vitek, "Helium Effect on Void Formation in 9Cr-1MoVNb and 12Cr-1MoVW Irradiated in HIFR," Journal of Nuclear Materials, 141-143(1984), pp. 929-937.

70. M. L. Grossbeck and K. C. Liu, "High-Temperature Fatigue Life of Type 316 Stainless Steel Containing Irradiation Induced Helium," Journal of Nuclear Materials, 103&104(1981), pp. 853-858

71. K. Q. Chen, Y. S. Wang, J. M. Quan, J. G. Sun, C. H. Zhang and Z. Y. Zhao, "The Formation of Helium Bubbles in 316L SS Irradiated with Helium Ions at Different Temperatures," Journal of Nuclear Materials, 212-215(1994), pp. 345-351.

72. T. A. Kenfield, W. K. Appleby, H. J. Busboom and W. L. Bell, "Swelling of Type 316 Stainless Steel at High Fluence in EBR-II," Journal of Nuclear Materials, 75(1978), pp. 85-97.

73. R. G. Faulkner and K. Anderko, "High Temperature Ductility of Irradiated Ferritic and Austenitic Steels," Journal of Nuclear Materials, 113(1983), pp. 168-171.

74. D. Kramer, K. R. Garr, C. G. Rhodes and A. G. Pard, "Helium Embrittlement of Type 316 Stainless Steel," Journal of The Iron and Steel Institute, August 1969, pp. 1141-1146.

75. D. Kramer, H. R. Brager, C. G. Rhodes and A. G. Pard, "Helium Embrittlement in Type 304 Stainless Steel," Journal of Nuclear Materials, 25(1968)121-131.

76. R. S. Barnes, "Embrittlement of Stainless Steel and Nickel-Based Alloys at High Temperature Induced by Neutron Irradiation," Nature, 206(1965)1307-1310.

77. H. Schroeder and U. Stamm, "High Temperature Helium Embrittlement: Austenitic Versus Martensitic Stainless Steels," ibid. ref[18], pp. 223-245.

78. A. J. Lovell, "Postirradiation Creep of Annealed Type 316 Stainless Steel," Nuclear Technology, 16, 1972, pp. 323-331.

79. E. E. Bloom and J. O. Stiegler, "Effect of Irradiation on the Microstructure and Creep-Rupture Properties of Type 316 Stainless Steel," Effects of Radiation on Substructure and Mechanical Properties of Metals and Alloys, ASTM STP 529, 1973, pp. 360-380.

80. M. L. Grossbeck and P. J. Maziasz, " Tensile Properties of 20% Cold-Worked Titanium-Modified Type 316 Stainless Steel Irradiated in HFIR," Journal of Nuclear Materials, 104(1981)827-832.

81. I. Shibahara, S. Ukai, S. Onose and S. Shikakura, "Irradiation Performance of Modified 316 Stainless Steel for Monju Fuel," Journal of Nuclear Materials, 204(1993), pp. 131-140.

82. D. J. Mazey, D. R. Harries and J. A. Hudson, "The Effects of Silicon and Titanium on Void Swelling and Phase Stability in 12Cr-15Ni Austenitic Alloys Irradiated with 46 MeV Nickel Ions," Journal of Nuclear Materials, 89(1980), pp. 155-181.

83. P. J. Maziasz and D. N. Braski, "Modification of the Grain Boundary Microstructure of the Austenitic PCA Stainless Steel to Improve Helium Embrittlement Resistance," Journal of Nuclear Materials, 141-143(1986), 973-977.

84. M. Suzuki, S. Hamada, P. J. Maziasz, M. P. Tanaka and A. Hishinuma, "Microstructural Development of Titanium-Modified Austenitic Stainless Steel under Neutron Irradiation in HFIR up to 57 dpa," ibid. ref. [18], pp. 160-171.

85. P. J. Maziasz and E. E. Bloom, "Comparison of 316 + Ti with 316 Stainless Steel Irradiated in a simulated Fusion Environment", Transactions of the American Nuclear Society, 27(1977), pp. 268-269.

86. P. J. Maziasz and D. N. Braski, "Grain Boundary Microstructural Development and Stability for Various Pretreatments of Path A Prime Candidate Alloy Irradiated in HFIR", ADIP Semiannu. Prog. Rep., march 31, 1983, DOE/ER-0045/10, pp. 39-48, U. S. DOE, Office of Fusion Energy.

87. J. Megusar, "Swelling Resistance of the Highly Deformed Titanium-Modified Austenitic Stainless Steel," ibid. ref. [18], pp. 185-192.

88. H. Kawanishi, M. Yamada, K. Fukuya and S. Ishino, "Effect of Titanium on Microstructural Changes in SUS 316 stainless Steels," Journal of Nuclear Materials, 103&104(1981), pp. 1097-1102.

89. W. Kesternich, M. K. Matta and J. Rothaut, "Influence of TiC Precipitation in Austenitic Stainless Steel on Strength, Ductility and Helium Embrittlement," Journal of Nuclear Materials, 122&123(1984), pp. 130-133.

90. P. J. Maziasz and D. N. Braski, "Microstructural Design of PCA Austenitic Stainless Steel for Improved Resistance to Helium Embrittlement under HIFR Irradiation," Journal of Nuclear Materials, 122&123(1984), pp. 305-310.

91. M. Fujiwara, H. Uchida, S. Ohda, S. Yuhara, S. Tani and Y. Sato, "Development of Modified Type 316 Stainless Steel for Fast Breeder Reactor Fuel Cladding Tubes," Effects of Radiation on Materials, 13th International Symposium, ASTM STP 955, F. A. Garner, N. H. Packan, and A. S. Kumar, Eds., American Society for Testing and Materials, Philadelphia,1987, pp. 127-145.

92. H. R. Brager and F. A. Garner, "The Influence of Cold Work Level, Solute, and Helium Content on the Swelling of 'Pure' AISI 316 (Fe-17Cr-16.7Ni-2.5Mo)," Effects of Radiation on Materials, 11th International Symposium, ASTM STP 782, H. R. Grager and J. S. Perrin, Eds., American Society for Testing and Materials, Philadelphia, 1982, pp. 152-165.

93. G. R. Caskey, Jr., "Tritium-Helium Effects in Metals," Fusion Technology, Vol 8, September 1985, pp. 2293-2298.

94. S. D. Atkin, "Weld Bend Tests on Irradiated, 20% Cold-Work 316 Stainless Steel", ADIP Semiannu. Prog. Rep., Sept. 30, 1981, DOE/ER-0045/7, pp. 110-117, U.S. DOE, Office of Fusion Energy.

95. S. Hamada, K. Watanabe, A. Hishinuma and I. Takahashi and T. Kikuchi, "Microstructures of a Welded Joint using an Irradiated Wrapper Tube," ADIP Semiannu. Prog. Rep., March 31, 1993, DOE/ER-0313/14, pp. 241-250, U.S. DOE, Office of Fusion Energy.

96. H. T. Lin and D. N. Braski, "Degradation in the Weldability of a Helium-Containing Vanadium Alloy," Journal of Nuclear Materials, 217(1994), pp. 209-212.

97. S. L. Robinson, "Tensile Properties of Welded Helium Charged 304L Stainless Steel," Journal of Nuclear Materials, 152(1988), pp. 212-219.

98. S. H. Goods and C. W. Karfs, "Helium-Induced Weld cracking in Low Heat Input GMA Weld Overlays," Welding Journal, Vol. 70, No. 5, 1991, pp. 123-132.

99. J. M. Mintz, Kinetics of Stress-Induced Cavity Growth in FCC Metals at Elevated Temperatures, Doctoral Dissertation, University of California, Davis, 1986.

100. D. W. Ramey and D. N. Braski, "Procedures for a Modified Tritium Trick - Helium Doping and Residual Tritium Analysis of Vanadium Alloys," Nuclear Instruments and Methods in Physics Research, B10/11(1985), pp. 976-980.

101. S. H. Goods, "Cavitation and Embrittlement in Tritium Exposed Copper," ibid. ref. [18], pp. 340-352.

102. "Standard Guide for Simulation of Helium Effects in Irradiated Metals," E 942-89, Annual Book of ASTM Standards, Volume 12.02, 1989, pp. 1-11.

103. H. Farrar IV and B. M. Oliver, "A Mass Spectrometer System to Determine Very Low Levels of Helium in Small Solid and Liquid Samples," Journal of Vacuum Science & Technology, A4(1986), pp. 1740-1741.

104. B. M. Oliver, J. G. Bradley and H. Farrar IV, "Helium Concentration in the Earth's Lower Atmosphere," Geochimica et Cosmochimica Acta, 48(1984), pp. 1759-1767.

105. "Standard Practice for Neutron Radiation Damage Simulation by Charged-Particle Irradiation," E 521-89, Annual Book of ASTM Standards, Volume 12.02, 1989, pp. 1-19.

106. J. F. Nankivell, "Stereoscopic Viewing of Metal Foils in the Electron Microscope," British Journal of Applied Physics, 13(1962), p. 129-130.

107. J.F. Nankivell, "The Theory of Electron Stereo Microscopy," Optik, 20, 1963, pp. 171-198

108. P. B. Hirsch, A. Howie, R. B. Nicholson, D. W. Pashley and M. J. Whelan, Electron Microscopy of Thin Crystals, Butterworth Inc., Washington, 1965, pp. 418-420.

109. P. J. Maziasz,"Swelling and Swelling Resistance Possibility of Austenitic Stainless Steels in Fusion Reactor," Journal of Nuclear Materials, 122&123(1985)472-486

110. C. A. Wang, H. T. Lin, M. L. Grossbeck and B. A. Chin, "Suppression of HAZ Cracking during Welding of Helium-Containing Materials," Journal of Nuclear Materials, 191-194(1992)696-700.

111. L. R. Greenwood and D. V. Steidl, "Neutron Dosimetry and Damage Calculations for the ORR-MFE6J Experiment," DOE/ER-0313/8, pp. 34-39.

112. J. Crank, The Mathematics of Diffusion, Clarendon Press, Oxford, 1975, p.69.

113. D. W. James and G. M. Leak, "Grain Boundary Diffusion of Iron, Cobalt and Nickel in Alpha-Iron and Iron in Gamma-Iron," Philosophical Magazine, 12(1962), pp. 491-503.

114. W. G. Wolfer and B. B. Glasgow, "Growth Mechanisms for Helium Inclusions and Bubbles," Damage Analysis and Foundmental Studies, DOE/ER-0046/12, pp. 155-169, U. S. DOE, Office of Fusion Energy.

115. E. M. Baroody, "Calculations on the Collisional Coalescence of Gas Bubbles on Solids," Journal of Applied Physics, Vol. 38, NO. 12, 1967, pp.4893-4903.

116. P. G. Shewmon, "The Movement of Small Inclusions in Solids by a Temperature Gradient," Transaction of the Metallurgical Society of AIME, Vol. 230, 1964, pp. 1134-1137.

117. R. S. Barnes and D. J. Mazey, "The Migration and Coalescence of Inert Gas Bubbles in Metals," Proceedings of Royal Society, 1963, Vol.275A, pp. 47-57.

118. T. Z. Chuang and J. R. Rice, "The Shape of Intergranular Creep Cracks Growing by Surface Diffusion," Acta Metallurgica, Vol. 21, 1973, pp.1625-1628.

119. T. Z. Chuang et al., "Non-equilibrium Models for Diffusion Cavitation of Grain Interfaces," Acta Metallurgica, Vol. 27, 1979, pp.265-284.

120. G. Neumann and G. M. Neumann, Surface Self-Diffusion of Metal, Diffusion Information Center, Ohio, 1972.

121. F. Dobeš and J. Čadek, "On the Kinetics of Stress Induced Growth of Grain Boundary Voids", Scripta Metallurgica, Vol. 4, 1970, pp. 1005-1008.

122. B. T. M. Loh, "Stress Concentration and Cavity Growth", ibid. ref. [155], pp. 299-304.

123. C. Herring, "Diffusional Viscosity of a Polycrystalline Solid," Journal of Applied Physics, Vol. 21, 1950, pp. 437-445.

124. Nuclear Systems Materials Handbook, Vol. 1, Design Data, Part I - Sturctural Materials, Group 1 - High Alloy Steels, Section 4 - 316 SS, annealed.

125. L. E. Murr, G. I. Womg and R. J. Horylev, "Measurement of Interfacial Free Energies and Associated Temperature Coeffcients in 304 Stainless Steel," Acta Metallurgica, Vol. 21, May 1973, pp. 595-604.

126. I. W. Chen, "Cavity Growth on a Sliding Grain Boundary," Metallurgical Transactions, 14A, 1983, pp. 2289-2293.

127. I. W. Chen and A. S. Argon, "Grain Boundary and Interphase Boundary Sliding in Power Law Creep," Acta Metallurgica, Vol. 27, 1979, pp. 749-754.

128. P. J. Maziasz, "Temperature Dependence of the Dislocation Microstructure of PCA Austenitic Stainless Steel Irradiated in ORR Spectrally-Tailored Experiments," Journal of Nuclear Materials, 191-194(1992)701-705.

129. D. E. Clark, C. J. Einerson and R. B. Loop, "Weldability of Rapidly Solidified Type 304 Stainless Steel," Advances in Welding Science and Technology, S. A. David, Ed., 1986, pp. 817-820.

130. W. R. Kanne, Jr., G. T. Chandler, D. Z. Nelson and E. A. Franco-Ferreira, "Welding Irradiated Stainless Steel," Journal of Nuclear Materials, 225(1995)69-75.

Appendix

Data Acquisition for K-type Thermocouple

This appendix details the computer program to retrive the K-type thermocouple voltage output from an ocilliscope memory and convert into temperatures as a function of time in the HAZ during welding. This program is written using Microsoft QuickBasic, version 4.5.

```
DECLARE SUB herc.hp ()
DECLARE SUB Viewport (Xmim!, Xmax!, Ymim!, Ymax!, Tmim,
Tmax!)
'******************  OSCISCOP.BAS  *******************
'
'A. This program receives single waveform data (time vs.
'   voltage) stored in Nicolet 3091 Oscilloscope via RS232C
'   port located at the rear panel of Nicolet 3091 using a
'   null modem.
'
'   Important:  No "save" should be selected on the data
'               channel.  Data$ string is valid but handling
'               differently.
'
'B. Data$ string contains totally 20051 characters (single
'   waveform and no "save" is selected):
'
'   5 identifer + 2 delimiter(CR/LF) + 5 * 4000 data point +
'   2 delimiter + 40 normalization string + 2 delimiter
'
'C. If "save" is selected, Data$ will be 20095 characters,
'   no matter either single or double waveform.
'   Use "AUTO CENTER" to select current and saved data:
'
'   5 identifer + 2 delimiter(CR/LF) + 5 * 2000 current data
'   + 2 delimiter + 40 normalization string + 2 delimiter +
'   5 * 2000 saved data + 2 delimiter + 40 normalization
'   string + 2 delimiter
'
'D. Program output may include:
'   Time(sec), Voltage(volt), Temperature(C) and a graphical
'   screen dump of Time vs. both Voltage and Temperature
'
'E. This program assumes K-type theomocouple is used and the
'   temperature is converted from voltage using polynomial
'   constants (a) as listed in program.  When different type
```

```
'   of thermocouple is used, only Time and Voltage will be
'   valid, and temperature need to be converted otherwise.
'   Refer to manual or catalog for temperature convertion.
'
'F. For the temperature measurement using thermocouple:
'
'   a.  set "AUTO CENTER" to ON
'   b.  set to "ROLL"
'   c.  set "HORIZONTAL" and "VERTICAL" to OFF
'   d.  set channel to ON (see above for "save" option)
'   e.  set "VOLTS FULL SCALE" to 100mV
'   f.  set all switches to DC
'   g.  set "TRIGGER" to AUTO
'   h.  set "TIME PER POINT" the double of measuring time
'   i.  set origin at far left center (use DATA REMOVE &
'       RESET)
'   j.  zeroing DC OFFSET (Ready to go!)
'   k.  press "LIVE" to sweep and "STORE" to save in memory
'   l.  start program to retrieve and convert data from
'       memory
'
'*************************************************************

CLS
OPEN "com1:9600,n,8,1" FOR RANDOM AS #1    'change baud rate
                                           'as necessary

    INPUT "Do you want to save data to a disk file ? ", ans$
    IF UCASE$(ans$) = "y" THEN
        INPUT "Enter file path and name for output: ", File$
        OPEN File$ FOR OUTPUT AS #2 'diskfile for output
    END IF

DIM V(4000), T(4000) '4000 data for each channel
'REM $DYNAMIC

'  The following constants are used to convert voltage to
'  temperature valid "only" for K-type thermocouple from 0
'  to 1370 C.

        CONST a0 = .226584602#
        CONST a1 = 24152.109#
        CONST a2 = 67233.42479999999#
        CONST a3 = 2210340.682#
        CONST a4 = -860963914.9#
        CONST a5 = 4.83506E+10
        CONST a6 = -1.18452E+12
        CONST a7 = 1.3869E+13
        CONST a8 = -6.33708E+13

PRINT "press Nicolet 3091 RS-232 buttom "
```

```
DATA$ = ""   'initialize data string

WHILE EOF(1)
WEND

DO
    I$ = INPUT$(LOC(1), #1)
    PRINT I$;
    DATA$ = DATA$ + I$
        Start! = TIMER
    DO
        IF NOT EOF(1) THEN EXIT DO
        delay! = TIMER
    LOOP UNTIL delay! - Start! > 1       'one second for data
                                         'detection
LOOP UNTIL EOF(1)

'Horizontal trigger point H0, stored in 16-20th characters
'in normalization string--> 20025-20029th in DATA$
'H0 = VAL(MID$(DATA$, 20025, 5))

V1 = (VAL(MID$(DATA$, 20030, 5)) - 5) * 10 ^
(VAL(MID$(DATA$, 20035, 5)) - 12)
H1 = (VAL(MID$(DATA$, 20040, 5)) - 5) * 10 ^
(VAL(MID$(DATA$, 20045, 5)) - 12)

    Xmim = 0!            'Time origin
    Xmax = 4000 * H1     'total time sweep for 4000
                         'data point
    Ymax = .1             'voltage full scale
    Ymim = -Ymax
    Tmim = 0
    Tmax = 1400          'Maximum temperature scale
    Factor = (Tmax - Tmim) / (Ymax - Ymim)    'Graphic factor
                                              'for Y2 axis

    INPUT "Do you want the screen sump to the printer";
dump$

    CALL Viewport(Xmim, Xmax, Ymim, Ymax, Tmim, Tmax)

j = 8    'start of data point in DATA$
interval = 3
Voffset = .000798                    'voltage offset for 20
                                     'degree C when testing

FOR I = 0 TO 3999 STEP 3 'data point

    V(I) = VAL(MID$(DATA$, j, 5)) * V1 + Voffset    'voltage
                                                    'in volts
    Time = I * H1         'time in second
```

```
'  Convert voltage to Celsius temperature, valid only for
'  K-type thermocouple

Ttail = V(I) * (a5 + V(I) * (a6 + V(I) * (a7 + a8 * V(I))))
T(I) = a0 + V(I) * (a1 + V(I) * (a2 + V(I) * (a3 + V(I) *
(a4 + Ttail))))

'   result come out as second and volt, re-format the data
'   to besaved in diskfile for future import to graphic
'   program, if necessary

    IF I > 0 THEN
    LINE (Time - H1, V(I - interval))-(Time, V(I))
    LINE (Time - H1, T(I - interval) / Factor + Ymim)-(Time,
T(I) / Factor + Ymim)
    END IF

        'PRINT USING "###.######"; Time;
        'PRINT "SEC",
        'PRINT USING "###.######"; V(I);
        'PRINT "VOLTS",
        'PRINT USING "####"; T(I)

        IF UCASE$(ans$) = "y" THEN
            PRINT #2, USING "###.######"; Time;
            'PRINT #2, USING "###.######"; V(I);
            PRINT #2, USING "######"; T(I)
        END IF

j = j + 5 * interval          'depend on how data point to
                              'be read, 5 for all data
IF j > LEN(DATA$) THEN EXIT FOR

NEXT I
        IF UCASE$(dump$) = "Y" THEN
            DATA$ = ""        'free up memory for screen dump
            'CALL scrndump("100", 1, 1)   'Pro.lib procedure
            CALL herc.hp
        END IF
CLOSE #2

END

SUB herc.hp
'==============================================================
'    Hercules mode 3 screen dumping routine for HP laser '
'    printer.
'==============================================================
    HERClength = 32767   'size of Hercules memory
    DEF SEG = &HB000    'Hercules screen segment
    BSAVE "$tmp.tm1", 0, HERClength  'bsave the screen image
```

```
    E$ = CHR$(27)    'escape
    Hdr$ = E$ + "*t100r" '75dpi resolution
    Hdr$ = Hdr$ + E$ + "*r1A"'initialize graphics

    HERCdata$ = SPACE$(HERClength)  'room for screen image
    DEF SEG
    BLOAD "$tmp.tm1", SADD(HERCdata$)       'bload it into
HERCdata$

    OPEN "$tmp.tm2" FOR RANDOM AS #99 LEN = 96
                                    '99 should be safe number
    FIELD #99, 6 AS Start$, 90 AS Dat$    '90 bytes per line
    LSET Start$ = E$ + "*b90W"           'start graphic
command

    FOR x = 1 TO 7830 STEP 90       'create image file 7830
                                    'bytes per interleaf
        FOR j = 0 TO 3
            LSET Dat$ = MID$(HERCdata$, 8192 * j + x, 90)
        PUT #99
        NEXT j
    NEXT x
    CLOSE #99

    LPRINT Hdr$;         'lprint header directly
    SHELL "copy $tmp.tm2/b lpt1: >nul:"     'copy the data
    LPRINT E$; "*rB"; E$; "E";   'end-of -graphic + reset
    KILL "$tmp.tm?"      'delete temporary files

END SUB

SUB Viewport (Xmim, Xmax, Ymim, Ymax, Tmim, Tmax)

    Title$ = "Nicolet Oscilloscope"
    Xaxis$ = "TIME (SEC)"
    Yaxis1$ = "VOLTAGE (V)"
    Yaxis2$ = "TEMPERATURE (C)"
    Xticknum = 9
    Y1ticknum = 7
    Y2ticknum = 6

CLS : SCREEN 8  'EGA screen 8 (Hercules screen 3, view
160,40-560,270)
    VIEW (140, 20)-(500, 150), , 1
    Xrange = 500 - 140 + 1
    Yrange = 150 - 20 + 1
    XTick = Xrange / (Xticknum + 1)
    Y1Tick = Yrange / (Y1ticknum + 1)
    Y2Tick = Yrange / (Y2ticknum + 1)
    TickLength = Xrange / 25
'Label X axis
    FOR I = 1 TO Xticknum
```

```
        LINE (I * XTick, Yrange)-(I * XTick, Yrange -
TickLength / 2)
        LINE (I * XTick, 0)-(I * XTick, TickLength / 2)
    NEXT I
'Label left Y axis
    FOR j = 1 TO Y1ticknum
        LINE (0, j * Y1Tick)-(TickLength, j * Y1Tick)
    NEXT j
'Label right Y axis
    FOR K = 1 TO Y2ticknum
        LINE (Xrange, K * Y2Tick)-(Xrange - TickLength, K *
Y2Tick)
    NEXT K

 WINDOW (Xmim, Ymim)-(Xmax, Ymax)
    LOCATE 21, 17: PRINT Xmim
    LOCATE 21, 61: PRINT Xmax
    LOCATE 20, 13: PRINT Ymim
    LOCATE 3, 13:  PRINT Ymax
    LOCATE 20, 65: PRINT Tmim
    LOCATE 3, 64:  PRINT Tmax

    PT% = 40 - LEN(Title$) / 2
    LOCATE 2, PT%
    PRINT Title$
    PX% = 40 - LEN(Xaxis$) / 2
    LOCATE 22, PX%
    PRINT Xaxis$
    PY1% = 12 - LEN(Yaxis1$) / 2
    FOR I% = 1 TO LEN(Yaxis1$)
        LOCATE PY1% + I% - 1, 14
        PRINT MID$(Yaxis1$, I%, 1)
    NEXT I%
    PY2% = 12 - LEN(Yaxis2$) / 2
    FOR j% = 1 TO LEN(Yaxis2$)
        LOCATE PY2% + j% - 1, 67
        PRINT MID$(Yaxis2$, j%, 1)
    NEXT j%

END SUB
```

Grain Boundary Bubble Growth

This appendix details the computer program for calculation of the grain boundary bubble growth as a function of time in the HAZ during welding. This program is written using Microsoft QuickBasic, version 4.5.

```
DECLARE SUB RegimeII ()
DECLARE SUB Model (ModelNum$, GrowConst!, RIII!, DgbIII!,
     DlaIII!)

'=========================MODELING.BAS=====================
'  This program is used to modeling the grain boundary
'  helium bubble kinetics during welding of helium
'  containing 316 stainless steels.
'==========================================================

CLS
'INPUT "Enter the size of array (iteration) = ", E%
E% = 400
DIM SHARED Time(E%), Temp(E%), TS(E%), Size(E%),
CoolTime(E%)

'General purpose constant

    CONST Pi = 3.14159
    CONST GBThickness = 4E-10 '(M)
    CONST Spacing = .000001'(M)
    CONST Boltzmann = 1.38053E-23  '(J/K)
    CONST eV = 1.602095E-19     '(J)
    CONST Volume = 1.2057E-29'(M^3)
    CONST SurfConst = 2
    CONST TempInit = 293'(K)
    CONST Tmax = 1573 '(K)
    CONST RI = 1E-09  '(M), final radius at Regime I
    CONST Enthalpy = 1.8 * eV
    CONST Entropy = 1.5 * Boltzmann
    CONST Qdiff = 1.65  ' ACTIVATION ENERGY FOR DIFFUSION
    CONST DeltaTime = .01 'Time interval for Regime III
    CONST Xmin = 0
    CONST Xmax = 4
    CONST Ymin = 0
    CONST Ymax = 1.2
'==================================
```

```
    Temp(0) = Tmax
    CoolTime(0) = 0

     CALL RegimeII

CLS
    PRINT "Final bubble diameter in Regime II is ";
    PRINT USING "#.#######"; 2 * 1000000! * RII;
    PRINT " um"
    PRINT


   PRINT "Press any key to continue Regime III."

DO: LOOP UNTIL INKEY$ <> ""


'===================================
'Beginning of the Regime III
'===================================
DO
    CLS
    PRINT "Select one destination for the output :"
    PRINT "1. Screen"
    PRINT "2. Printer"
    PRINT "3. Diskfile"
    PRINT "4. Quit"

    Choice$ = UCASE$(INPUT$(1))
LOOP WHILE INSTR("1234SPDQ", Choice$) = 0

    SELECT CASE Choice$
        CASE "1", "S"
              Filespec$ = "SCRN:"
        CASE "2", "P"
              Filespec$ = "LPT1:"
        CASE "3", "D"
              INPUT "What is the file name ?", Filespec$
        CASE ELSE
              END
    END SELECT

DO
        CLS
        PRINT "Choose a model number to calculate growth
rate"
        PRINT
        PRINT "1.  Hull -Rimmer"
        PRINT "2.  Speight - Harris"
        PRINT "3.  Speight - Beere"
        PRINT "4.  J. Weertman"
        PRINT "5.  Dobes-Cadek"
```

```
        PRINT "6.  B.T.M. Loh"
        ModelNum$ = INPUT$(1)

LOOP WHILE INSTR("123456", ModelNum$) = 0


CLS
OPEN Filespec$ FOR OUTPUT AS #1

INPUT "APPLIED COMPRESSIVE STRESS (Pa) = "; Compress

CLS
    IF Choice$ = "3" OR Choice$ = "D" THEN
        PRINT "Data saving in progress..."
    ELSE
      PRINT #1, "   TIME     DIA.    TEMP    THERMAL    UTS
   GBs      YS"
     PRINT #1, "   sec       um       K       MPa       MPa
  MPa      MPa"
      PRINT #1,
      VIEW PRINT 4 TO 24   'Preserve the output title label
    END IF

    RIII = RII  'Initialize  size at beginning of Regime III

Size(0) = RIII * 2000000!

FOR I = 1 TO E%

'IF RIII >= Spacing / 2 THEN    'Speight & Beere invalid
'I = E%
'GOTO Nextloop:   'exit  when RIII reach critical size
'END IF


    Time(I) = I * DeltaTime + .785          'TIME

'for 0 to 7 sec cooling data point fit
    TempPart = 36.815986# + Time(I) * (-2.286686 + Time(I) *
(-.234133 + .025553 * Time(I)))
    Temp(I) = 1573.349115# + Time(I) * (49.728468# + Time(I)
* (-150.006827# + Time(I) * TempPart))

    DeltaTemp = Temp(I - 1) - Temp(I)    'DELTA TEMPERATURE

'Calculate the Young's Modulus (Pa)

Temp(I) = 1.8 * Temp(I) - 459.4         'CONVERT TO
TEMPERATURE F

ModTail = 3.69785E-06 * Temp(I) ^ 2 - 7.709188E-10 * Temp(I)
^ 3
```

```
Modulus = 6.894757E+09 * (28.33669 - (2.882211E-03 *
Temp(I)) - ModTail)

'Calculate the thermal strain

Strain1 = 2.679852E-06 * Temp(I) ^ 2 - 4.95473E-10 * Temp(I)
^ 3

Strain2 = .0000018 * (8.09139 + (5.496948E-03 * Temp(I)) -
Strain1)

DeltaStrain = DeltaTemp * Strain2

Strain = DeltaStrain + Strain  'Total strain

'SHRINKAGE STRESS Pa, ADD EXTERNAL APPLIED STRESSES

    ShrinkStress1 = (Modulus * Strain - Compress)

'Effect of Surface Tension on the bubble growth

    Temp(I) = (Temp(I) + 459.4) / 1.8  'absolute temperature

    Gamma = -.00151 * Temp(I) + 4.11
    SurfaceTension = SurfConst * Gamma / RIII'Pa
    ShrinkStress = ShrinkStress1 - SurfaceTension

        IF ShrinkStress < 0 THEN
            ShrinkStress = 0
        END IF

       TS(I) = ShrinkStress

'GB DIFFUSIVITY

    DgbIII = 7.7E-14 / GBThickness * EXP(-Qdiff * eV /
Boltzmann / Temp(I))

'Lattice diffusivity

    DlaIII = .000105 * EXP(-67800 / 1.987 / Temp(I))

'AMOUNT OF BUBBLE GROWTH

  GrowConst1 = DgbIII * GBThickness * Volume * TS(I) *
DeltaTime

  GrowConst = GrowConst1 / 2 / Boltzmann / Temp(I) / RIII

CALL Model(ModelNum$, GrowConst, RIII, DgbIII, DlaIII)
```

```
RESULT:

    RIII = RIII + Growth          'BUBBLE SIZE RADIUS
    Size(I) = RIII * 2000000!          'BUBBLE DIAMETER IN um
    TS(I) = TS(I) / 1000000!           'THERMAL STRESS MPa


'Produce output to Destination #1

PRINT #1, USING "####.##  "; CoolTime(I); Size(I); Temp(I)

Nextloop:

NEXT I

CLOSE #1

END

SUB Model (ModelNum$, GrowConst, RIII, DgbIII, DlaIII)
'==========================================================
'   Calculate bubble growth based on selected model.
'==========================================================
SHARED Growth

    IF ModelNum$ = "1" THEN

      Heading$ = "<< HULL-RIMMER MODEL >>"
      Growth = GrowConst * 4 * Pi / Spacing

    ELSEIF ModelNum$ = "2" THEN

      Heading$ = "<< SPEIGHT-HARRIS MODEL >>"
      SHconst1 = 1 / RIII - 4 * RIII / Spacing ^ 2
      SHconst2 = LOG(Spacing / (2 * RIII))
      SHconst3 = (Spacing ^ 2 - 4 * RIII ^ 2) / (2 * Spacing
^ 2)
        Growth = GrowConst * SHconst1 / (SHconst2 -
SHconst3)

    ELSEIF ModelNum$ = "3" THEN

      Heading$ = "<< SPEIGHT-BEERE MODEL >>"
      Sbconst1 = 1 - 4 * RIII ^ 2 / Spacing ^ 2
      SBconst2 = Sbconst1 * (3 - 4 * RIII ^ 2 / Spacing ^ 2)
/ 4
      SBconst3 = LOG(Spacing / 2 / RIII) - SBconst2
      Growth = GrowConst / RIII / SBconst3

    ELSEIF ModelNum$ = "4" THEN
```

```
     Heading$ = "<< J. WEERTMAN MODEL >>"
      JW.const = 4 * LOG(Spacing / 2 / RIII) - 3
      C0 = (EXP(-Enthalpy / Boltzmann / Temp(I)) *
EXP(Entropy / Boltzmann))
      Growth = GrowConst * 4 * C0 / RIII / JW.const

    ELSEIF ModelNum$ = "5" THEN

      'Assume numerical factor Gamma=1

      Heading$ = "<< DOBES-CADEK Model >>"
      DC.Const1 = (2 * DlaIII / .00007 / GBThickness /
DgbIII) ^ .5
      DC.Const2 = (.00007 * GBThickness * DgbIII / 8 /
DlaIII / RIII ^ 2) ^ .5

      Growth = GrowConst * DC.Const1 * (1 + DC.Const2)
      Heading$ = "<< DOBES-CADEK Model >>"

    ELSE

 'Assume volume relaxtion is 13% (6-20% for infinit cryatal)

      Heading$ = "<< B.T.M. LOH MODEL >>"
      Growth = GrowConst * 5 * .13 / RIII

    END IF
SUB RegimeII
'=====================================================
'            Beginning of the Regime II
'=====================================================
SHARED RII
    DeltaTimeII = 1.57  'Total time for Regime II in second

'Grain boundary diffusion

    DgbII = 7.7E-14 / GBThickness * EXP(-Qdiff * eV /
Boltzmann / Tmax)

    Cv = (EXP(-Enthalpy / Boltzmann / Tmax) * EXP(Entropy /
Boltzmann)) / Volume

'Final radius at Regime II

    RIItail = 3 * GBThickness * Volume * DgbII * Cv *
DeltaTimeII / 2

    RII = (RI ^ 3 + RIItail) ^ (1 / 3)

END SUB
```

Volume Average Diameter

This appendix details the computer program for calculation of the cavity volume average diameter (VAD). This program is written using Microsoft QuickBasic, version 4.5.

```
DECLARE SUB inputdata ()
DECLARE SUB changedata ()
DECLARE SUB inqury ()
'======================  VAD.BAS  =========================
'  This program calculates the volume-average diameter of a
'  set of cavity or bubble distribution.
'==========================================================
COMMON SHARED i, j, k, m, z
z = 100          ' total number of classes
DIM SHARED diameter(z), count(z)
i = 1
n = 0
Nd3 = 0
CLS
CALL inputdata
FOR m = 1 TO i - 1
n = n + count(m)
Nd3 = count(m) * diameter(m) ^ 3 + Nd3
NEXT m
vad = (Nd3 / n) ^ (1 / 3)
PRINT
PRINT "Total cavity number = "; n
PRINT "The cavity volume-average diameter = "; vad;
"micrometer."
END

SUB changedata
PRINT : PRINT : PRINT
INPUT "Which the data number to change ?", num
PRINT "Old diameter = "; diameter(num)
INPUT "new diameter = ", diameter(num)
PRINT "old number of count = "; count(num)
INPUT "new number of count = ", count(num)
INPUT "more change ? ", ans$
IF UCASE$(ans$) = "Y" THEN CALL changedata
CALL inqury
END SUB

SUB inputdata
PRINT : PRINT : PRINT
PRINT "Please input cavity diameter and number of count"
```

```
PRINT "Enter SPACE twice to end input"
PRINT
FOR i = i TO z
INPUT "input cavity diameter  =  ", diameter(i)
INPUT "input number of cavity =  ", count(i)
IF diameter(i) = 0 THEN EXIT FOR
NEXT i
CALL inqury
END SUB

SUB inqury
CLS
PRINT : PRINT : PRINT
PRINT "No.        Diameter        Count"
PRINT
FOR j = 1 TO i - 1
PRINT j, diameter(j), count(j)
NEXT j
PRINT
DO
INPUT "(A)ppend, (C)hange or (G)o to calculate VAD ?", ans$
LOOP WHILE INSTR("aAcCgG", ans$) = 0
SELECT CASE ans$
        CASE "c", "C"
              CALL changedata
        CASE "a", "A"
              CALL inputdata
END SELECT
END SUB
```

ORNL/TM-13256
Distribution
Category UC-423

INTERNAL DISTRIBUTION

1-2. Central Research Library
3. Document Reference Section
4-5. Laboratory Records Department
6. Laboratory Records, ORNL RC
7. ORNL Patent Section
8-10. M&C Records Office
11. S. S. Babu
12. D. N. Braski
13. D. F. Craig
14. S. A. David
15. K. Farrell
16. G. M. Goodwin
17. A. N. Gubbi
18. M. L. Grossbeck
19. J. A. Horak
20. E. A. Kenik
21. J. F. King
22. R. L. Klueh
23. H. T. Lin
24. J. S. Lin
25. D. C. Lousteau
26. L. K. Mansur
27. H. E. McCoy, Jr.
28. D. J. McGuire
29. R. K. Nanstad
30. B. E. Nelson
31. G. R. Rao
32. J. P. Robertson
33. A. F. Rowcliffe
34. M. J. Saltmarsh
35. M. L. Santella
36. V. K. Sikka
37. R. E. Stoller
38. J. M. Vitek
39-48. C. A. Wang
49. S. J. Zinkle

EXTERNAL DISTRIBUTION

50-52. ARGONNE NATIONAL LABORATORY, 9700 S. Cass Avenue, Argonne, IL 60439

M. C. Billone
R. Mattas
D. L. Smith

53-55. AUBURN UNIVERSITY, Department of Mechanical Engineering, Auburn, AL 36849

B. A. Chin
M. Thakur
R. Zee

56-58. BATTELLE PACIFIC NORTHWEST LABORATORY, P.O. Box 999, Richland, WA 99352

A. Ermi
F. A. Garner
M. L. Hamilton

59-60. ECN PETTEN, Materials Department, P.O. Box 1, 1755 ZG Petten, The Netherlands

M. I. de Vries
B. van der Schaaf

61-62. GENERAL ATOMICS, P.O. Box 81608, San Diego, CA 92138

R. Johnson
J. P. Smith

63. IFF, Kernforchungsanlage, Postfach 1913, D-5170 Julich 1, Germany

H. Ullmaier

64. INSTITUT FÜR MATERIAL - UND FESTKÖRPERFORSCHUNG, Kernforschungszentrum Karlsruhe, D-7500 Karlsruhe, Germany

K. Ehrlich

65-68. JAERI, Nuclear Fuel Research Division, Tokai-mura, Naka-gun 319-11, Ibaraki-ken, Japan

S. Hamada
A. Hishinuma
S. Jitsukawa
M. Suzuki

67-70. JOINT RESEARCH CENTRE, Ispra Establishment, Materials Science Division 21020 - ISPRA (Varese) Italy

P. Fenici
P. Schiller

71. McDONNELL DOUGLAS ASTRONAUTICS COMPANY, EAST, P.O. Box 516, St. Louis, MO 63166

J. W. Davis

72. NATIONAL RESEARCH INSTITUTE FOR METALS, Tsukuba, Japan

M. Okada

73-75. ITER TEAM, Max-Plank - Institut Fùr Plasmaphysik, Boltzmannstrasse 2, 85748 Garching, Germany

R. Parker
G. Kalinin
J. Nihoul

76. RISO NATIONAL LABORATORY, Metallurgy Department, DK 4000, Roskilde, Denmark

B. N. Singh

77. SCK, Boeretang 200, B-2400 MOL, Belgium

W. Vander Meulen

78. SANDIA NATIONAL LABORATORIES, Livermore Division 8316, Livermore, CA 94550

S. Goods

79-83. SAVANNAH RIVER LABORATORY, Aiken, SC 29801

A. K. Birchenall
G. R. Caskey, Jr.
W. R. Kanne
R. E. Nygren
J. R. Wermer

84-86. UNIVERSITY OF CALIFORNIA, 5532 Boelter Hall, Los Angeles, CA 90024

M. A. Abdou
R. W. Conn
N. Ghoniem

87-88. UNIVERSITY OF CALIFORNIA, Department of Chemical and Nuclear Engineering, Santa Barbara, CA 93106

G. E. Lucas
G. R. Odette

89. 9A Cumnor Rise Road, Cumnor Hill, Oxford, OX2 9HD, England

D. R. Harries

90. UNIVERSITY OF MISSOURI, Nuclear Engineering, Rolla, MO 65401

A. Kumar

91. UNIVERSITY OF WISCONSIN, Nuclear Engineering Department, Madison, WI 53706

G. L. Kulcinski

92. TOHUKU UNIVERSITY, Katahira 2-1-1, Sendai 980, Japan

H. Matsui

93-94. NATIONAL INSTITUTE FOR FUSION SCIENCE, Furo-cho, Chikusa, Nagaya 464-01, Japan

T. Muroga
A. Rohyama

95-96. DOE, OFFICE OF FUSION ENERGY, Reactor Technologies Branch, MS G-234 (GTN), Washington, DC 20545

M. M. Cohen
F. W. Wiffen

97. DOE, OAK RIDGE OPERATIONS OFFICE, P.O. Box 2001, Oak Ridge, TN 37831-8600

Office of Assistant Manager for Energy Research and Development

98-99. DOE, OFFICE OF TECHNICAL AND SCIENTIFIC INFORMATION, Office of Information Services, P.O. Box 62, Oak Ridge, TN 37831

For distribution as shown in DOE/OSTI-4500, Distribution Category UC-423 (Magnetic Fusion Reactor Materials)